THE UNIVERSITY OF SHEFFIELD

Particle Acceleration in Near Earth Geospace

by

Homayon Aryan

A thesis submitted in partial fulfillment for the
degree of Doctor of Philosophy

in the

Faculty of Engineering

Department of Automatic Control and Systems Engineering

January 2015

Declaration of Authorship

I, Homayon Aryan, declare that this thesis titled, 'Particle Acceleration in Near Earth Geospace' and the work presented in it are my own. I confirm that:

- This work was done wholly or mainly while in candidature for a research degree at this University.
- Where any part of this thesis has previously been submitted for a degree or any other qualification at this University or any other institution, this has been clearly stated.
- Where I have consulted the published work of others, this is always clearly attributed.
- Where I have quoted from the work of others, the source is always given. With the exception of such quotations, this thesis is entirely my own work.
- I have acknowledged all main sources of help.
- Where the thesis is based on work done by myself jointly with others, I have made clear exactly what was done by others and what I have contributed myself.

Signed: _____

Date: _____

"Try not to become a man of success, but rather try to become a man of value."

Albert Einstein

THE UNIVERSITY OF SHEFFIELD

Abstract

Faculty of Engineering

Department of Automatic Control and Systems Engineering

Doctor of Philosophy

by Homayon Aryan

The radiation belts occupy a vast region of near Earth geospace where many important communication, navigation, Earth observation, and defence satellites operate. In recent decades, demand for space technology has grown dramatically and this is set to grow further as humans become more and more dependent on space technology. Without the operation of currently hundreds of satellites around the Earth, the world would face a huge catastrophe to support a population of 7 billion plus. Trapped energetic radiation belt electrons represent a serious hazard to spacecraft electronic components. At the geostationary orbit, which is located at the edge of the outer radiation belt, these highly energetic electrons are accelerated to high energies, in the range of keV to MeV, through various processes. Therefore, it is considerably important to understand the basic properties of the Van Allen radiation belts and the main processes that are thought to be important in the acceleration and loss mechanisms of the radiation belt electrons that ultimately change the dynamics of the radiation belts. This thesis investigates particle acceleration in near Earth geospace. The findings of this research expanded our knowledge of the Van Allen radiation belts through studying the relationship between solar wind parameters and energetic electron fluxes at the outer radiation belt, the study of naturally occurring electromagnetic waves and their crucial role in the acceleration and loss of energetic electrons in the inner magnetosphere, and the study of particle acceleration in the vicinity of the Earth and interplanetary medium by strong interplanetary collisionless shocks associated with Coronal Mass Ejection (CME), in particular, in the case of strong collisionless shock formation associated with shock coalescence. The results can be used to help improve forecasting and nowcasting of changes in energetic electron population and ultimately help mitigate the damage caused to the satellites and other space based systems. Subsequently, this would help increase satellite lifetime and improve reliability.

Acknowledgements

First of all, I would like to thank my supervisors, Professor Michael Balikhin and Doctor Simon Pope, for their valuable advice and guidance throughout my PhD program. I am sincerely grateful an indebted to Professor Michael Balikhin for giving me the opportunity to prove myself. I am honoured to have had the privilege to work with him. He is an inspirational scientist and a role model. I would also like to thank all members of the Space Systems Laboratory group (Simon Walker, Richard Boynton, Keith Yearby, Victor Fedun, Ivan Pakhotin, and Andrew Dimmock) for useful physics discussions. I am especialy grateful to Doctor Simon Walker for his advice and guidance.

This work would have not been possible without the support and encouragement of my Family. So I would like to thank each and everyone of my family members for always believing in me. I especially would like to thank my mother for looking after me. Last but not least, I would like to thank my friends for putting up with me throughout my studies.

Contents

List of Figures

List of Tables

Abbreviations

ACE	**A**dvanced **C**omposition **E**xplorer
CCMC	**C**ommunity **C**oordinated **M**odelling **C**entre
CIR	**C**o-rotating **I**nteraction **R**egion
CME	**C**oronal **M**ass **E**jection
CRRES	**C**ombined **R**elease and **R**adiation **E**ffects **S**atellite
DWP	**D**igital **W**ave **P**rocessor
EEF	**E**energetic **E**lectron **F**lux
EMIC	**E**lectromagnetic **I**on **C**yclotron
ESA	**E**uropean **S**pace **A**gency
FFT	**F**ast **F**ourier **T**ransform
GPS	**G**lobal **P**ositioning **S**atellites
IMF	**I**nterplanetary **M**agnetic **F**ield
IP	**I**nter**P**lanetary
JGR	**J**ournal of **G**eophysical **R**esearch
LASCO	**L**arge **A**ngle and **S**pectrometric **CO**ronagraph
LEO	**L**ow **E**arth **O**rbit
MAG	**MAG**netometer aboard ACE
MEO	**M**edium **E**arth **O**rbit
MHD	**M**agnetohydrodynamics

MLT	**M**agnetic **L**ocal **T**ime
NARMAX	**N**onlinear **A**uto**R**egressive **M**oving **A**verage **M**odelling
NASA	**N**ational **A**eronautics and **S**pace **A**dministration
NOAA	**N**ational **O**ceanic and **A**tmospheric **A**dministration
SI	**I**nternational **S**ystem
SIR	**S**tream **I**nteraction **R**egion
SOHO	**SO**lar and **H**eliospheric **O**bservatory
STAFF	**S**patio **T**emporal **A**nalysis of **F**ield **F**luctuation
STEREO	**S**olar **TE**rrestrial **RE**lations **O**bservatory
SWPC	**S**pace **W**eather **P**rediction **C**enter
TC1	**Tan Ce 1**
THEMIS	**T**ime **H**istory of **E**vents and **M**acroscale **I**nteractions during **S**ubstorms)
UT	**U**niversal **T**ime
VEX	**V**enus **EX**press
VLF	**V**ery **L**ow **F**requency

Physical Constants

Astronomical unit	Au	=	1.495978707×10^8 km (exact)
Particle charge	q	=	1.602×10^{-19} C (exact)
Speed of Light	c	=	$2.997\ 924\ 58 \times 10^8$ ms^{-1} (exact)

Symbols

A_{Lower}	Lower Kullback-Leibler acceptance level	
A_{Upper}	Upper Kullback-Leibler acceptance level	
Ae	Auroral electrojet index	nT
AL	Westerly auroral electrojet	nT
AU	Easterly auroral electrojet	nT
$\overline{B}$	Average magnetic field	nT
B	Magnetic field	nT
$\overline{B_\alpha}$	Average horizontal Cartesian component of magnetic field vector	nT
$\overline{B_\beta}$	Average vertical Cartesian component of magnetic field vector	nT
$\|B\|$	Magnetic field magnitude	nT
B_d	Downstream magnetic field	nT
B_L	Parallel magnetic field component	nT
B_m	Perpendicular magnetic field	nT
B_n	Shock normal direction	nT
Bs	Negative of vertical interplanetary magnetic field component	nT
Bs_{60}	Bs with 60 minutes delay	nT
Bs_{90}	Bs with 90 minutes delay	nT
Bs_{120}	Bs with 120 minutes delay	nT
B_u	Upstream magnetic field	nT

B_x	Magnetic field x component	nT
B_y	Magnetic field y component	nT
B_z	Vertical interplanetary magnetic field component	nT
c_s	Sonic speed	kms^{-1}
ΔB	Magnetic field jump	nT
Dst	Disturbance storm time index	nT
E	Electric field	$\mathrm{N.C}^{-1}$
f_{ce}	Electron Cyclotron Frequency	
F_L	Electromagnetic Lorentz force	N
H_i	Horizontal component of the geomagnetic field	nT
D_{KL}	Kullback-Leibler Distance	
D_{KLlh}	Kullback-Leibler Distance between low and high	
D_{KLlm}	Kullback-Leibler Distance between low and moderate	
D_{KLmf}	Kullback-Leibler Distance between moderate and fast	
D_{KLmh}	Kullback-Leibler Distance between moderate and high	
D_{KLsm}	Kullback-Leibler Distance between slow and moderate	
D_{KLsf}	Kullback-Leibler Distance between slow and fast	
K	Number of magnetic field measurements	
K index	Kennziffer index	
Kp index	Global Kennziffer planetary index	
L	McIlwain L-shell	
$\mathbf{M}$	Mach number	
$M_{\alpha\beta}$	Covariant matrix	
n	Solar wind density	n/cc
n_{0m}	Current day maximum solar wind density	n/cc

n_{1m}	Maximum solar wind density from previous day	n/cc
n_{2m}	Maximum solar wind density from 2 days ago	n/cc
$\hat{n}$	Shock normal	
N_s	Total number of longitudinal stations	
P	Solar wind pressure	nPa
P_{0m}	Current day maximum solar wind pressure	nPa
P_{1m}	Maximum solar wind pressure from previous day	nPa
P_{2m}	Maximum solar wind pressure from 2 days ago	nPa
T	Solar wind temperature	K
v	Particle velocity	ms^{-1}
V_{slow}	Speed of slow shock	kms^{-1}
V_{fast}	Speed of fast shock	kms^{-1}
V_A	Alven velocity	kms^{-1}
V_s	Saturation velocity	kms^{-1}
V_{SW}, V	Solar wind velocity	kms^{-1}
V_{0m}	Current day maximum solar wind velocity	kms^{-1}
V_{1m}	Maximum solar wind velocity from previous day	kms^{-1}
V_{2m}	Maximum solar wind velocity from 2 days ago	kms^{-1}
z	Confidence level	
ω	Angular frequency	$rads^{-1}$
ω_{pi}	Ion plasma frequency	$rads^{-1}$
μ	Electron and ion mass ration	
λ_m	Magnetic latitude	degree (°)
σ	Minimum variance	

For always encouraging me to study and follow my dreams, I dedicate this work to my family.

Chapter 1

Introduction

1.1 Motivation

Today, humanity relies heavily on space technology. While many of us know the crucial roles satellites play in everything from navigation to communication, their significance in many other areas of our lives is perhaps not so widely documented. In recent decades, demand for space technology has grown dramatically and this is set to grow further as humans become more and more dependent on space technology, primarily for communication, navigation, defence, Earth observation, and scientific purposes. Without the operation of currently hundreds of satellites around the Earth, the world would face a huge catastrophe to support a population of 7 billion plus. Some of the main potential problems that could arise from satellite failures include: Global Positioning System (GPS) failure leading to critical congestion levels and planes flying longer routes (GPS data is used to reduce fuel burn and flight time through direct routing with reduced separation between airplanes), broadcasting failure, communication failure, lack of accurate

weather prediction (satellites are used to predict extreme weather events, such as hurricanes, in advance and prevent catastrophic disasters by providing advance warning), plummeting food production (satellite images are used in food production to monitor crops and ensure high yield), and lack of surveillance (this can leave defence systems vulnerable).

Space weather is thought to be the main contributing factor that can impact the performance of satellite systems and can cause satellite anomalies, damage critical electronic components, and degrade solar arrays [13, 66, 68, 93, 111, 152], which are both very costly and disruptive. Space weather is the term commonly used to refer to the highly variable conditions in the near Earth geospace environment. Space weather mostly initiate at the Sun and affect the entire solar system including the space environment in the vicinity of the Earth. This has fascinated humans from very early prehistory. Charged plasma is constantly emitted from the Sun's surface and races through space, away from the Sun, in the form of solar wind. The Earth's magnetic field provides a vital defensive shield in the form of magnetosphere that diverts most of the charged plasma particles around the Earth at the magnetopause. Without this protection the solar wind would destroy the Earth's ozone layer, the upper layer of the atmosphere responsible for protecting Earth from ultraviolet radiation, and ultimately cast doubt over persistence of life on Earth.

Some charged particles that do enter become trapped within the Earth's radiation belts which can be hazardous to satellite electronic subsystems. By far the most crucial satellites, such as communication satellites, often operate within the highly dynamic regions of the Earth's radiation belts where the flux of relativistic

electrons can change by several orders of magnitude during storms and other disturbances [15, 57, 193]. Often the relativistic electrons found trapped within these regions are referred to as the killer electrons due to their ability to damage electronic systems aboard satellites that may lead to permanent failure of individual subsystem, or even complete loss of the satellite [12, 19, 34, 68, 69, 91]. Inevitably, causing disruptions to communication, navigation, Earth observation, and defence. In 2002, *Baker* [13] reported that the operational anomalies of Galaxy IV satellite in May 1998, Telstar 401 satellite in January 1997, and MARECS-A satellite in February 1986 were most likely caused by energetic electrons. Such particles may also penetrate the satellite and cause component damage. For example, the loss of solar power on ANIK E1 in 1994 [12].

Energetic particles found in the vicinity of the Earth are not only hazardous to spacecraft electronic components but also poses serious health risks to humans in space. Radiation was identified as a serious hazard to human health during the very first human spaceflight program, Project Mercury, by NASA between 1959 to 1963. In this project, exposure to radiation was carefully monitored to prevent potential biological damage and health risks to astronauts. Energetic charged particles, such as electrons, protons, alpha, and heavier particles, in the vicinity of the Earth originate from two sources: Van Allen radiation belts and solar energetic particle events which may be related according to some studies [216]. Unshielded exposure to extensive solar particle events can lead to serious health effects. Thus, careful consideration of potential radiation environment is necessary to mitigate the risk to astronauts that may operate or travel through high radiation regions.

Energetic charged particles are mainly trapped within the Earth's Van Allen radiation belts by the Earth's magnetic field. This creates a torus of donut shaped

charged particles around the Earth. The Van Allen radiation belt was named after James Van Allen who discovered the inner belt in 1958. The outer belt was detected by Sputnik 3, which was later confirmed by Explorer III mission. Energetic electrons with energies that range from hundreds of keV up to several MeV are mainly trapped equatorially within the Earths inner ($1.1 < L < 2$) and outer ($3 < L < 7$) radiation belts which are separated by what is known as the slot region ($2 < L < 3$) (where L is the McIlwain L−shell [161] that roughly tags a specific magnetic field line by the radial distance in Earth radii of its equatorial crossing). The inner radiation belt is relatively stable and only varies during intense geomagnetic storms [146, 171]. However, the outer radiation belt is highly dynamic and the flux of energetic electrons can vary by several orders of magnitude during storms and other disturbance [15, 19, 34, 57, 193, 245]. Figure 1.1 presents a schematic of the Earth's Van Allen radiation belts together with some of the most common satellite orbits that pass through the radiation belts.

Evidently, the radiation belts occupy a vast region of geospace near Earth that is heavily used by very important satellites, such as, communication, navigation, Earth observation, and defence satellites. And as humans continue to expand space operation and become more and more dependent on space based technology, the need for more satellite operation within the radiation belt occupied regions will only grow. The energetic electrons trapped within the radiation belts pose significant threat to these satellites by damaging or destroying critical electronic systems, causing satellite anomalies, and degrading solar arrays. Despite decades of intense research, the acceleration mechanisms of radiation belt electrons that affect the dynamics of the Earths radiation belts [8, 24, 37, 138, 220, 241] are not yet fully understood. Therefore, it is considerably important to understand

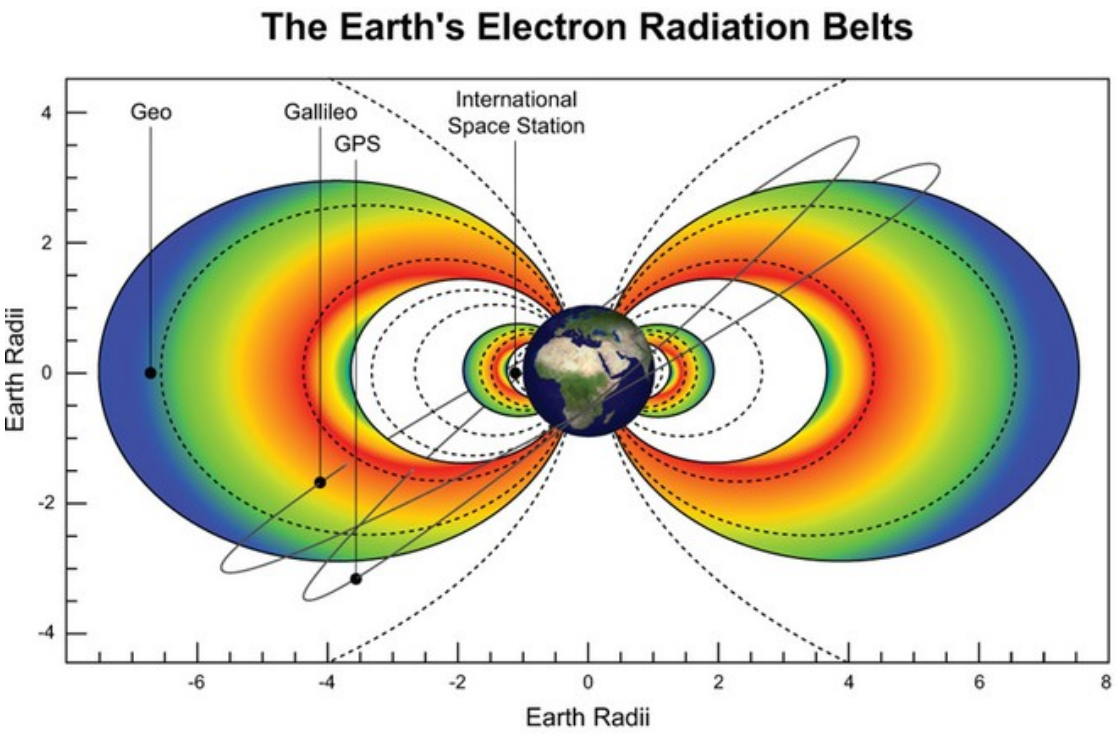

FIGURE 1.1: A schematic of the Earth's Van Allen radiation belts together with some of the most common satellite orbits that pass through the radiation belts, adapted from *Horne* [99].

the acceleration mechanisms of radiation belt electrons, the properties of the Van Allen radiation belts, and the processes that are thought to be important in its dynamics.

This thesis investigates the flux of energetic electrons at the geostationary orbit, an equatorial orbit with an orbit period equal to the Earth's rotation period that is located at the edge of the outer radiation belt where many important satellites continuously operate. Also, study the crucial role played by naturally occurring electromagnetic waves in the acceleration and loss of energetic electrons in the inner magnetosphere that ultimately change the dynamics of the radiation belts. And finally examine how the propagation of strong interplanetary collisionless shocks associated with Coronal Mass Ejections contribute to the acceleration of particles to relativistic energies.

1.2 Overview

The Earth's magnetosphere is a highly complex and dynamic system formed as a result of solar wind interaction with the Earth's magnetic field. Chapter 2 provides a brief introduction of the Sun and its complex interaction with the Earth's magnetic field. It provides a brief insight into the magnetospheric physics and the basic physical process that occur in space plasma. It also discusses the population of trapped energetic Van Allen radiation belt particles.

Chapter 3 describes the crucial role of solar wind parameters in the dynamic of the radiation belts. In particular, this chapter investigates the trends between Energetic Electron Fluxes (EEF) and solar wind velocity (V_{SW}) at geostationary orbit. Previous studies have shown that for constant solar wind density, energetic electron flux increases with solar wind velocity until a saturation velocity (V_S) is reached. Beyond the saturation velocity an increase in solar wind velocity is statistically not accompanied with energetic electron flux enhancement. This chapter investigates the saturation velocity and its dependency upon solar wind density using the reverse arrangement test. The results prove that solar wind density play a crucial role in defining the relationship between solar wind velocity and electron flux at geostationary orbit. This thesis demonstrats that the saturation velocity was dependent on solar wind density, whereby the saturation velocity decreased as the solar wind density increased. This important new knowledge can be used in forecasting and nowcasting models of energetic electron fluxes at geosynchronous orbit in order to improve predictions and ultimately help mitigate the damage

caused to electronic components of geostationary satellites and other space based systems. The results have been published in the peer-reviewed international Journal of Geophysical Research (JGR) in February 2013 (*Aryan, H., Boynton R. J., and Walker S. N. (2013), Analysis of trends between solar wind velocity and energetic electron fluxes at geostationary orbit using the reverse arrangement test, J. Geophys. Res. Space Phys., 118, doi:10.1029/2012JA018216*).

Chapter 4 describes how naturally occurring electromagnetic waves, in particular chorus waves, contribute to the acceleration and loss of energetic electrons in the inner magnetosphere that ultimately change the dynamics of the radiation belts. The distribution of these waves in the inner magnetosphere is commonly presented under different values of geomagnetic activity as expressed by the geomagnetic indices, despite the fact that not all geomagnetic storms necessarily change relativistic electron fluxes in the outer radiation belt and the fact that geomagnetic indices are indirect and nonspecific parameters that lack time history information. Chapter 4 presents the distribution of chorus waves not only as a function of geomagnetic activity, but also as a function of directly measured solar wind parameters (velocity, density, pressure, and interplanetary magnetic field) that are known to be predominantly effective in the control of radiation belt energetic electron fluxes. The new wave models developed here can benefit studies of the evolution of energetic electron fluxes that rely heavily on the numerical codes in order to model energy and pitch angle diffusion due to electron interaction with plasma waves in the frame of quasi-linear (some properties of linearity) approximation. The new wave models can also be used to improve forecasting and nowcasting of energetic electrons in the inner magnetosphere. The results have been published in the peer-reviewed international Journal of Geophysical

Research in August 2014 (*Aryan, H., Yearby, K., Balikhin, M. A., Agapitov, O. V., Krasnoselskikh, V., and Boynton, R. (2014), Statistical study of chorus wave distributions in the inner magnetosphere using Ae and solar wind parameters, J. Geophys. Res. Space Phys., 119, 6131-6144, doi: 10.1002/2014JA019939*).

Other processes that contribute to the energisation and acceleration of energetic electrons include interplanetary collisionless shock waves that are mainly associated with Coronal Mass Ejections and Co-rotating Interactive Regions. Chapter 5 describes the importance of interplanetary collisionless shocks in the acceleration of energetic particles to relativistic energies. Ions accelerated at these shocks contribute to the solar energetic protons observed in the vicinity of the Earth. Propagating collisionless shocks may coalescence, where weak shocks overtake one another, to form stronger shocks. Chapter 5 reveals that collisionless shocks, associated with Coronal Mass Ejections, coalescence between the orbits of Venus and the Earth and form stronger shocks. Such shocks can be effective accelerators of ions due to multiple reflections (leading to accumulative energy gain) from their colliding fronts. The new results can be used to improve our knowledge and better understand the process of shock formation and coalescence. The results have been published in the peer-reviewed international journal of Annales Geophysicae, in March 2014 (*Aryan, H., Balikhin, M. A., Taktakishvili, A., and Zhang, T. L. (2014), Observation of shocks associated with CMEs in 2007. Ann. Geophys., 3, 223-230, doi: 0.5194/angeo-32-223-2014*).

Chapter 6 summarises the importance of the results obtained in this thesis and how it can helps us better understand particle acceleration in near Earth geospace. The latter chapter also discuses the potential future studies.

1.3 Key Contributions to the Scientific Community

1.3.1 Publications

The following articles were published in the international peer reviewed space physics journals:

- **Aryan, H.,** Yearby, K., Balikhin, M. A., Agapitov, O. V., Krasnoselskikh, V., and Boynton, R. (2014), Statistical study of chorus wave distributions in the inner magnetosphere using Ae and solar wind parameters, J. Geophys. Res. Space Phys., 119, 6131-6144, doi: 10.1002/2014JA019939.

- **Aryan, H.,** Balikhin, M. A., Taktakishvili, A., and Zhang, T. L. (2014), Observation of shocks associated with CMEs in 2007. Ann. Geophys., 3, 223-230, doi: 0.5194/angeo-32-223-2014.

- **Aryan, H.,** Boynton R. J., and Walker S. N. (2013), Analysis of trends between solar wind velocity and energetic electron fluxes at geostationary orbit using the reverse arrangement test, J. Geophys. Res. Space Phys., 118, 636-641, doi: 10.1029/2012JA018216.

1.3.2 Presentations

The following is a list of key presentations presented at various national and international conferences:

- Yearby, K., **Aryan, H.,** Balikhin, M. A., Krasnoselskikh, V., and Agapitov, O. V. (2014), Observations of Chorus and Hiss by Double Star TC1. Geospace Revisited. Rhodes, Greece.

- **Aryan, H.,** Yearby, K., Balikhin, M. A., Krasnoselskikh, V., and Agapitov, O. V. (2014), The distribution of waves in the inner magnetosphere as a function of solar wind parameters. COSPAR Scientific Assembly. Moscow, Russia.

- **Aryan, H.,** Yearby, K., Balikhin, M. A., Krasnoselskikh, V., and Agapitov, O. V. (2013), Statistical study of waves distribution in the inner magnetosphere using geomagnetic indices and solar wind parameters. AGU Fall Meeting. San Francisco, California, USA

- Yearby, K., **Aryan, H.,** Balikhin, M. A., Krasnoselskikh, V., and Agapitov, O. V. (2013), The statistical study of Chorus waves using the Double star TC1 data. AGU Fall Meeting. San Francisco, California, USA

- Boynton, R., Balikhin, M. A., Alipudin R., Chiu, C., and **Aryan, H.** (2013), On the increase and decay of the electron fluxes at GEO. AGU Fall Meeting. San Francisco, California, USA.

- **Aryan, H.,** Balikhin, M. A., Taktakishvili, A., and Zhang, T. L. (2013), CME associated shocks. 2013 UK MHD – National Conference on Geophysical, Astrophysical and Industrial Magnetohydrodynamics. Glasgow, UK.

- **Aryan, H.,** Pakhotin, I., Balikhin, M. A., Walker, S. N., Boynton, R. J., Fedun, V., Pope, S. and Yearby, K (2013), Space plasma and solar physics. USES, The University of Sheffield. Sheffield, UK.

- **Aryan, H.,** Boynton R. J., and Walker S. N. (2012), Analysis of trends between solar wind velocity and energetic electron fluxes at geostationary orbit using the reverse arrangement test. AGU Fall Meeting. San Francisco, California, USA.

Chapter 2

Introduction to Magnetospheric Physics

2.1 Introduction

Solar activity at the Sun directly affects the near Earth geospace environment, especially, the population of trapped energetic particles within the Earth's magnetosphere that can damage or even destroy electronic components aboard crucial satellites. The Sun and its interaction with the Earth and other planets within the solar system has long been recognised and studied. The Earth's magnetic field interacts in a complex way with the Sun's Interplanetary Magnetic Field (IMF) and turbulent solar wind. This results in much of the complexity of magnetospheric weather. The ability to understand and forecast this complex solar terrestrial weather system is extremely important scientifically and to safeguard space based assets.

This chapter provides a brief insight into the magnetospheric physics. It attempts to describes the Sun and its complex interaction with the Earth's magnetic field that lead to the formation of a highly dynamic magnetosphere. In particular, this chapter describes some of the most important properties of the solar terrestrial environment and the physical processes that affect this environment.

2.2 The Sun and Solar Wind

The Sun, nearest star to Earth, is a large ball of ionised gas, consist of mainly hydrogen (90%) and helium (10%), held together and compressed under its own gravitational attraction. The Sun's magnetic fields are very intense and highly variable which are the drivers of most solar and geomagnetic activity. Charged plasma particles are constantly emitted from the surface of the Sun and races through space to the edge of the heliosphere [211] in the form of solar wind. At one Astronomical unit (Au) away from the Sun (the Earths orbit) the solar wind has an average speed of approximately 400 kms^{-1}, mean density of about 4 cm^{-3}, and mean interplanetary magnetic field magnitude of 5 nT. The solar wind may be observed as an extension of the Sun's outer atmosphere, the corona, into the interplanetary space called the heliosphere [134]. The solar wind consists of mainly electrons and protons, along with other heavier ionised atoms. These particles escape the Sun's gravity by acquiring high energies from the high temperatures of the corona. In 1960, *Gringauz et al.* [90] became the first group of scientists to measure the particle nature of the solar wind. Two years later, *Neugebauer and Snyder* [176] revealed that charged particles were emitted continuously from the

surface of the Sun, corona, using the Mariner 2 data. Coronal activity determines the solar wind velocity and composition.

2.2.1 Co-rotating Interaction Regions

Although solar wind always flows away from the Sun, its velocity and composition is not uniform. The solar wind varies routinely through the 27 day rotation of the Sun, known as the Carrington rotation [49]. Fast moving solar wind, generally originate in the coronal holes that extend equatorward from the magnetic poles of the Sun [131], interact with the slower moving solar wind, usually originate within the relatively dense coronal streamer [67, 86], and forms spiral shaped density compressions known as the Co-rotating Interaction Regions (CIRs) [29, 71, 82] that co-rotate with the Sun [83, 108]. Some fast streams do not exist through a complete rotation of the Sun. Hence, some studies suggest the use of the term Stream Interaction Regions (SIRs) [89] in order to include all short and long duration streams.

A schematic of a fast stream interacting with a slow stream, produced by *Pizzo* [191], is shown in Figure 2.1. At the leading edge of the fast stream, where the fast stream overtakes the slow stream, plasma material is compressed creating a region of high plasma density. In contrast, at the trailing edge of the stream a region of low plasma density is formed, where plasma material is rarefied [84, 112, 186, 221]. Subsequently, CIRs are commonly bounded by forward and reverse collisionless shock pairs that contributes to the acceleration of solar energetic particles in both the vicinity of the Earth and the interplanetary medium (this is explored further in Chapter 5).

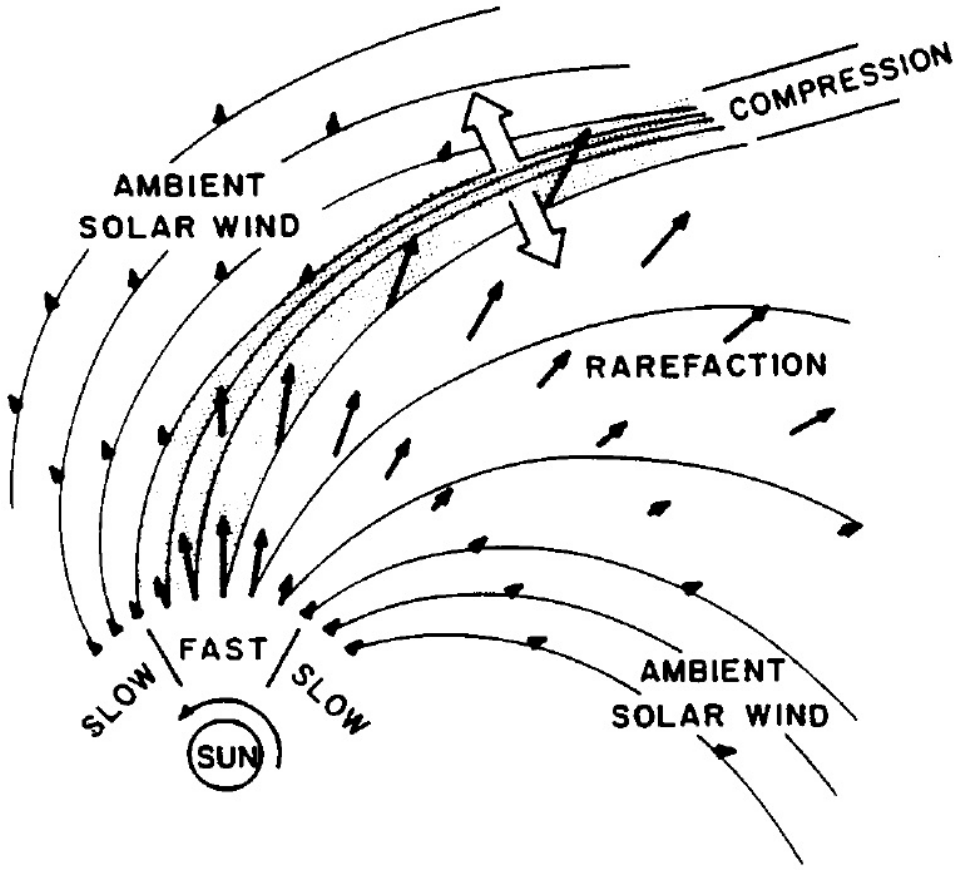

FIGURE 2.1: Schematic illustration of a fast stream interacting with a slow stream, adapted from *Pizzo* [191]. At the leading edge of the fast stream, where the fast stream overtakes the slow stream, plasma material is compressed creating a region of high plasma density. Conversely, at the trailing edge of the stream a region of low plasma density is formed, where plasma material is rarefied.

The pattern of coronal expansion varies as the Sun's magnetic field flip approximately every 11 years, known as the solar cycle. In 1843, *Schwabe* [210] discovered the solar cycle from the observation of sunspots, temporary dark localised regions on the surface of the Sun with very intense magnetic fields, over a period of approximately 17 years. During this cycle the Sun goes through periods of solar maximum and solar minimum defined by the number of observed sunspots. Sunspots are transient structures, with intense magnetic fields and lower temperature than the surroundings, that appear as dark photospheric structures in the photosphere of the Sun. The sunspot number forms the primary time series in

solar and solar terrestrial physics. The number of observed sunspots during solar maximum is highly variable and difficult to predict accurately. Generally, solar maximum corresponds to periods of high geomagnetic activity and vice versa.

2.2.2 Coronal Mass Ejections

Coronal Mass Ejections are sudden sporadically violent eruptions, mainly from the active regions of the corona, in which up to 10^{16} mg of coronal material [107, 113, 121] is propelled into the interplanetary space with speeds of hundreds to 2-3 thousands kms^{-1} [85, 103]. The solar wind velocity and composition can significantly change during such violent eruptions [88]. CME's were first observed with the OSO-7 white light coronagraph [242] and identified as an important component of solar coronal physics. Later in 1984, *Hundhausen et al.* [110] described CMEs as observable changes in coronal structures occurring on time scales of minutes to hours. A typical CME consists of a bright leading edge, a bright core, and a dark cavity [45], as shown in figure 2.2, using a white light coronal image. Figure 2.2 show a CME eruption observed by ESA and NASA Solar and Heliospheric Observatory (SOHO) mission on 2 December 2002, which is available online from SOHO online image gallery.

CMEs are the most energetic and the largest phenomena associated with the eruption of plasma from the Sun [158] which is caused by huge disturbances and changes in the coronal magnetic field [113]. The rate of CME eruption vary from around three CMEs during the solar maximum to about one CME every five days during the solar minimum. Almost all CMEs evolve into Interplanetary Coronal Mass Ejections (ICMEs) and interact with the solar wind as they propagate away from the Sun [80]. Slow moving CMEs are accelerated, while fast moving CMEs are

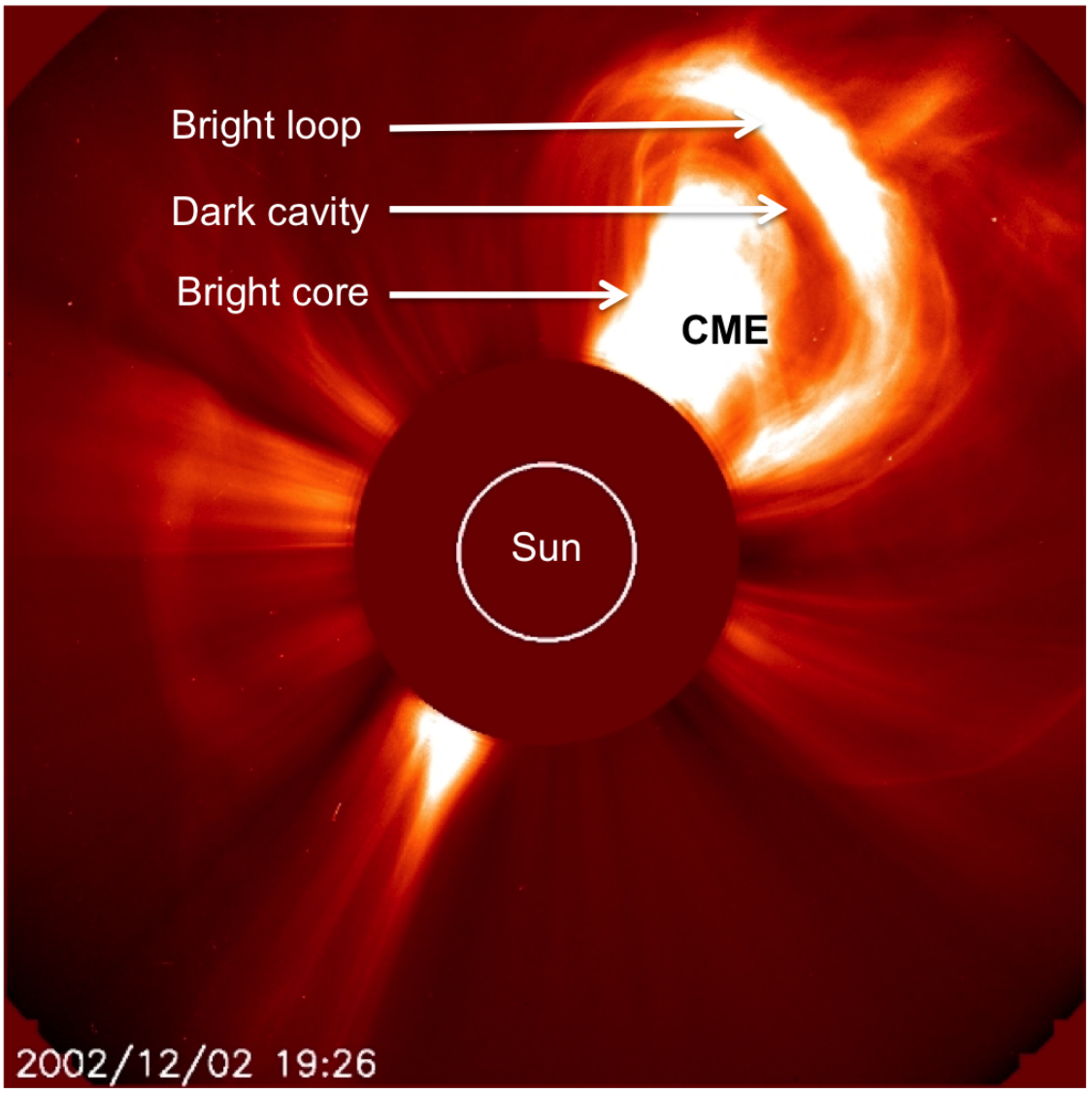

FIGURE 2.2: A white light coronal image showing the structure of a CME with a bright leading edge, a bright core, and a dark cavity. The CME eruption was observed by ESA/NASA SOHO mission on 2 December 2002. Available online from SOHO image gallery: http:// sohowww.nascom.nasa.gov/ gallery/ bestofsoho.html.

decelerated towards the speed of ambient solar wind [88]. The interaction of the CMEs with the solar wind frequently forms forward interplanetary collisionless shocks [41, 215] that contribute to the acceleration of Solar Energetic Particles (SEP) in both the vicinity of the Earth and the interplanetary medium.

The Earth directed CMEs, known as the halo CMEs, can engulf the Earth within approximately one to five days with the ability to cause severe geomagnetic storms

[87]. Helo CMEs are rare events that significantly increase the population of charged particles in the vicinity of the Earth, which may severely damage or destroy electronic components aboard satellites. According to the British Antarctic Survey, the halloween storm in 2003 led to the loss of one satellite and triggered malfunction in 47 other satellites. The effect of severe CMEs can also be felt on the ground, notably the power cut in Quebec, Canada, in 1989, which left many people without power. Extreme geomagnetic storms can force satellites to operate in safe mode, space station astronauts to take shelter in their most sheltered compartments, and airliners to fly alternative routes.

2.2.3 Solar Flares

Solar flares are sudden sporadically violent eruptions of energy, mainly from localised active regions of the Sun, in the form of electromagnetic radiation across the whole spectrum. Solar flares are the most powerful manifestations of solar activity. A solar flare can release large quantities of energy, up to 10^{25} J, which can heat materials to many millions of degrees in just a few minutes. Solar flares were first observed by *Carrington* [48] in 1859 using optical observations and they are classified according to their brightness in the x-ray wavelengths, as class C, M, and X. The C class flares are the smallest type of flares with minimal consequences. However, the M (medium size) class and the X (the largest) class flares can significantly affect the radio communication at the Earth and contribute to the acceleration of solar energetic particles in both the vicinity of the Earth and the interplanetary medium [208].

Solar flares occur as a result of huge disturbances and changes in the coronal magnetic field. The frequency of occurrence of solar flares vary with solar activity

in a similar fashion to the occurrence of CMEs. Although, solar flares and CMEs are closely related, there is an imperfect association of occurrence between them. They can occur together or separately [70, 174]. While, the largest solar flares, H-alpha flares, are generally involved with CMEs [214], the majority of smaller flares are not [174]. In contrast, large CMEs can be involved with large, small, or no solar flares [174, 213]. The duration of the flare usually determines its association with CMEs [214]. Long duration eruptive flares are more widely associated with CMEs, than impulsive confined flares [122].

2.2.4 Geomagnetic Indices

Coronal Mass Ejections and co-rotating interaction regions are large scale solar wind structures that can cause geomagnetic storms [81]. The intensity of the geomagnetic storm vary between different solar wind structures. Generally, the most intense geomagnetic storms are associated with CMEs, while CIRs typically cause less intense geomagnetic storms. Consequently, the implications for the acceleration and energisation of energetic particles in the vicinity of the Earth is different for different solar wind structures.

In space weather, geomagnetic indices are often used to quantify the ability, geo-effectiveness, of interplanetary solar wind structures to cause geomagnetic storms. Geomagnetic indices are ground based measurements that are compiled to quantify the state of the magnetosphere and how the Earth responds to a given type of solar wind structure [120]. The most commonly used geomagnetic indices are the Dst, the Kp, and the Ae index.

2.2.4.1 *Dst* Index

The Disturbance storm time (Dst) index is widely used to define the occurrence, duration, and magnitude of a geomagnetic storm. The Dst index is developed from low latitude hourly averaged horizontal component magnetograms to determine the ring current strength [226]. The four longitudinal observatories used to determine the Dst index are evenly distributed within near Earth equator in order to minimise the electrojet activities. Although the ring current is the most significant contributing current system in Dst index [92, 116, 196], it is possible that other low latitude current systems, such as substorms induced currents, magnetotail currents, and induced currents in the solid Earth may also contribute to Dst index [197, 247]. The Dst index is calculated using the follow formula 2.1:

$$\mathbf{Dst(t)} = \frac{1}{N_s} \sum_{t=1}^{N_s} \frac{\Delta H_i(t)}{cos(\theta_i)} \tag{2.1}$$

Where, N_s is the total number of longitudinal stations, $\Delta H_i(t)$ is the horizontal component of the geomagnetic field, and θ_i is the magnetic latitude.

Usually, the minimum value of the Dst index is used to distinguish between weak ($Dst \geq -30$ nT), moderate ($-50 \leq Dst < -30$ nT), strong ($-100 \leq Dst < -50$ nT), severe ($-200 \leq Dst < -100$ nT), and great ($Dst < -200$ nT) geomagnetic storms [151]. Figure 2.3 shows how the Dst index changed during different phases (initial phase, main phase, and recovery phase) of a storm recorded by ESA/NASA SOHO mission on 15 May 2005.

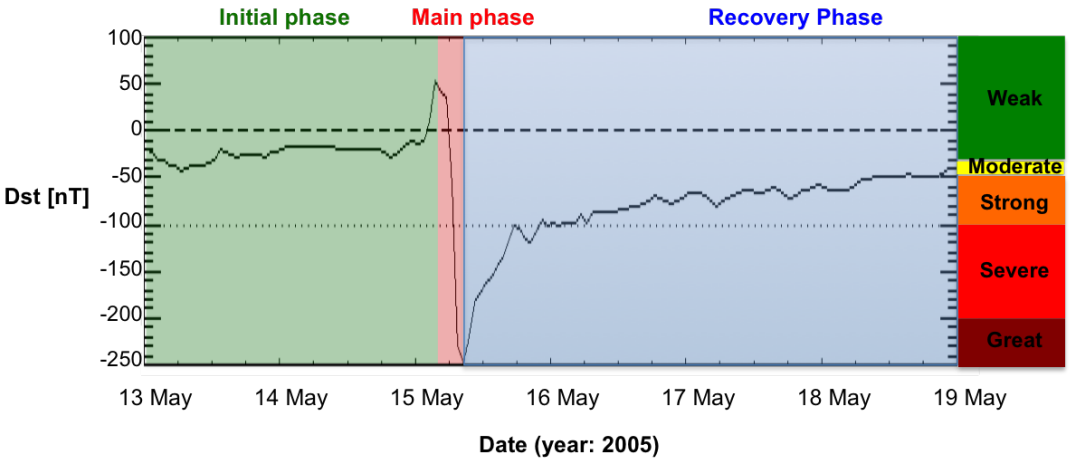

FIGURE 2.3: Dst index variation during initial phase (green), main phase (red), and recovery phase (blue) of a storm recorded by ESA/-NASA SOHO mission on 15 May 2005, courtesy of online CDAW Data Center: http://cdaw.gsfc.nasa.gov/ CME_list/ daily_plots/ dsthtx/ 2005_05/ dsthtx$_2$0050513.*html*.

2.2.4.2 Kp Index

The global Kennziffer planetary (Kp) index is derived from the sub-auroral Kennziffer (K) index [30] measurements obtained from 13 ground based midlatitude magnetometer stations [163]. The Kp index is defined as an integer between 0 (very quiet) and 9 (very disturbed) to distinguish between quiet ($Kp < 4$), moderate ($Kp = 4$), and active ($Kp > 4$) geomagnetic conditions. Generally, the Kp index is estimated every three hours to describe the overall geomagnetic disturbance. It is based on the fluctuation of the horizontal geomagnetic field relative to a quiet day [30, 163]. Figure 2.4 shows the estimated Kp index during a relatively moderate geomagnetic disturbance in October 2014.

The Kp has been readily available since its introduction by *Bartels et al.* [30] in 1939. Subsequently, it is one of the most widely used geomagnetic indices for studying the causes and consequences of geomagnetic activity. However, the sub-auroral stations that are used to compute the Kp index are largely sensitive to

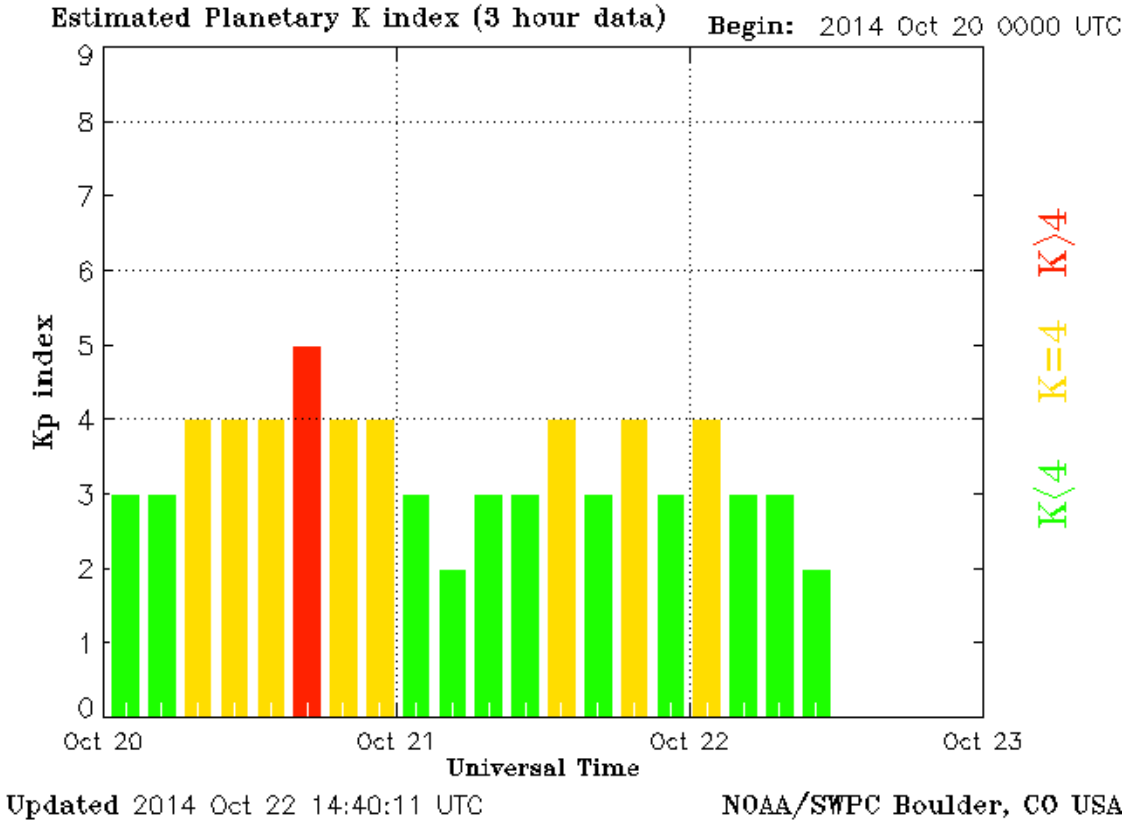

FIGURE 2.4: Estimated Kp index during a relatively moderate geomagnetic disturbance in October 2014, courtesy of online NOAA (national oceanic and atmospheric administration) SWPC (space weather prediction center): http://www.swpc.noaa.gov.

convection due to the effects of the inner edge of the plasma sheet [235]. This may introduce ambiguities in its interpretations [257].

2.2.4.3 *Ae* Index

The Auroral electrojet (Ae) index is compiled from the magnetograms of 12 auroral zone observatories distributed longitudinally in local time in the latitude region that is typical of the northern hemisphere auroral zone [59]. The Ae index describes the substorm intensity in the range 0 nT (low intensity) to over 1500 nT (very high intensity).

The *Ae* index is calculated every minute at each observatory from the northward horizontal component relative to a quiet day. It is based on the separation between the Auroral electrojet Upper (AU) and the Auroral electrojet Lower (AL) indices. The AU is a measure of the eastward auroral electrojet intensity, while the AL is a measure of the westward auroral electrojet intensity. Hence, the *Ae* index is simply the difference between the easterly and westerly auroral electrojets, defined as 2.2:

$$\mathbf{Ae(t)} = AU(t) - AL(t) \tag{2.2}$$

The *Ae* index has been widely used since its introduction by *Davis and Sugiura* [59] in 1966. However, the *Ae* index may not always be able to monitor the electrojet activity precisely [5, 154] due to the highly variable auroral ovals [98, 123, 153].

2.3 Earth's Magnetosphere

The Earth's magnetosphere is a highly complex and dynamic system formed as a result of solar wind interaction with the Earth's magnetic field. Inside the magnetosphere, the geomagnetic field determines the motion of the charged particles [79]. The magnetosphere has a very complex structure, as shown in Figure 2.5, which slows down, thermalises, and deflects solar wind around the Earth. Ultimately, providing a vital defensive shield from the energetic charge particles of the solar wind and cosmic rays. On the day side, the solar wind compresses the magnetosphere to a distance of approximately 10 times the radius of the Earth

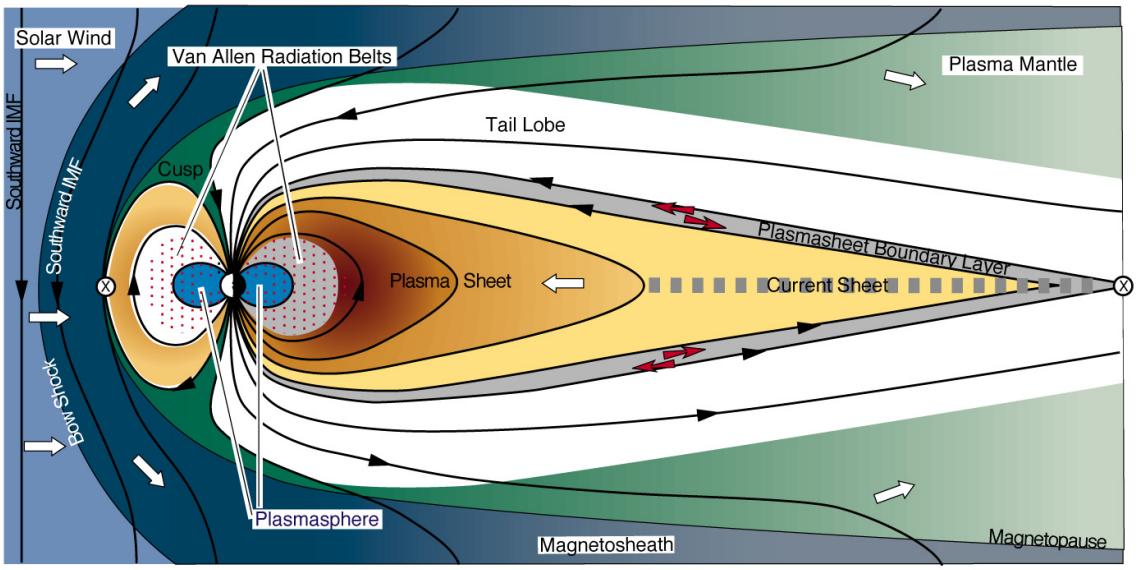

FIGURE 2.5: Schematic of the Earths magnetosphere, adapted from *Hill* [97], which points out the approximate location of the Bow shock, magnetosheath, magnetopause, plasmasphere, Van Allen radiation belts, and the cusps.

(R_E) with the sunward boundary located where the external pressure of the solar wind equals the internal pressure of the geomagnetic field [249]. In contrast, the solar wind stretches out the night side magnetosphere to a possible distance of $1000R_E$ in the direction away from the sun, creating the tail lobes and the plasma sheet that form the long magnetotail [249]. The current sheet lies in the centre of the tail, embedded within the plasma sheet, a region of closed field lines in the equatorial magnetotail that extends from the magnetotail to the geostationary orbit separating the north and south tail lobes. The magnetic field lines, tail lobes, current sheet, and plasma sheet form the basis of auroral physics.

The Earth's magnetosphere is highly dependent on the level of solar activity and on the conditions in the interplanetary medium. Generally, geomagnetic storms compress the magnetosphere on the day side but extends the magnetotail on the night side. The initial interaction between the solar wind and the Earth's magnetosphere occur at the Bow shock, which is formed upstream of the magnetosphere,

at a distance of approximately 3 to 4 R_E in front of the magnetopause. In contrast to the shock wave formed in front of an aircraft moving at supersonic speeds, the bow shock is a stationary and collisionless shock. At the bow shock, the solar wind is slowed down, compressed, thermalised, and deflected around the Earth. The shocked solar wind plasma occupies the region downstream of the bow shock, known as the magnetosheath. The magnetopause separates the shocked solar wind plasma from the plasma of the inner magnetosphere creating a current layer. The magnetopause current flow is centred on the northern and southern magnetic null points[52, 53], known as the cusps, where the magnetic field lines diverge, providing the magnetosheath plasma direct access to the ionosphere, the upper region of the Earth's atmosphere.

The inner part of the magnetosphere, known as the plasmasphere, is located just above the upper ionosphere consisting of dense, low energy plasma. Plasma within the plasmasphere co-rotates with the Earth due to the high electric conductivity of the ionosphere. In 1963 *Carpenter* [47] discovered the plasmasphere through the analysis of Very Low Frequency (VLF) whistler wave data. It was later found that the plasmasphere occupies approximately the same region of the inner magnetosphere as the Van Allen radiation belt (between $L = 2$ and $L = 7$). Recently, *Darrouzet et al.* [58] reported that the link between the plasmapause (the outer boundary of the plasmasphere) and the radiation belt boundaries is defined by the level of geomagnetic activity. The radiation belt boundary position is reportedly less variable than the plasmapause position especially during low geomagnetic activity enhancements. In fact the plasmasphere can stretch out to beyond the outer boundary of the Van Allen radiation belts during low geomagnetic activity.

The structures of the bow shock, magnetosheath, and magnetopause are all very

sensitive to solar wind properties. The level of magnetospheric activity strongly determines the shape, size, and dynamics of the plasmasphere. While the magnetosphere ultimately deflects most high energy charged particles from the solar wind around the Earth, at times some high energy charged particles enter the magnetosphere through variety of means [10, 188, 199] and become trapped in the Van Allen radiation belts. Particle entry is strongly influenced by the orientation of the IMF and is enhanced during periods of southward IMF [199].

2.4 Van Allen Radiation Belts

The Van Allen radiation belt is a torus of energetic charged particles magnetically trapped in the mirror geometry of the Earths magnetic field. The Van Allen radiation belt was named after James Van Allen who discovered the inner belt in 1958. The outer belt was detected by Sputnik 3, which was later confirmed by Explorer III mission [248]. Energetic particles, in the energy range of hundred keV to tens of MeV, are mainly trapped within the Earths inner ($1.1 < L < 2$) and outer ($3 < L < 7$) radiation belts [190] separated by a region of low electron density known as the slot region ($2 < L < 3$). The inner radiation belt is relatively stable and the flux of energetic particles only varies during intense geomagnetic storms [40, 146, 156, 171]. The inner radiation belt consist of mainly protons that are largely concentrated in the Earth's equatorial plane with the highest flux observed at around 1.5 L.

On the other hand, the outer radiation belt is highly dynamic and the flux of energetic electrons can vary by several orders of magnitude, on a timescale of a few hours to days, during storms and other disturbance [15, 19, 34, 57, 192,

193, 245] due to a competition between various acceleration and loss processes [230, 236, 246]. The outer belt is larger and more diffuse, which consists of mainly electrons [54, 252] largely concentrated in the Earth's equatorial plane. The peak flux usually occur in the region of $4 < L < 5$.

Meanwhile, the slot region is widely accepted to have formed as a result of slow inward radial diffusion from a source population in the outer zone and precipitation losses from the inner magnetosphere, due to pitch angle scattering by very low frequency waves, such as plasmaspheric hiss [157] and magnetosonic waves [173]. Evidence points to whistler mode chorus waves as the main source of plasmaspheric hiss [39] which is also accountable for the decay of energetic electrons in the outer radiation belt during relatively quiet times [232]. The slot region is temporarily filled when enhanced outer radiation belt electrons are injected inward during intense geomagnetic activity, [200]. Occasionally, intense geomagnetic storms may also produce a third temporary radiation belt [23]. However, the electrons decay following the storm time to reform the quiet time slot region and two zone radiation belt structure. In fact, the whole electron radiation belts are constantly decaying and episodically reforming. The new formed belts may possess very different properties to its predecessor.

The radiation belts occupy a vast region of geospace near Earth where many important communication, navigation, Earth observation, and defence satellites operate. Figure 1.1 presents a schematic of the Earth's radiation belts together with some of the most common satellite orbits that pass through the radiation belts. Trapped energetic radiation belt electrons constitute a significant hazard to spacecraft electronic components [12]. The communications satellites largely operate in geostationary orbit, an equatorial orbit with an orbit period equal to

the Earth's rotation period, which is located at 6.6 R_E, the edge of the outer radiation belt. Geostationary satellites appear fixed in the sky to an observer on the surface of the Earth, a very desirable advantage for communication technology. The navigation satellites, such as GPS satellites, operate in Medium Earth Orbit (MEO), subsequently passing through the high flux regions of the outer radiation belts. The international space station and other satellites used for Earth observation and defence that operate in Low Earth Orbit (LEO) are also not immune to energetic electrons as they may be exposed to dangerous levels of radiation during very intense storms [22]. Energetic particles can penetrate deep into the atmosphere by gyrating along geomagnetic field lines at the cusps where geomagnetic field is relatively weak.The accumulation of charged electrons on the surface of the spacecraft and subsequent discharge is a major hazard [93].

2.4.1 Radiation Belt Particles

Radiation belts consist of mainly protons and electrons trapped by the Earth's magnetic field. The composition and temporal variability of the inner and outer radiation belts is different [198, 250]. The main sources of energetic electrons found trapped in the Van Allen radiation belts are thought to be the solar wind and the ionosphere [144]. However, the energy of the radiation belt electrons is considerably higher (generally in the range of hundred keV to tens of MeV) compared to the low energies of the solar wind electrons (approximately 10 eV), the magnetosheath electrons (around 30 eV), the central plasmasheet electrons (between 500 eV to 2000 eV), and the ionosphere electrons (topically less than 1 eV). Electrons are transported predominantly through through inward radial diffusion and fast injection by fluctuating electric and magnetic fields. The former transport

mechanism violate the particles third adiabatic invariants [74, 135]. Though, the energy gained is limited by the ratio of the magnetic field magnitudes within the region of radial transport. This indicates that the electrons are energised through various complex processes. The precise mechanisms that affect the acceleration and loss of energetic radiation belt electrons is an active area of research. The most probable mechanisms include, the interaction of gyroresonant particles with plasmaspheric waves [24, 62, 104, 138, 166, 209, 220, 239] and particle acceleration by interplanetary collisionless shock waves, associated with CMEs and CIRs [145, 201]. Figure 2.6 illustrates some of the physical processes that affect the dynamics of the Earth's radiation belts including, inward radial diffusion of solar wind, interaction of gyroresonant particles with plasmaspheric waves, and particle acceleration in interplanetary collisionless shock waves.

The flux of relativistic electrons in the outer radiation belt respond to majority of geomagnetic disturbances [193]. In 2003 *Reeves et al.* [193] examined 276 geomagnetic storms of which 53% increased, 19% decreased, and the remaining 28% left the flux of relativistic electrons in the outer radiation belt relatively unchanged. Generally, the main phase of a geomagnetic storm triggers a rapid decease in the flux of relativistic electrons, while during the recovery phase, the flux increases back up to or beyond the pre-storm level [75]. The enhancement of energetic electrons is linked to CIR driven [11, 35, 148, 189, 192, 256] and CME driven [20, 21, 192, 212] storms. It has been widely reported that in the outer region of the radiation belt, the CIR driven storms are more effective in the electron flux enhancement than the CME driven storms [60, 124, 172].

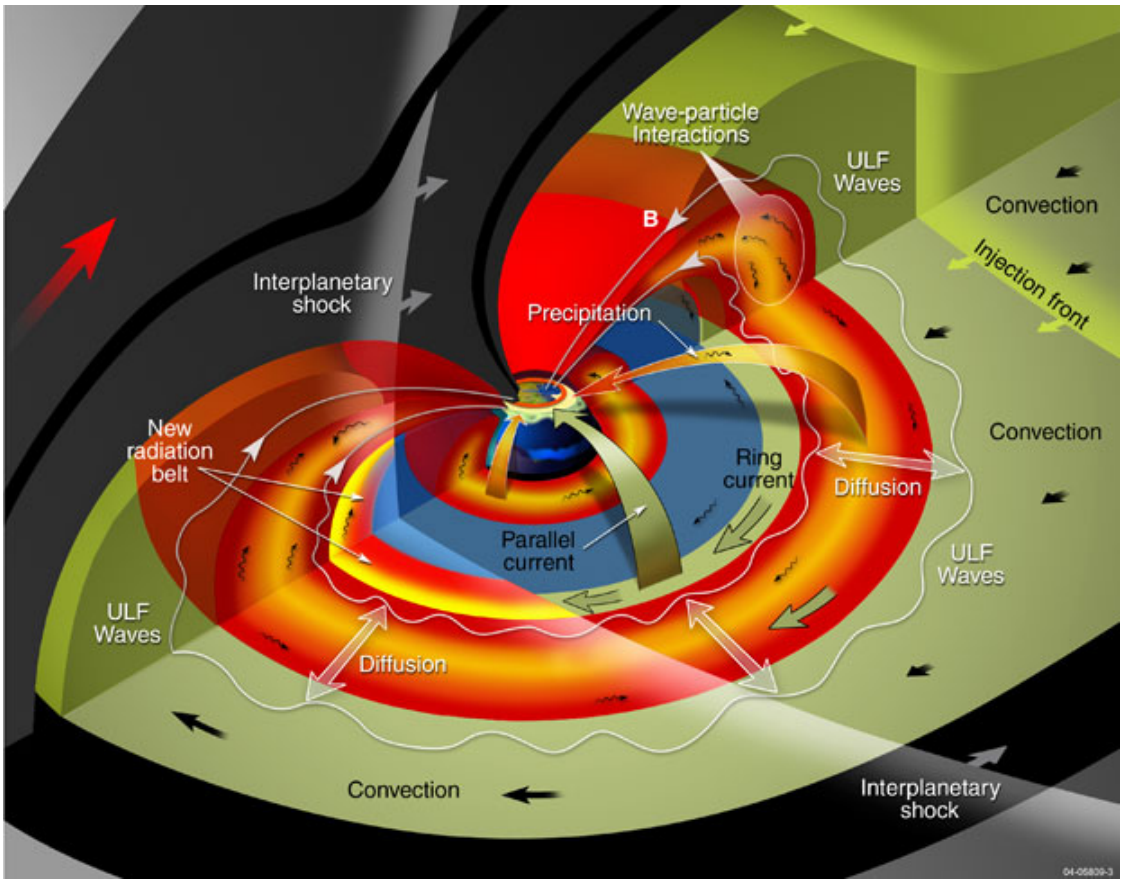

FIGURE 2.6: Schematic of physical processes that affect the dynamics of the radiation belts, adapted from *Mauk et al.* [160]

2.4.2 Motion of Particles

The Earth's magnetic field, which acts similar to a magnetic dipole, control the motion of the energetic particles within the radiation belts. Radiation belt particles encircles the Earth in a complicated orbital motion constrained by the magnetic field. The behaviour of these energetic charged particles in electric and magnetic fields is described by the electromagnetic Lorentz force law:

$$\mathbf{F_L} = q\mathbf{E} + q\mathbf{v} \times \mathbf{B} \tag{2.3}$$

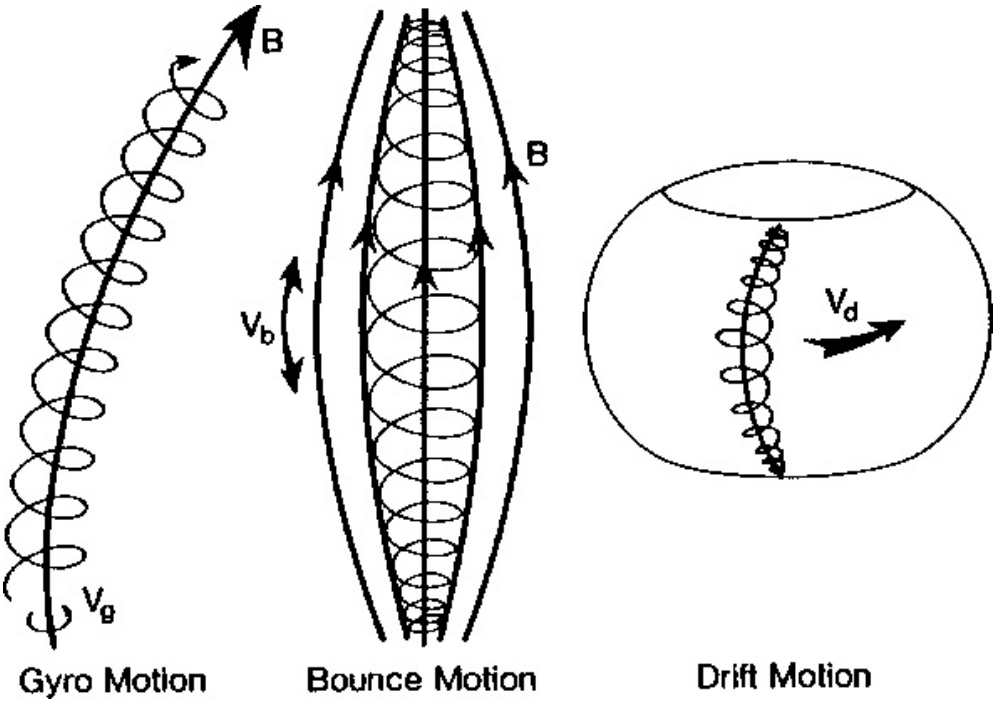

FIGURE 2.7: Schematic of particle motion in a magnetic field, adapted from *Kivelson and Russell* [129]

In equation 2.3, F_L is the electromagnetic Lorentz force, q is the particle charge, **E** is the electric field, **B** is the magnetic field, and v is the velocity of the particle. Once the energetic particles are trapped their motion is confined to gyration around the magnetic field lines, bounce along the field lines between magnetic mirror points, and drift around the Earth [129].

The particle gyromotion around the magnetic field lines occur due to particle's perpendicular velocity component to the local field line vector. On the other hand, any parallel velocity component to the local magnetic field line will cause the particles to bounce along the field line. Meanwhile, the particle drifts around the Earth due to the magnetic gradient and curvature drift. The three types of motions are mostly uncoupled due to the fact that the frequencies associated with each of these motions are quite different, i.e., the bounce frequency is much larger than the drift frequency, while the gyro frequency is much larger than both the bounce

and drift frequencies. A schematic of the three types of particle motions, adapted from [129], is illustrated in figure 2.7. Electrons typically drift eastward around the Earth, they bounce between the stronger magnetic fields in the northern and southern hemisphere and gyrate around the local magnetic field. Generally, high energy particles bounce and drift faster than particles with lower energy.

Chapter 3

Energetic Electron Fluxes at Geostationary Orbit

3.1 Introduction

Energetic electron fluxes at geostationary orbit represent a serious hazard to satellite electronic components and other space based systems. The severity of the hazard is determined by the level of energetic electron flux [14, 17]. Evidence suggest a strong correlation between the occurrence of these fluxes and subsequent operation anomalies or even failures of satellites, especially at geostationary orbit. Therefore, accurate prediction of energetic electron fluxes at geostationary orbit could mitigate the damage caused to the satellites and other space based systems [12]. Energetic electrons are mainly trapped in fairly stable orbits within the Earth's outer radiation belt ($3 < L < 7$). The flux of energetic electrons in the Earth's outer radiation belt can vary by three orders of magnitude during

magnetic storms and other disturbances. The solar wind is the driver of radiation belt dynamics that can lead to enhancement [20, 229] and loss [179] of the relativistic electrons. The solar wind ultimately controls the population of the energetic electrons at geostationary orbit. Thus, understanding the relationship between flux of energetic electrons and the main solar wind parameters will lead to better predictions of energetic electron fluxes at geostationary orbit.

While the dynamics of low energy particles that forms the ring current are more or less understood [76] mainly through ring current modelling (e.g. [72, 73, 115, 117–119, 149]), a comprehensive physical model capable of explaining the formation of high energy fluxes in the radiation belts which is universally accepted has not been developed yet. Among the most prominent physical processes are the radial diffusion which may be enhanced due to Ultra Low Frequency (ULF) waves and pulsations (e.g. [61, 104–106, 209]) or the interaction with waves within the outer radiation belt itself [6, 7, 102, 182, 217–219, 227–229, 231]. It is accepted at present that both of these processes play significant role in the electron energisation but their relative importance under different solar wind conditions is not yet understood.

The relationship between solar wind parameters and energetic electron fluxes at the outer radiation belt has been studied widely for many decades. In 1966, *Williams* [256] became the first to suggest a link between periodic increases in the trapped relativistic electron populations and the upsurge in the solar wind kinetic energy density. Later in 1979, *Paulikas and Blake* [189] compared the relativistic electron fluxes of three different energy levels (> 0.7, > 1.55, and > 3.9 MeV) with solar wind parameters (solar wind velocity, IMF, and sector polarity) averaged over different timescales (daily, 27 days, and 6 months). The latter study identified a

roughly linear correlation between solar wind velocity and energetic electron fluxes across all three energy levels. This was remarkable result that shaped the radiation belt studies, space weather forecasting, and the studies of solar wind radiation belt coupling. However, in 2011 *Reeves et al.* [194] restudied the results of *Paulikas and Blake* [189] using thirty years of daily averaged energetic electron fluxes and solar wind velocity. *Reeves et al.* [194] discovered that the relationship between energetic electron fluxes and solar wind velocity was in fact considerably more complex than previously suggested by *Paulikas and Blake* [189]. According to the latter study, the correlation between solar wind velocity and energetic electron fluxes appeared to have a triangle shape with a distinct velocity dependent lower limit, but a velocity independent upper limit as presented in Figure 3.1, which shows s scatterplot of daily averaged V_{SW} and electron flux in the energy range $1.8 - 3.5$ MeV for the year 1994. The Figure show a triangle shaped distribution with a distinct velocity dependent lower limit, but a velocity independent upper limit.

The solar wind parameters that control the energetic electron fluxes at geostationary orbit have been analysed using various methodologies (e.g. [28, 159, 181, 184]) leading to different outcomes. In 2011, *Balikhin et al.* [28] applied the Nonlinear Autoregressive Moving Average Modelling (NARMAX) algorithm to model the evolution of energetic electrons fluxes at geostationary orbit. NARMAX is an effective methodology used in complex nonlinear systems [25, 33, 36] and has been shown to work well for obtaining a solar wind coupling function [42] and for deriving models for the Dst index [36, 43].

Unexpectedly, *Balikhin et al.* [28] identified the solar wind density as the most important control parameter for electrons in the energy range $1.8 - 3.5$ MeV. They

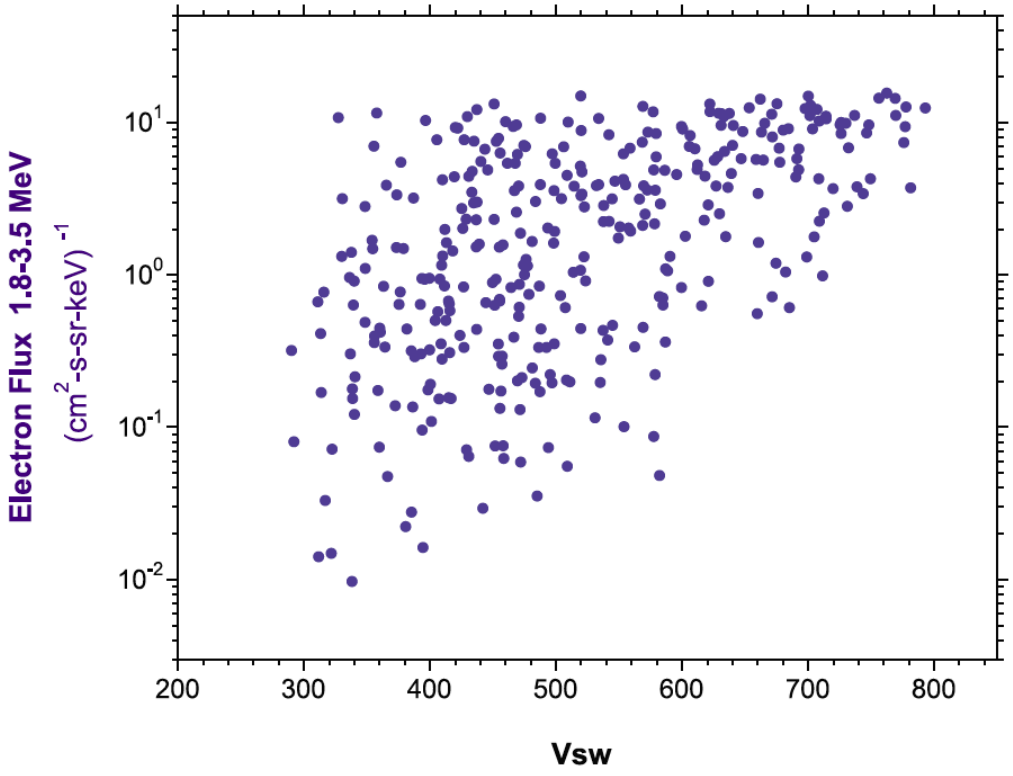

FIGURE 3.1: A scatterplot of daily averaged V_{SW} and electron flux in the energy range $1.8 - 3.5$ MeV for the year 1994. The Figure show a triangle shaped distribution with a distinct velocity dependent lower limit but a velocity independent upper limit. Figure adapted from *Reeves et al.* [194] Figure 5(B).

went on to demonstrate that for electrons measured in the energy range $1.8 - 3.5$ MeV and solar wind densities measured in the range $2.2 \leq n < 2.3$ cm^{-3}, the flux of energetic electrons increased as solar wind velocity increased until a saturation velocity was reached. Beyond this point an increase in solar wind velocity was statistically not accompanied with energetic electron flux enhancement as shown in Figure 3.2. Figure 3.2 clearly show a velocity dependent lower limit and a velocity independent upper limit with the transition taking place approximately in the solar wind velocity range 550 kms^{-1} $< V_{SW} <$ 650 kms^{-1}. However, the precise saturation velocity and its dependence upon solar wind density is not clear.

This chapter investigates the saturation velocity and its dependency upon solar wind density for electrons measured in the fixed energy range $1.8 - 3.5$ MeV and

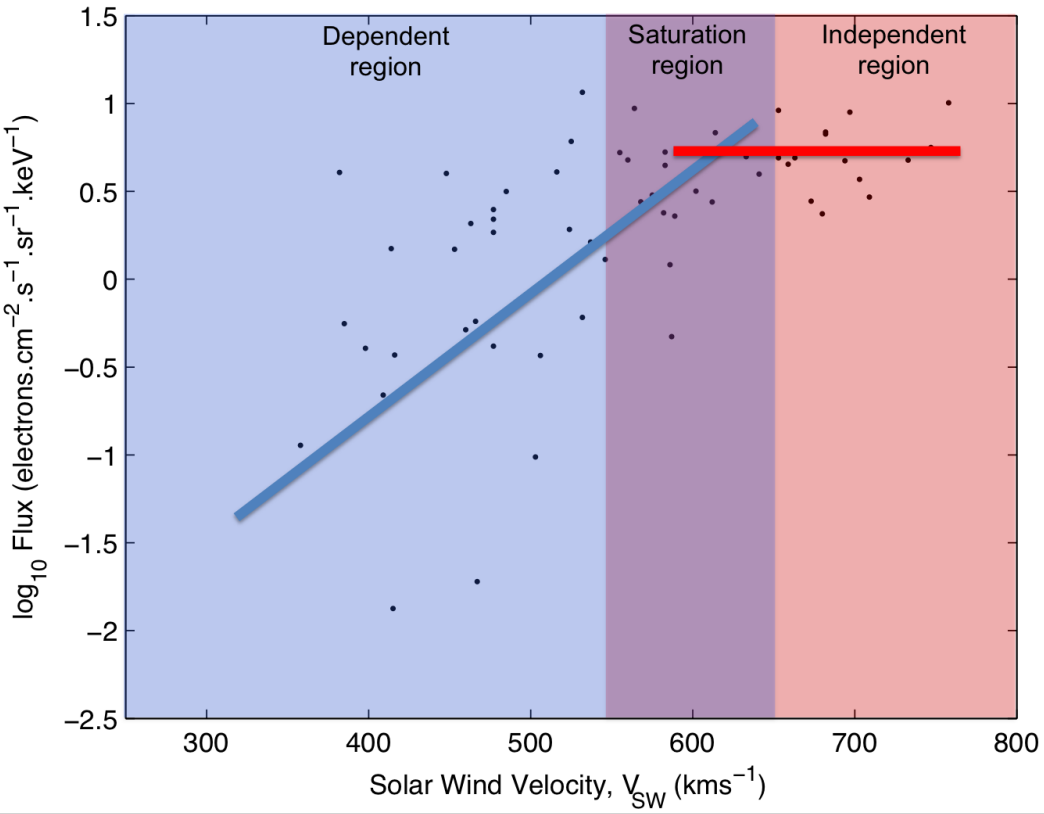

FIGURE 3.2: A scatterplot of daily averaged energetic electron fluxex and solar wind velocity for electron fluxes measured in the energy range 1.8−3.5 MeV and solar wind density measured in the range $2.2 \leq n < 2.3$ cm^{-3} based on Figure 2(d) *Balikhin et al.* [28]. The figure show a velocity dependent lower limit (blue shade) and a velocity independent upper limit (red shade) with the transition taking place in the solar wind velocity range 550 kms^{-1} $< V_{SW} <$ 650 kms^{-1} (purple shade)

for solar wind densities below 6.0 cm^{-3}.This will provide better understanding of the physical processes within the geostationary orbit and could lead to improved modelling and forecasting of fluxes of high energy electrons in the terrestrial radiation belts. This can potentially help mitigate the damage to satellites and other space based systems.

3.2 Data Set and Methodology

The electron flux data are collected by Los Alamos National Laboratory using the Energetic Spectrometer for Particles (ESP) instrument [162] aboard their satellites between 22 September, 1989 to 31 December, 2009. This instrument measured the flux of energetic electrons in various energy ranges. In this study, the analysis is based on one day averages of electron fluxes measured in the range $1.8-3.5$ MeV. These data are available as auxiliary material to the paper by *Reeves et al.* [194] at ftp:/ftp.agu.org/apend/ja/2010ja015735, which also contain a description of the data set preparation. The solar wind density and velocity data are available online at OMNIWeb database.

Temporal changes in the solar wind velocity and density are not observed immediately in the energetic electron fluxes. The magnetospheric system introduces a time delay which depends on the particle energy [147]. The time delay between changes in solar wind velocity and enhancement of the electron fluxes is due to in situ energisation of electrons by very low frequency waves and the time taken for the electrons to diffuse inward to geostationary orbit in response to the changes in the solar wind. It has been shown by various methodologies that the time delay increases with increasing energy [42, 147, 194]. Thus, the time delays between solar wind density and solar wind velocity for the electron fluxes measured in the fixed energy range $1.8-3.5$ MeV are estimated to be one and two days respectively [42, 147, 194].

Figure 3.2 emphasises that the transition between the dependent lower limit and the independent upper limit occur at some saturation velocity approximately in the solar wind velocity range $550\ \text{kms}^{-1} < V_{SW} < 650\ \text{kms}^{-1}$. However, the precise

velocity of saturation is not clear. This saturation velocity can be estimated mathematically using the reverse arrangement test. The reverse arrangement test is an effective methodology widely used to identify whether there is a significant trend in a set of N observations arranged in an increasing order. The Reverse arrangement test is a non-parametric or distribution-free trend test where no assumption is made concerning the probability distribution of the data being evaluated [31, 32]. In this case, a set of N observations arranged in an increasing order of solar wind velocity can be tested for the presence of a trend by calculating the number of times $EEF_i < EEF_j$ for which $i < j$ (EEF represents the electron flux values). The sum of all such inequalities is called A_t which is given by equation 3.1:

$$\mathbf{A_t} = \sum_{i=1}^{N-1} A_i \tag{3.1}$$

where

$$\mathbf{A}_i = \sum_{j=i+1}^{N} R_{ij} \tag{3.2}$$

and

$$\mathbf{R}_{ij} = \begin{cases} 1 & if\ EEF_i < EEF_j \\ 0 & Otherwise \end{cases} \tag{3.3}$$

The value of A_t is then compared with the upper (A_{Upper}) and lower (A_{Lower}) boundaries of the acceptance range (Table 5.1) to determine whether the hypothesis is true or false. The hypothesis that the observations are dependent with 95% confidence is accepted only if A_t falls within the acceptance range. Similarly,

TABLE 3.1: Provides the acceptance range for $z = 1.96$ which corresponds to a 95% confidence level. Also provides the values of A_n in the test for no trend for electron fluxes measured in the range $1.8 - 3.5$ MeV and solar wind density measured in the range $2.2 \leq n < 2.3$ cm^{-3}. In this case, there are 66 data points within the data set.

No. of data	A_{Lower}	A_{Upper}	$A_n(2.2 \leq n < 2.3)$
4	0	6	0
5	1	9	1
6	2	13	5
8	6	22	16
10	11	33	31
20	64	125	100
26	123	213	126
27	133	228	127
30	162	272	N/A
40	305	474	N/A
50	496	729	N/A
60	731	1038	N/A
66	901	1255	N/A
70	1014	1400	N/A
80	1382	1815	N/A
90	1721	2283	N/A
100	2145	2804	N/A

the set of N data points arranged in an increasing order of solar wind velocity can also be tested for the absence of a trend by calculating the number of times $EEF_i > EEF_j$ for which $i < j$. Here the sum of all such inequalities is called A_n which is calculated in a similar way to A_t by substituting $EEF_i > EEF_j$ in Equation 3.3. Again the value of A_n is compared with the upper (A_{Upper}) and lower (A_{Lower}) boundaries of the acceptance range (Table 5.1) to determine whether the hypothesis is true or false. In this case, the hypothesis that the observations are independent with 95% confidence is accepted only if A_n falls within the acceptance range. The values of the acceptance range A_{Upper} and A_{Lower} are calculated using equations 5.7 and 3.5 [31, 32] where the value of z determines the confidence level i.e., $z = 1.96$ represents 95% confidence level. Larger values of z represent higher confidence level and vice versa.

$$\mathbf{A_{Upper}} = \mathbf{z}\sqrt{\frac{\mathbf{(2N+5)(N-1)N}}{\mathbf{72}}} + \frac{\mathbf{N(N-1)}}{\mathbf{4}} - \mathbf{0.5} \tag{3.4}$$

$$\mathbf{A_{Lower}} = \frac{\mathbf{N(N-1)}}{\mathbf{4}} + \mathbf{0.5} - \mathbf{z}\sqrt{\frac{\mathbf{(2N+5)(N-1)N}}{\mathbf{72}}} \tag{3.5}$$

In general, large enhancements in the electron fluxes occur during fast solar wind conditions. Thus, a simple reverse arrangement test will not be adequate to identify the saturation velocity. This is because, a forward reverse arrangement test for a trend for any number of data is likely to return positive and fail to identify the saturation velocity. However, it is possible to estimate the saturation velocity by assuming there is no correlation between energetic electron flux and solar wind velocity for solar wind velocities larger than the saturation velocity (i.e. the upper fast region). In this case, the reverse arrangement test for the absence of a trend for any number of data with solar wind velocity higher than the saturation velocity would be expected to produce values of A_n that falls within the acceptance range confirming that energetic electron flux and solar wind velocity are independent (here the data is arranged in an increasing order of solar wind velocity and A_n is obtained by comparing the corresponding electron flux values). Hence, the value of the saturation velocity is estimated by repeatedly running the test for the absence of a trend with an increasing number of data points (t), starting with the 4 highest values of V_{SW} ($t = 4$) (reverse arrangement test requires at least four values) and consecutively adding the next highest value of V_{SW} ($t = 4, 5, \cdots, N$. I.e. look for the absence of a trend in the subset $t = 4, 5, \cdots, N$ as the number of data

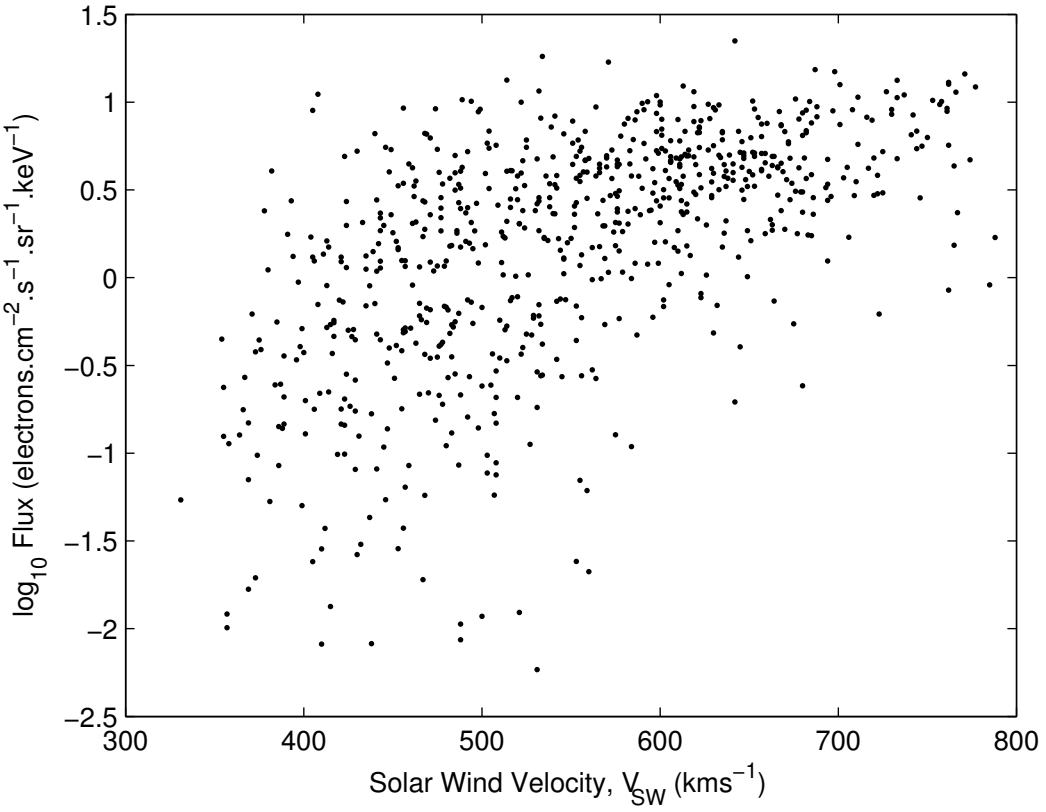

FIGURE 3.3: A scatterplot of energetic electron fluxes as a function of solar wind velocity for electron fluxes measured in the energy range $1.8 - 3.5$ MeV and solar wind density measured in the range $2.0 \leq n < 3.0$ cm^{-3}. Here there are too many data points in the data set which is clearly obscuring information.

points (t) in the subset increases step by step). The saturation velocity is then determined as the point where A_n first falls outside the acceptance range. This is confirmed by a forward reverse arrangement test for the presence of a trend for the remaining ($t_r = N - t$ when $t \geq 4$) data points below the saturation velocity (i.e. the lower slow V_{SW} region).

It is important to understand how the saturation velocity varies with different solar wind density range for electrons in the fixed energy range $1.8 - 3.5$ MeV. This can be analysed by applying the reverse arrangement test to various other solar wind density ranges with electron flux measured in the fixed energy range $1.8 - 3.5$ MeV. In this study the data in the solar wind density range $2 - 6$cm^{-3}

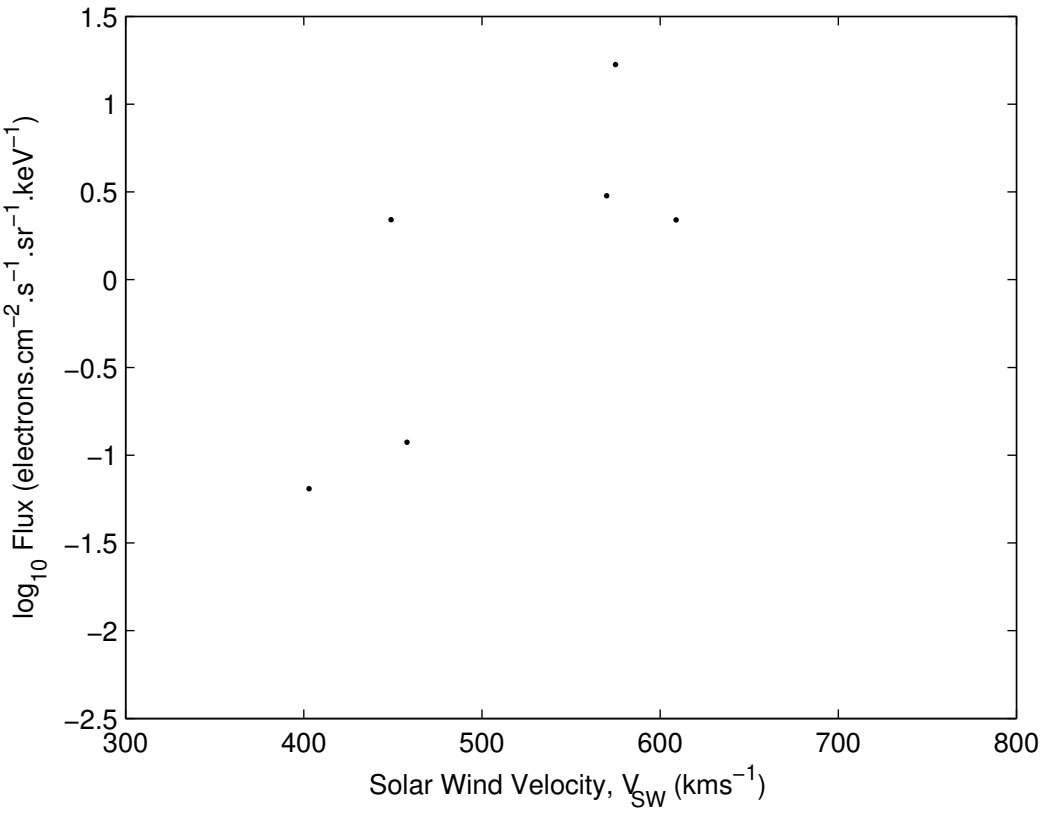

FIGURE 3.4: A scatterplot of energetic electron fluxes as a function of solar wind velocity for electron fluxes measured in the energy range $1.8 - 3.5$ MeV and solar wind density measured in the range $1.0 \leq n < 1.1$ cm^{-3}. Here there are only 6 data points in the data set which provides negligible information.

were grouped in 0.1 cm^{-3} solar wind density bins. However, since solar wind densities < 2cm^{-3} occur rarely the following larger solar wind density bins were used $0.5 \leq n < 1.3$, $1.3 \leq n < 1.6$, $1.6 \leq n < 1.8$ and $1.8 \leq n < 2.0$. These bin sizes were chosen to maintain adequate and approximately equal number of data points in each subset. This is important since having too many data points in the data set can obscure information, whilst too few data points in the data set may not provide the true representation. For example in Figure 3.3 the solar wind density bin is 1.0 cm^{-3} $(2.0 - 3.0$cm$^{-3})$ which includes a large number of data points (733) and clearly obscuring information. On the other hand, in Figure 3.4 the solar wind density bin is 0.1 cm^{-3} $(1.0 - 1.1$cm$^{-3})$ for low solar wind density

where the occurrence is rare. In latter case there are only 6 data points in the data set which provides negligible information. In addition, higher solar wind densities, above 6 cm^{-3}, only occur under a narrow range of low solar wind velocities and will not be considered in this study.

3.3 Results and Discussions

The reverse arrangement test was applied to electron fluxes measured in the energy range $1.8 - 3.5$ MeV and solar wind density measured in the range $2.2 \leq n < 2.3$ cm^{-3} as presented in Figure 3.2 in order to estimate the saturation velocity (the data were arranged in an increasing order of solar wind velocity). In the present case, a reverse arrangement test for the absence of a trend for the 4 highest V_{SW} data points ($t = 4$) returned $A_n = 0$ which fell within the acceptance range confirming the absence of a trend (Figure 3.5 and Table 5.1). The same test for the 5 highest V_{SW} data points ($t = 5$) returned $A_n = 1$ which again fell within the acceptance range. This process was repeated until A_n fell outside the acceptance range. In this case, a test for the absence of a trend for the 27 highest V_{SW} data points ($t = 27$) returned $A_n = 127$ which fell outside the acceptance range indicating that there is no evidence that electron flux and solar wind velocity are independent. Therefore, the final value of A_n that fell within the acceptance range was $A_n = 126$ which corresponds to the 26 highest V_{SW} data points ($t = 26$) within the subset. This implies that with 95% confidence there is no trend in the 26 highest V_{SW} data points. The reverse arrangement test for the presence of a trend for the remaining 40 lowest V_{SW} data points ($t_r = N - t = 66 - 26 = 40$, there are a total of 66 data points in this data set) returned $A_t = 463$ which fell within the

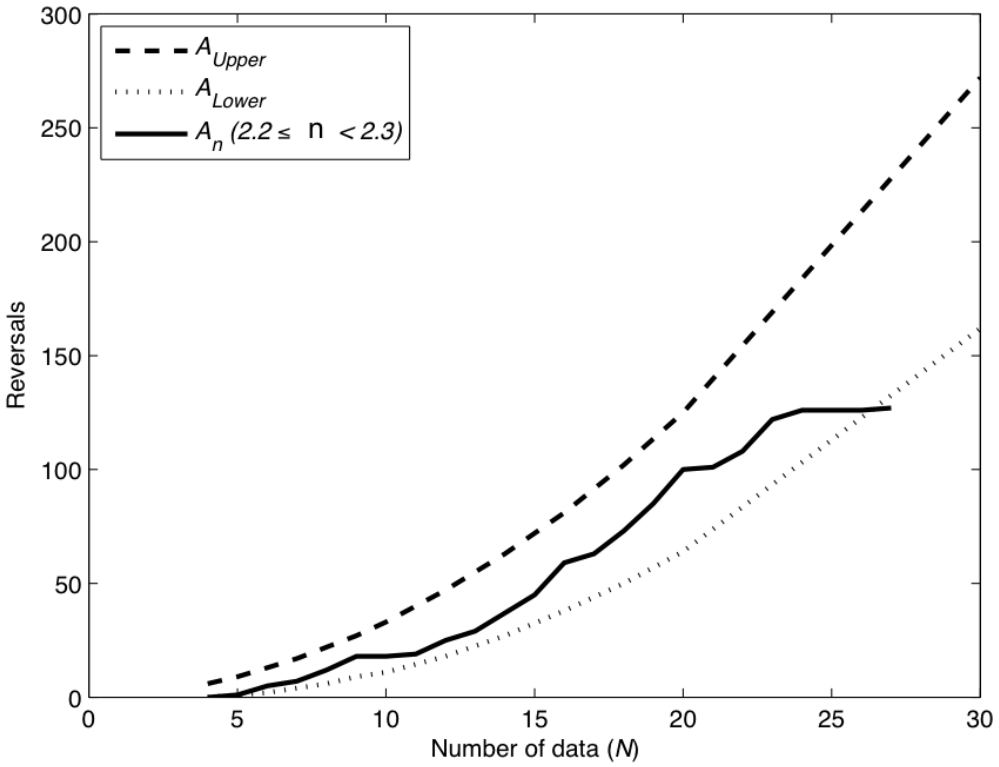

FIGURE 3.5: A comparison of the results from the reverse arrangement test for the absence of a trend versus the acceptance range for $z = 1.96$ which corresponds to a 95% confidence level. The test represents electron fluxes measured in the energy range $1.8 - 3.5$ MeV and solar wind density measured in the range $2.2 \leq n < 2.3$ cm^{-3}. In this case, the final value of A_n that falls within the acceptance range is $A_n = 126$ which corresponds to the final 26 data points. A reverse arrangement test for the final 27 data points returns $A_n = 127$ which falls outside the acceptance range.

acceptance range confirming that there is a trend. Hence, the saturation velocity is estimated to be at the 40^{th} highest V_{SW} data point which corresponds to solar wind velocity of 586 kms^{-1} as indicated in Figure 3.6. Here a 95% confidence level is preferred solely because lower confidence levels would provide less accurate estimations and higher confidence levels would make the reverse arrangement test less tolerant to small expected variations in the data.

The above method was applied to different solar wind densities in the range $2 -$ 6cm^{-3} in order to estimate the saturation velocities. The results are presented in

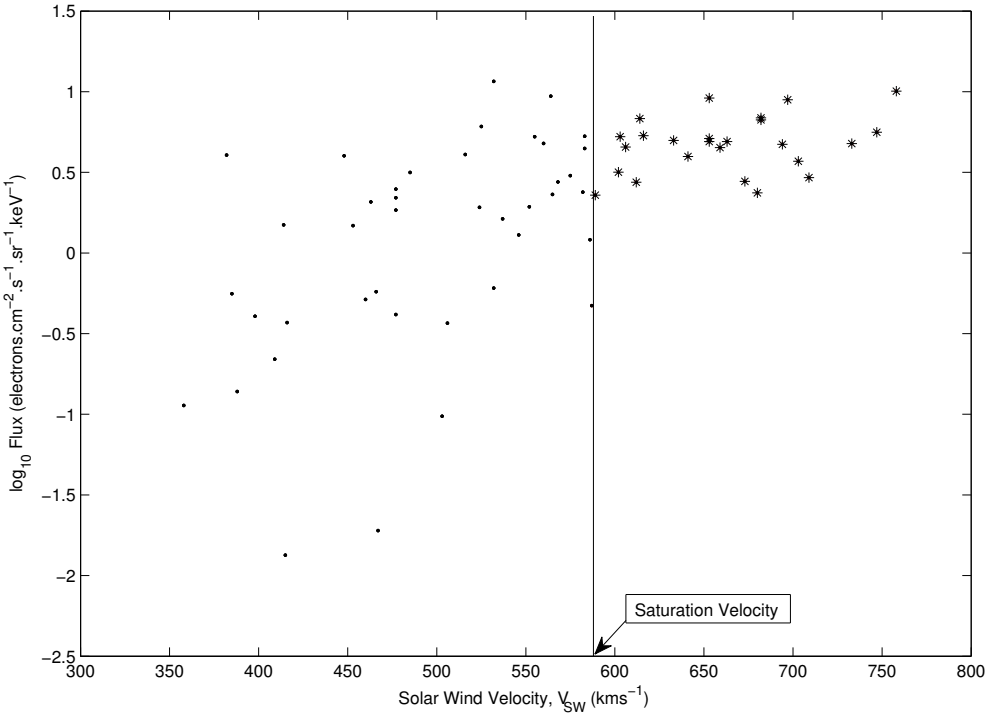

FIGURE 3.6: A scatterplot of energetic electron fluxes as a function of solar wind velocity for electron fluxes measured in the energy range $1.8 - 3.5$ MeV and solar wind density measured in the range $2.2 \leq n < 2.3$ cm^{-3}. There is a trend in the data points represented by solid dots below the saturation velocity but there is no trend present in the data points represented by stars above the saturation velocity with 95% confidence level.

Figure 3.7 in the form of a scatterplot of saturation velocity as a function of solar wind density. It clearly illustrates that the saturation velocity decreases as the solar wind density increases. Generally, Figure 3.7 follow a strong linear fit with a linear correlation coefficient of -0.77. However, for solar wind density in the range $1.3 \leq n < 1.6$ the saturation velocity appears to be curiously lower than expected as indicated by the circle in Figure 3.7. This anomaly may be due to the relatively larger solar wind density range which is obscuring information leading to inaccurate interpretation of the results. The most appropriate solution to this problem would be to reduce the bin size. However, reducing the bin size leads to considerably fewer number of data points in each data subset which is likely to

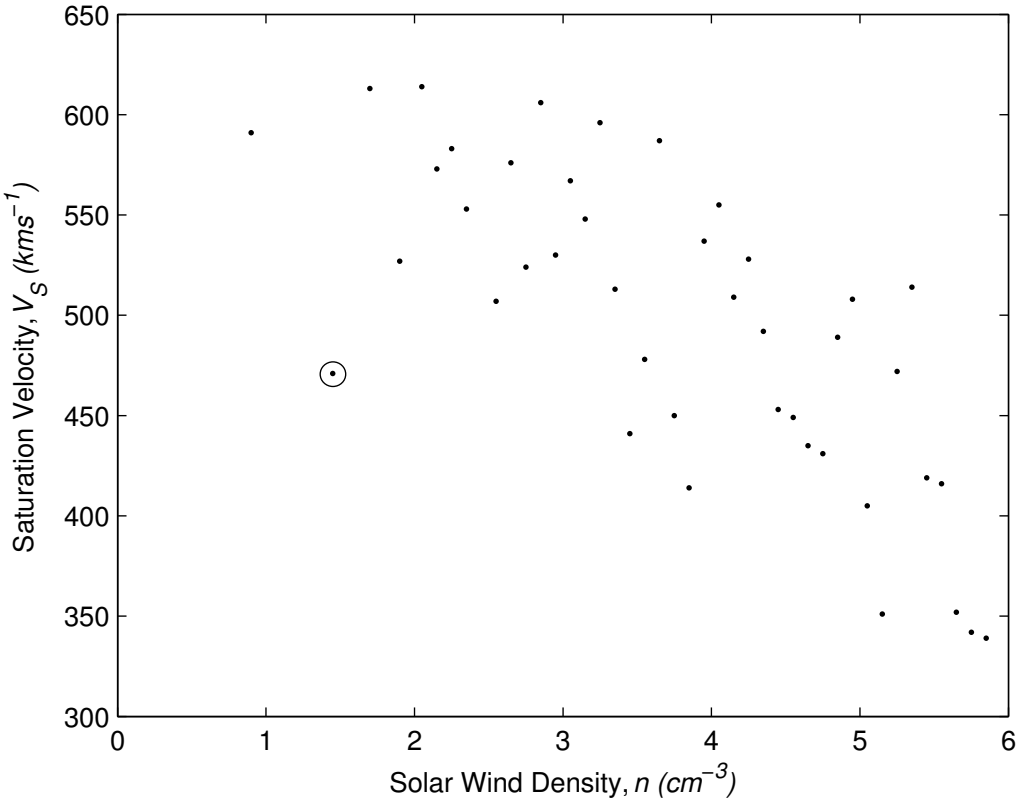

FIGURE 3.7: Saturation velocity as a function of solar wind density. Figure shows that as solar wind density increases the saturation velocity decreases. The circled data point represent possible anomaly.

produce unreliable results due to inaccurate representation of data (Figure 3.4).

3.4 Conclusion

From the results obtained in this study, it can be concluded that solar wind density plays an important role in defining the relationship between energetic electron flux and solar wind velocity at geostationary orbit. Clearly the electron flux have a distinct velocity dependent lower limit separated from the velocity independent upper limit by some saturation velocity. The reverse arrangement test is employed to estimate the saturation velocity with 95% accuracy. The results in Figure 3.7

demonstrates that it is the solar wind density that determines the saturation velocity. The saturation velocity decreases as the solar wind density increases. This implies that the range of solar wind velocity that is correlated to the electron flux decreases as solar wind density increases. For low solar wind densities the roughly linear correlation between electron flux and solar wind density is spread over a wide range of solar wind velocities, whereas for high solar wind densities the correlation between electron flux and solar wind density is limited to narrow range of solar wind velocities.

Low densities occur as a result of substantial electron loss from the outer radiation belt through wave particle interactions and drift loss through the dayside magnetopause due to both outward diffusion and magnetopause shadowing [159]. The latter is where the electron path takes electrons outside the magnetosphere given that the magnetopause is significantly compressed on the dayside due to high solar wind dynamic pressure [181]. This knowledge of the saturation velocity and its dependency upon solar wind density will not only provide better understanding of the physical processes within the geostationary orbit but also lead to improved modelling and forecasting of fluxes of high energy electrons in the outer terrestrial radiation belt. This can potentially help mitigate the damage to the satellites and other space based systems.

It is worth noting that there are limitations associated with the reverse arrangement test i.e. sensitivity to data gap and data size. Therefore, the reverse arrangement test must be employed with caution when analysing data associated with gaps. This introduces difficulties given that the occurrence rate of energetic electron fluxes vary across the solar wind density range and data gaps are difficult to eliminate.

Finally, this study was based only on one day averages of electron fluxes measured in the energy range $1.8 - 3.5$ MeV and solar wind densities less than 6.0 cm^{-3}. The relationship between solar wind saturation velocity and solar wind density may be different with shorter or longer time scales. Also, determination of the relationship between the saturation velocity and solar wind density for electron fluxes measured in other energy ranges and for solar wind densities larger than 6 cm^{-3} is highly beneficial for modelling and forecasting of fluxes of high energy electrons. This will be at the centre of future investigations into energetic electron fluxes at geostationary orbit.

3.5 Summary

A correlation between solar wind velocity and energetic electron fluxes at geostationary orbit was first identified more than thirty years ago. However, *Reeves et al.* [194] reported that the relation between solar wind velocity and energetic electron fluxes was considerably more complex than previously suggested. Application of process identification technique to the evolution of electron fluxes in the energy range of $1.8-3.5$MeV also revealed peculiarities in the relation between solar wind velocity and energetic electron fluxes at geostationary orbit. It has been revealed that for constant solar wind density, electron flux increases with solar wind velocity until a saturation velocity is reached [194] . Beyond the saturation velocity an increase in solar wind velocity is statistically not accompanied with electron flux enhancement. This study investigated the saturation velocity and its dependency upon solar wind density using the reverse arrangement test. Approximately 20 years of electron flux data collected by Los Alamos National Laboratory using the

Energetic Spectrometer for Particles (ESP) instrument was studies. The results proves that solar wind density play a crucial role in defining the relationship between solar wind velocity and electron flux at geostationary orbit. This important new knowledge can be used in forecasting and nowcasting models of energetic electron fluxes at geostationary orbit in order to improve predictions and ultimately help mitigate the damage caused to electronic components of geostationary satellites. The results have been published in the peer-reviewed international Journal of Geophysical Research in February 2013 (*Aryan, H., Boynton R. J., and Walker S. N. (2013), Analysis of trends between solar wind velocity and energetic electron fluxes at geostationary orbit using the reverse arrangement test, J. Geophys. Res. Space Phys., 118, doi:10.1029/2012JA018216*).

3.6 Acknowledgments

This work was performed using data from Los Alamos National Laboratory that was provided as auxiliary material to the paper by *Reeves et al.* [194] at ftp:/ftp.agu.org/apend/ja/ 2010ja015735, and the OMNI web data.

Chapter 4

Wave-Particle Interaction

4.1 Introduction

Plasma waves are electromagnetic fluctuations that are found in the Earths magnetosphere. Waves play a fundamental role in the dynamics of magnetospheric particles.They affect the energisation, pitch angle distribution, and collision frequency of particles. Magnetospheric emissions may originate from various sources including plasma instabilities, turbulent magnetosheath, lightning discharges in the atmosphere, and man-made signals. The most common plasma waves in the magnetosphere are magnetosonic, Electromagnetic Ion Cyclotron (EMIC), chorus, and plasmaspheric hiss waves. These waves are distributed in the inner magnetosphere and are observed under different frequency bands.

Seed (tens to hundreds of keV) electrons, which form an important source of energetic electrons in the radiation belts, are produced when energetic plasma sheet electrons are transported into the geostationary orbit during substorms and periods of enhanced convection [148]. Local acceleration by wave particle interactions

[102, 229, 239] through efficient energy diffusion [100, 229] can further energise the seed electrons to highly relativistic energies [16, 101, 236]. The interaction of gyroresonant particles with chorus waves largely determines the dynamics of the radiation belts [166, 260, 261] that affects the acceleration and loss of radiation belt electrons [24, 37, 220]. Chorus is also the dominant scattering process leading to diffuse auroral precipitation [177, 178, 236].

Chorus emissions are very intense right hand polarised electromagnetic whistler mode waves that are excited naturally in the low density region near the geomagnetic equator outside the plasmapause [46, 136, 207]. They are observed as short coherent pulses in two separate frequency bands: the lower band ($0.1f_{ce} < f < 0.5f_{ce}$) and the upper band ($0.5f_{ce} < f < f_{ce}$) with a gap in wave power at $0.5f_{ce}$ [46, 96, 243], where f_{ce}, electron cyclotron frequency, is the frequency with which electrons gyrate about the Earths magnetic field line and is proportional to the magnetic field intensity. Cyclotron resonance with anisotropic energetic electrons injected from the plasma sheet is thought to be responsible for the excitation of chorus waves [126, 164, 183] that will subsequently propagate from equatorial regions to higher latitudes in both the southern and the northern hemispheres [37, 136, 206].

In addition, evidence points to whistler mode chorus as the main source of plasmaspheric hiss [39, 170], which is not only responsible for the formation of the slot region [1, 156, 157], but also responsible for the decay of energetic electrons in the outer radiation belt during relatively quiet times [232] due to resonant pitch angle scattering of energetic electrons [157]. According to a detailed ray tracing by Bortnik et, al. [38], a fraction of chorus energy can avoid Landau damping and propagate from an equatorial source region ($4 < L < 7$) outside the plasmasphere

to high latitudes, and subsequently refract into the plasmasphere, where it blends into the incoherent band of plasmaspheric hiss.

Plasmaspheric hiss is a structureless, band limited, right hand polarised electromagnetic whistler mode wave that was first discovered in the late 1960s [94, 234]. It is an important class of electromagnetic wave [38, 39, 237], which is exited naturally in the high plasma density region inside the plasmasphere and dayside plasmaspheric plumes [50, 95, 187]. Plasmaspheric hiss is observed as a steady, incoherent noise band in the frequency range of 100 Hz $< f <$ 2 kHz with a lower power than chorus [168]. The amplitudes of plasmaspheric hiss can typically range from 10s of pT on the dayside during quiet times to above 100 pT during active times [142, 168, 238]. Figure 4.1 shows the time-frequency spectrogram of wave magnetic field spectral density of chorus waves observed by Van Allen Probe-B between 17:08:40 - 17:08:46 UT on 30 September 2012 and less than quarter of an hour later (b) Van Allen Probe-A observes plasmaspheric hiss between 17:22:21 - 17:22:27 UT. The white dashed line marks the 0.5 f_{ce} frequency. The figure illustrates the difference in structure, observed frequency, and appearance of plasmaspheric hiss and chorus waves.

Naturally occurring electromagnetic waves, such as plasmaspheric hiss and chorus waves, have attracted significant attention in recent decades for their crucial role in the acceleration and loss of energetic electrons that ultimately change the dynamics of the radiation belts [139, 141, 143, 167, 169, 236, 240]. The distribution of these waves in the inner magnetosphere is commonly presented under different values of geomagnetic activity as expressed by the geomagnetic indices, such as Ae, Kp, and Dst [4, 139, 141, 168, 169]. The results largely show that both plasmaspheric hiss

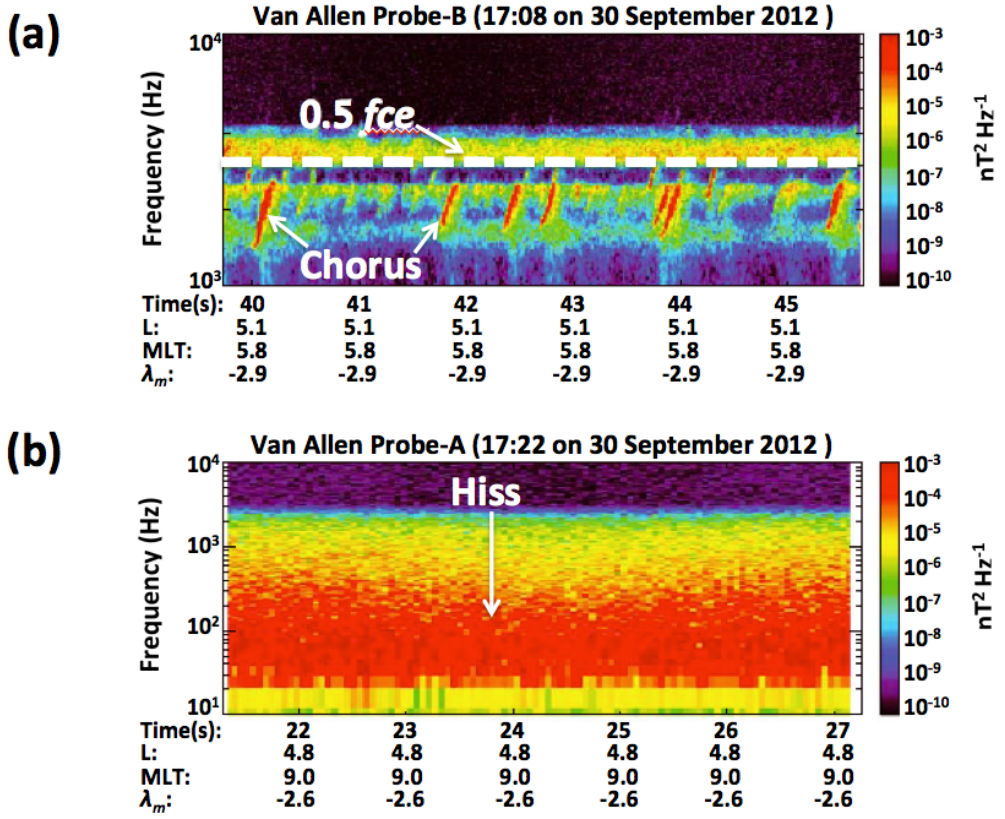

FIGURE 4.1: The time-frequency spectrogram of wave magnetic field spectral density of (a) chorus waves observed by Van Allen Probe-B between 17:08:40 - 17:08:46 UT on 30 September 2012 and less than quarter of an hour later (b) Van Allen Probe-A observes plasmaspheric hiss between 17:22:21 - 17:22:27 UT, courtesy of Li et, al. [142]. The white dashed line marks the 0.5 f_{ce} frequency. The figure illustrates the difference in structure, observed frequency, and appearance of plasmaspheric hiss and chorus waves.

and chorus emissions are dependent on geomagnetic activity with peak intensities observed during active conditions.

In the case of chorus waves, *Li et al.* [139] performed a comprehensive survey of chorus waves using approximately 2 years (1 June 2007 to 1 Feb 2009) of THEMIS (Time History of Events and Macroscale Interactions during Substorms) data to show that the largest wave intensities were observed with equatorial ($|\lambda_m| < 10°$, where λ_m is the magnetic latitude) chorus between pre-midnight to around noon Magnetic Local Time (MLT) and during active conditions ($Ae > 300$ nT) in the

region $L > 7$. These results were later confirmed by *Meredith et al.* [169] who combined data from five different satellites to improve the statistical survey of chorus waves in the inner magnetosphere. Earlier in 2004, Meredith et, al. [168] studied the substorm dependance of plasmaspheric hiss and found that the largest average wave intensities, in the order of 47 pT, were observed with midlatitude ($|\lambda_m| > 15°$) hiss from 0800 to 1800 MLT during active conditions ($Ae > 500$ nT) in the region $2 < L < 4$.

The wave models discussed above, similar to many other wave models (e.g., [141, 165, 167, 236]), were all organised only by geomagnetic indices. However, not all geomagnetic storms necessarily change the flux of relativistic electrons in the outer radiation belt as it was shown by *Reeves et al.* [193] in 2003. The latter study, examined 276 geomagnetic storms of which only 53% increased, 19% decreased, and the remaining 28% left the flux of relativistic electrons in the outer radiation belt relatively unchanged.

Additionally, geomagnetic indices are compiled from imperfectly covered ground based measurements. Although, geomagnetic indices are principally continuous and homogeneous over long time periods, they are indirect and nonspecific parameters [18, 247] that lack time history information. For example, the Ae index is compiled from the magnetograms of several auroral zone observatories to represent auroral electrojet properties [59]. Despite its universal use in wave models, the Ae index may not always be able to monitor the electrojet activity precisely [5, 154] due to the highly variable auroral ovals [98, 123, 153]. Meanwhile, the planetary Kp index is derived from the sub-auroral K index measurements obtained from various midlatitude ground based magnetometer stations [163] to describe the geomagnetic disturbance. However, the sub-auroral stations are largely sensitive to

convection due to the effects of the inner edge of the plasma sheet [235], which may introduce ambiguities in its interpretations [257]. Finally, the Dst index is developed from low latitude horizontal component magnetograms in an effort to determine the ring current strengths [226, 247]. Although the ring current is the most significant contributing current system in Dst index [92, 116, 196], it is possible that other low latitude current systems, such as substorms induced currents, magnetotail currents, and induced currents in the solid Earth may also contribute to Dst index [197, 247].

In general, geomagnetic indices indicate the solar wind changes that ultimately drive energetic electron enhancements [18]. This emphasises the need to present wave distributions not only as a function of geomagnetic activity, but also as a function of directly measured solar wind parameters, such as velocity (V), density (n), pressure (P), and Bs (where $Bs = -Bz$ and Bz is the southward interplanetary magnetic field component), that are known to be predominantly effective in the control of radiation belt energetic electron fluxes [184, 194, 195, 251].

Recently, *Boynton et al.* [44] applied the NARMAX algorithm [27, 28] to show the importance of solar wind parameters that control the flux of energetic electrons at geostationary orbit and identified solar wind velocity and the southward interplanetary magnetic field component as the most influential parameters. Solar wind density and pressure are also important geoeffective parameters [9, 145, 155].

4.2 Statistical Study of Chorus Wave Distributions in the Inner Magnetosphere as Functions of Geomagnetic Activity and Solar Wind Parameters

In the present study the set of parameters of the wave distributions are expanded to include solar wind parameters, such as bulk velocity, density, flow pressure, and the vertical interplanetary magnetic field component (Bz), in addition to geomagnetic activity. The inclusion of solar wind parameters will broaden the set of parameters used to represent wave distributions in the inner magnetosphere, which will undoubtably improve our understanding of the dynamics of the radiation belt electrons, and also link the distribution of waves to specific and directly measured solar wind parameters. Studies of the evolution of energetic electron fluxes rely heavily on the numerical codes in order to model energy and pitch angle diffusion due to electron interaction with plasma waves in the frame of quasi-linear approximation. Therefore, including the solar wind parameters in addition to the geomagnetic activity in the statistical wave models will benefit those studies, provide a better representation of the wave distributions in the inner magnetosphere, and improve our knowledge of the acceleration and loss of radiation belt electrons.

This study analyses almost 4 years (1 January 2004 to 29 September 2007) of Double Star TC1 Spatio-Temporal Analysis of Field Fluctuation (STAFF) and OMNIWeb data in order to present the wave magnetic field intensities for the lower and upper band chorus waves as functions of Magnetic Local Time (MLT), magnetic latitude (λ_m), L, geomagnetic index (Ae), and solar wind parameters

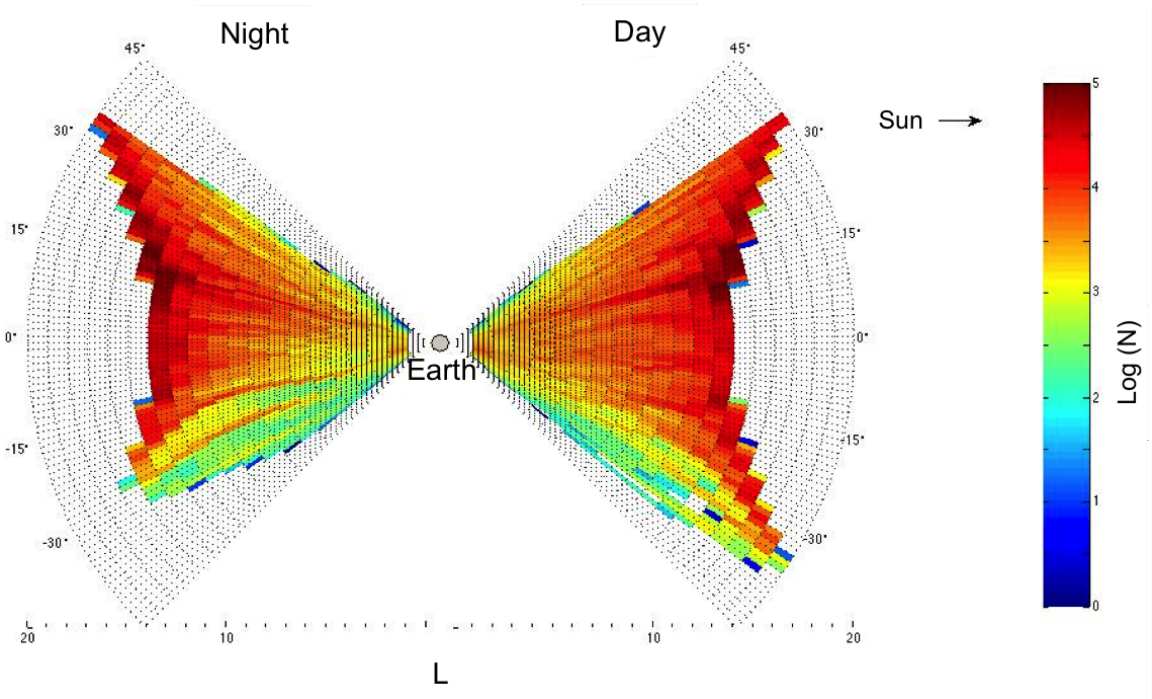

FIGURE 4.2: The nightside (left) and dayside (right) coverage of the Double Star TC1 as functions of L and λ_m.

(Velocity (V), Density (n), Pressure (P), and the vertical interplanetary magnetic field component (Bz)).

4.2.1 Description of the Data Set and Methodology

Double Star was lunched on 29 December 2003 as a joint mission by the European Space Agency (ESA) and China National Space Administration. The equatorial satellite Tan Ce 1 (TC1) operates in an highly elliptical orbit with a perigee of 562 km and an apogee 78,970 km, allowing the equatorial TC1 satellite to access all of the most critical regions of the radiation belts. Figure 4.2 present the nightside and dayside coverage of the double star TC1 as functions of L and λ_m.

The STAFF experiment on board TC1 computes the spectral matrix at 27 different frequencies (between 10 Hz and 4 kHz) with a 1s resolution using a Digital Wave

Processor (DWP) [56] provided by The University of Sheffield. At these frequencies, where the available telemetry does not permit acquisition of the waveform, spectrum analysis is performed onboard. After the data pass through an antialias filter, DWP digitises the three components of the waveform at a 10 kHz sampling rate. A complex Fast Fourier Transform (FFT) is then calculated and processed to get a spectral matrix in 27 roughly logarithmically spaced channels (similar to that of Cluster). The spectrum analyser data is then processed on the ground to minimise the interference resulting from the non-deployment of the antenna boom. This is done by rejecting spectra acquired when large interference spikes occur, and by combining the signals from two axes of the antenna to synthesise a measurement in a direction where continuous interference is least. The optimum direction is adjusted as a function of frequency and spin phase. This study analyses almost four years (01, January, 2004 to 29, September, 2007) of Double Star TC1 STAFF and OMNIWeb data. The geomagnetic index (Ae) and the solar wind parameters (V, n, and P) used are 1−hour values available online at OMNIWeb database. The vertical interplanetary magnetic field component (Bz) used are 1−minute values that are also available online at OMNIWeb database. The L parameter is binned in linear steps of $0.2L$ and the MLT parameter is binned in linear steps of 1-hour of MLT. The lower and upper band chorus wave intensities are calculated over the frequency ranges ($0.1fce < f < 0.5fce$) and ($0.5fce < f < fce$) respectively. The data is only selected in the cases where all of a given frequency band fall within the frequency range otherwise the data is rejected. All data are in SI unites (Ae (nT), V (km/s), n (n/cc), P (nPa), Bz (nT)).

4.2.2 Results

4.2.2.1 Average Chorus Intensities as a Function of Geomagnetic Activity

The distributions of chorus wave in the inner magnetosphere can be presented under different values of geomagnetic activity as expressed by the geomagnetic indices. Figure 4.3 shows the equatorial ($|\lambda_m| < 15°$) lower band (a), equatorial upper band (b), midlatitude ($15° \leq |\lambda_m| \leq 40°$) lower band (c) and midlatitude upper band (d) average chorus intensities as functions of L, MLT, and geomagnetic activity (as expressed by Ae) during quiet (left), moderate (centre) and active (right) conditions. In each sub-figure the MLT increases anti-clockwise with midday located at the north and the L value increases outwards up to $L = 10$.

It is clear from Figure 4.3 that both the equatorial (Figure 4.3b) and midlatitude (Figure 4.3d) upper band chorus intensities are relatively weak even during active conditions with peak values largely below 10 pT. The peak chorus intensities are mostly confined in the regions from 0500 to 1300 MLT (equatorial) and from 0900 to 1400 MLT (midlatitude), and marginally intensify with increasing geomagnetic activity.

The lower band chorus intensities (Figures 4.3a and 4.3c) on the other hand, are far more extensive and stronger than the corresponding upper band chorus. The peak lower band chorus intensities rise to 10 pT and 20 pT, primarily from pre-midnight to the afternoon sector, during quiet and moderate conditions, respectively. The largest intensities of the order 50 pT are observed for lower band chorus during active conditions in the region of $4 \leq L \leq 9$ from 2300 to 1300 MLT (equatorial) and from 0500 to 1400 MLT (midlatitude).

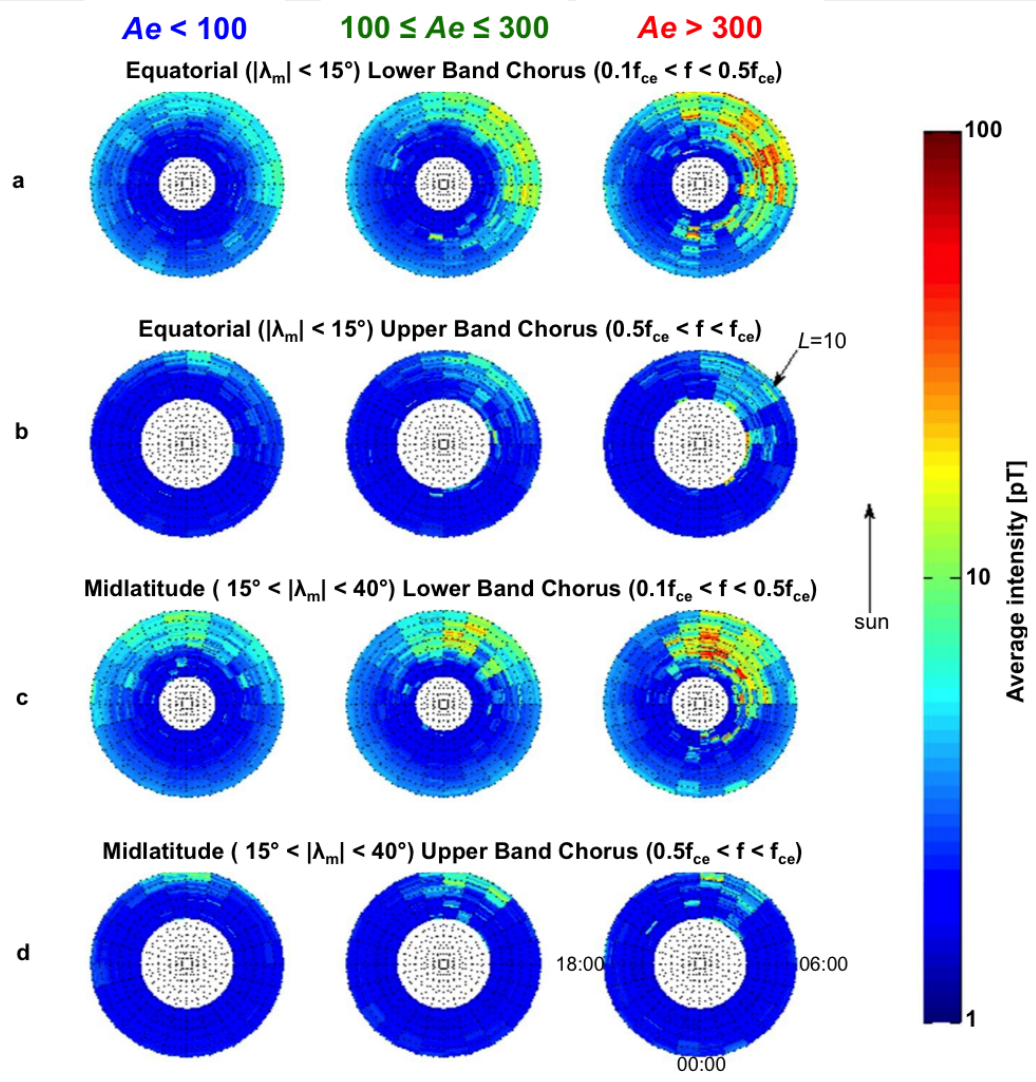

FIGURE 4.3: The (a) equatorial ($|\lambda_m| < 15°$) lower band, (b) equatorial upper band, (c) midlatitude ($15° \leq |\lambda_m| \leq 40°$) lower band, and (d) midlatitude upper band average chorus intensities as functions of L, MLT, and geomagnetic activity during quiet (left column), moderate (middle column), and active (right column) conditions. In each sub-figure the MLT increases anti-clockwise with midday located at the north and the L value increases outwards up to $L = 10$.

By large, the peak intensities of the midlatitude chorus are similar in magnitude to the corresponding equatorial chorus intensities. However, the peak intensities for midlatitude region predominantly occur within a smaller MLT sector than the corresponding equatorial chorus intensities. For example, the peak intensities of midlatitude lower band chorus during active conditions mainly occur from 0500 to 1400 MLT compared to a more extensive spread from 2300 to 1300 MLT seen for equatorial lower band chorus.

The results here are largely consistent with previous studies that presented model wave distributions in the inner magnetosphere under different values of geomagnetic activity as expressed by the geomagnetic indices [3, 4, 141, 167, 169]. In particular, the results here agree with the results of *Meredith et al.* [169] who presented a combined satellite (DE1 (3 years), CRRES (15 months), Cluster 1 (10 years), Double Star TC1 (1 year), and THEMIS (17 months)) model of the equatorial and midlatitude wave intensity for the upper and lower band chorus also as a function of *Ae*.

4.2.2.2 Average Chorus Intensities as a Function of Solar Wind Parameters

As discussed earlier, *Reeves et al.* [193] concluded that only 53% of geomagnetic storms increase the flux of relativistic electrons at geostationary orbit while 19% cause a decrease and the remaining 28 have no significant effect. Also, geomagnetic indices are compiled from imperfectly covered ground based measurements. Although, geomagnetic indices are principally continuous and homogeneous over long time periods, they are indirect and nonspecific parameters [18, 247] that lack time history information. This emphasises the importance of including solar wind

parameters in addition to geomagnetic indices in order to better understand the distributions of chorus wave in the magnetosphere. The following sections reveal the average chorus intensities as a function of solar wind velocity, density, pressure and interplanetary magnetic field, Bz, respectively.

Average Chorus Intensities as a Function of Velocity

Solar wind parameters are known to be predominately effective in the control of high energy fluxes at geostationary orbit with solar wind velocity considered as the most influential parameter [44]. Figure 4.4 shows the average lower band chorus intensities as functions of L, MLT and V for slow (left column), moderate (middle column), and fast (right column) solar wind velocities.

It is commonly accepted that temporal changes in solar wind parameters are not immediately observed at the geostationary orbit. In fact, there is a time delay of approximately 1 – 2 days depending on the energy [9, 42, 147, 189, 194]. The interplay between the local acceleration and outward/inward radial diffusion mainly determines the time delay. While chorus emissions are generated over a wider range than geostationary orbit, a similar time delay may still apply. Consequently, Figure 4.4 includes maximum solar wind velocity from current day (V_{0m}, top row), 1 day (V_{1m}, middle row), and 2 days (V_{2m}, bottom row) ago (the subscript, $*m$, represents maximum value, and the corresponding number indicates number of days delay).

The average chorus intensities as a function of solar wind velocity follows a noticeably similar trend to that of chorus intensities as a function of geomagnetic activity. In this case, the average chorus intensities rise with increasing solar wind velocity in all three cases of delay. However, it is not immediately clear which

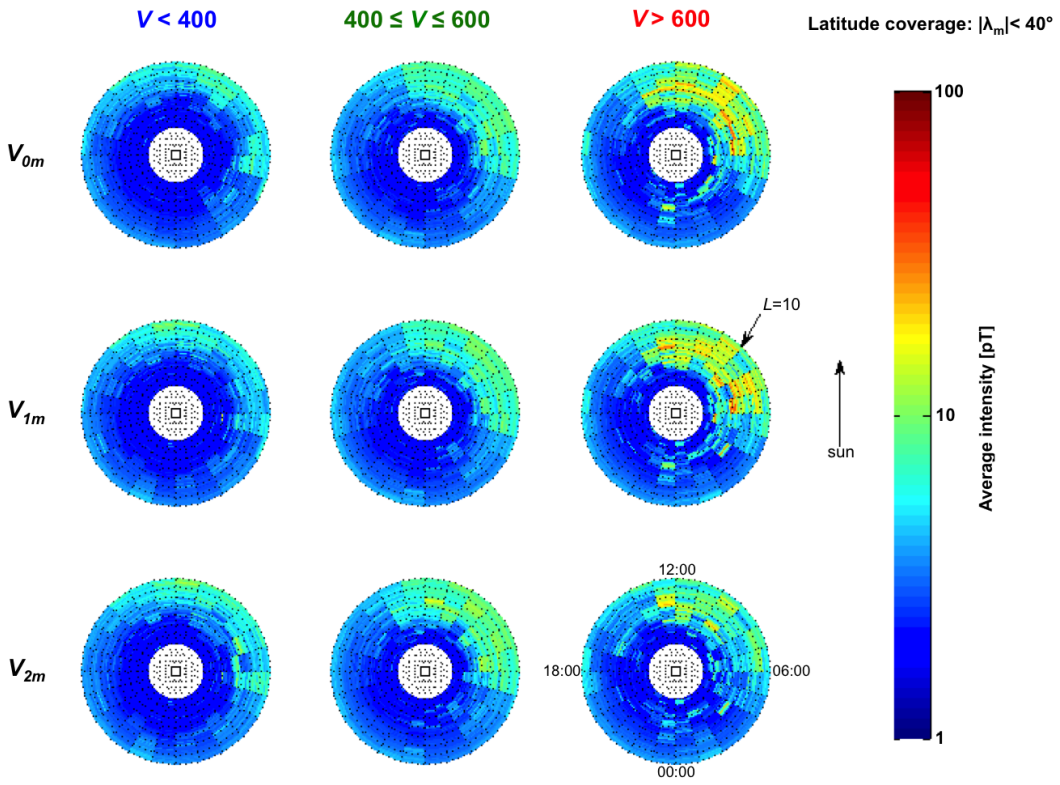

FIGURE 4.4: Average chorus intensities as a function of L, MLT, and V for (left column) slow, (middle column) moderate, and (right column) fast solar wind velocities. Results are shown for maximum solar wind velocity observed on (top row) current day (V_{0m}), (middle row) previous day (V_{1m}), and (bottom row) 2 days ago (V_{2m}). The magnetic latitude coverage is $|\lambda_m| < 40°$.

of the three cases of delay provides the most widespread statistical distribution. Therefore, the Kullback-Leibler [132, 133] theory was applied in order to identify the case with the most widespread statistical distribution.

The Kullback-Leibler theory calculates the difference between two probability distributions (e.g., X and Y) given as a number known as the Kullback-Leibler Distance (D_{KL}) which is essentially the distance of X from Y, with X and Y normalised, defined by equation 5.7.

TABLE 4.1: The Kullback-Leibler Distance (D_{KL}) between slow and moderate (D_{KLsm}), slow and fast (D_{KLsf}), and moderate and fast (D_{KLmf}) solar wind velocities for V_{0m}, V_{1m} and V_{2m} as presented in Figure 4.4. All three cases of delay provide valid distributions, yet the most widespread statistical distribution is observed with maximum solar wind velocity from previous day (V_{1m}) that has the largest D_{KLsf} value of 0.0635.

	D_{KLsm}	D_{KLmf}	D_{KLsf}
V_{0m}	0.0270	0.0395	0.0534
V_{1m}	0.0258	0.0513	0.0635
V_{2m}	0.0298	0.0448	0.0458

$$\mathbf{D_{KL}} = \sum_i X_i \cdot log_2(X_i/Y_i) \tag{4.1}$$

A D_{KL} value of zero implies that the two probability distributions are identical. The Kullback-Leibler theory was applied to the results in Figure 4.4 in the following way: 1) calculate D_{KL} between slow and moderate (D_{KLsm}), slow and fast (D_{KLsf}), and moderate and fast (D_{KLmf}) solar wind velocities for each particular cases of delay. 2) verify the validity of the distribution for each cases of delay (a distribution is only valid if $D_{KLsf} > D_{KLsm}$ and $D_{KLsf} > D_{KLmf}$, i.e., the largest difference is expected between the two extreme distributions; in this case between slow and fast solar wind velocities). 3) the distribution with the highest value of D_{KLsf} amongst the valid distributions is selected (larger values of D_{KL} suggests broader distribution). The values of D_{KLsm}, D_{KLsf}, D_{KLmf} for V_{0m}, V_{1m} and V_{2m} are presented in Table 4.1.

The results show that all three cases of delay provide valid distributions. However, the most widespread statistical distribution is observed with maximum solar wind velocity from previous day (V_{1m}) that has the largest D_{KLsf} value of 0.0635. Hence,

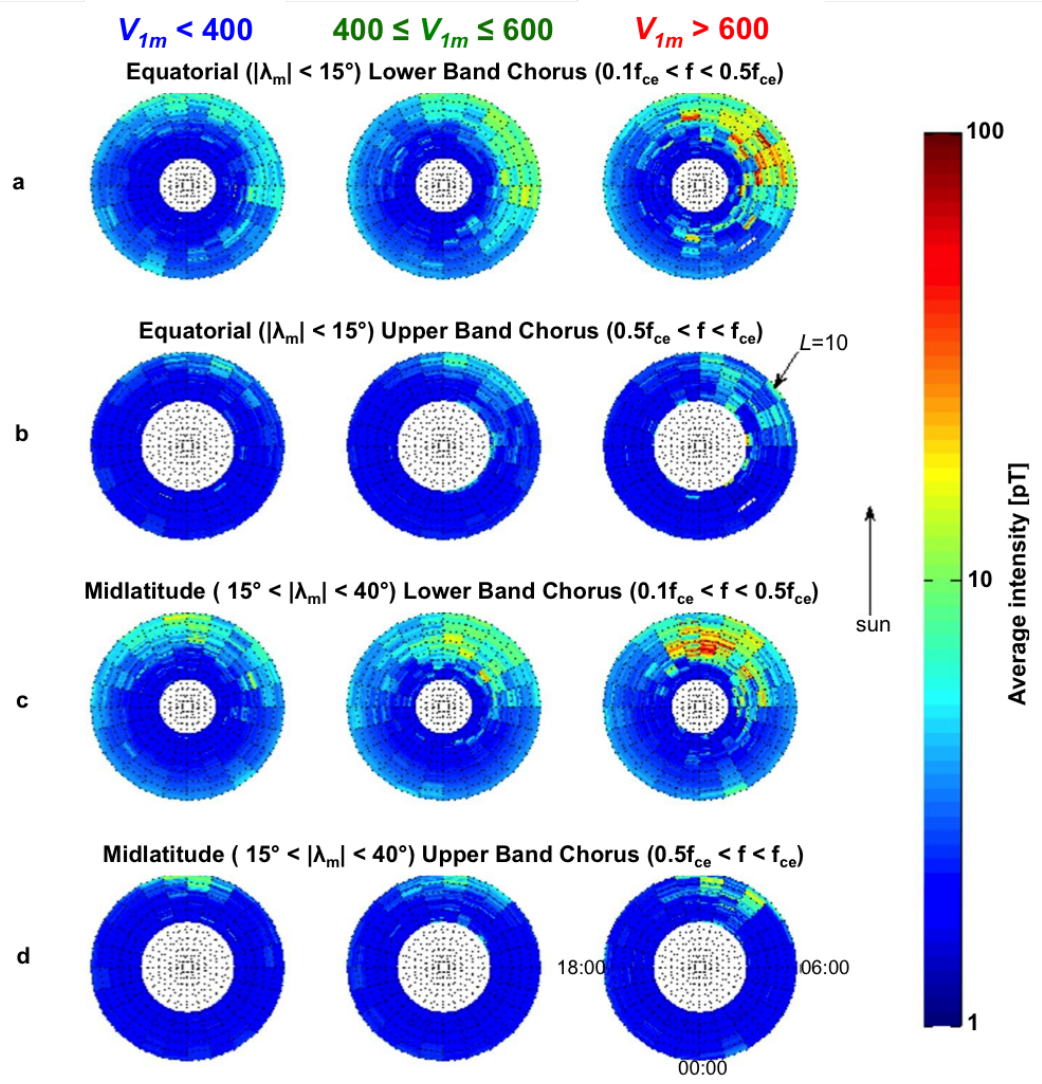

FIGURE 4.5: The (a) equatorial ($|\lambda_m| < 15°$) lower band, (b) equatorial upper band, (c) midlatitude ($15° \leq |\lambda_m| \leq 40°$) lower band, and (d) midlatitude upper band average chorus intensities as functions of L, MLT, and maximum solar wind velocity from previous day (V_{1m}) for slow (left column), moderate (middle column), and fast (right column) solar wind velocities.

a time delay of one day is selected as the most appropriate time delay for solar wind velocity.

Figure 4.5 shows the equatorial ($|\lambda_m| < 15°$) lower band (a), equatorial upper band (b), midlatitude ($15° \leq |\lambda_m| \leq 40°$) lower band (c) and midlatitude upper

band (d) average chorus intensities as functions of L, MLT, and maximum solar wind velocity from previous day (V_{1m}) for slow (left column), moderate (middle column), and fast (right column) solar wind velocities. The results show significant similarities to the corresponding average equatorial and midlatitude lower and upper band chorus intensities as a function of geomagnetic activity seen in Figure 4.3.

The upper band chorus intensities are generally weak with peak values of less than 10 pT even during active conditions. The peak intensities largely occur within the regions of 0600 to 1200 MLT (equatorial) and 1000 to 1400 MLT (midlatitude) and rise slightly with increasing velocity. The lower band chorus is more extensive, occurring in the region $4 \leq L \leq 9$ from 0300 to 1300 MLT (equatorial) and from 0300 to 1300 MLT (midlatitude), and stronger in compression to the corresponding upper band chorus with peak intensities rising to 15 pT, 20 pT, and 50 pT during slow, moderate, and fast solar wind velocities, respectively. The occurrence of peak lower band chorus intensities during active conditions (Figure 4.3) is slightly higher than during fast solar wind velocities (Figure 4.5). The peak intensities of midlatitude chorus are approximately equal in magnitude to the corresponding equatorial chorus intensities but mainly occur at smaller MLT sector. The results prove that there is a strong dependency between the intensity of chorus emission and solar wind velocity.

Average Chorus Intensities as a Function of Density

Solar wind density is another important solar wind parameter that is known to be influential in the control of high energy fluxes at geostationary orbit where it plays a crucial role in defining the relationship between energetic electron fluxes and solar wind velocity [9]. Figure 4.6 shows the average chorus intensities as

TABLE 4.2: The Kullback-Leibler Distance (D_{KL}) between low and moderate (D_{KLlm}), low and high (D_{KLlh}), and moderate and high (D_{KLmh}) solar wind densities for n_{0m}, n_{1m} and n_{2m} as presented in Figure 4.6. Here, the distributions of n_{0m} (top row) and n_{1m} (middle row) are valid. However, the distribution of n_{2m} (bottom row) is invalid because $D_{KLlm} > D_{KLlh}$. Hence, the most widespread statistical distribution is observed with maximum solar wind density from previous day (n_{1m}) that has the largest D_{KLlh} value of 0.0500.

	D_{KLlm}	D_{KLmh}	D_{KLlh}
n_{0m}	0.0368	0.0307	0.0412
n_{1m}	0.0447	0.0305	0.0500
n_{2m}	0.0583	0.0293	0.0580

functions of L, MLT, and n for low (left column), moderate (middle column), and high (right column) solar wind densities. Once again, the time delay introduced by the magnetospheric system is considered, and therefore, the average lower band chorus is shown for maximum density from the current day (n_{0m}, top row), previous day (n_{1m}, middle row), and 2 days (n_{2m}, bottom row) ago.

In contrast to solar wind velocity (Figure 4.4), the average chorus intensities decline with increasing solar wind density. The Kullback-Leibler theory was applied to calculate D_{KL}, between low and moderate (D_{KLlm}), low and high (D_{KLlh}), and moderate and high (D_{KLmh}) solar wind densities for each particular cases of delay, shown in Table 4.2. Here, the distributions of n_{0m} (top row) and n_{1m} (middle row) are valid. However, the distribution of n_{2m} (bottom row) is invalid because $D_{KLlm} > D_{KLlh}$. Amongst, the two valid distributions the most widespread statistical distribution is observed with maximum solar wind density from previous day (n_{1m}) that has the largest D_{KLlh} value of 0.0500. Subsequently, a time delay of one day is selected as the most appropriate time delay for solar wind density.

Figure 4.7 shows the equatorial ($|\lambda_m| < 15°$) lower band (row a), equatorial upper band (row b), midlatitude ($15° \leq |\lambda_m| \leq 40°$) lower band (row c) and midlatitude

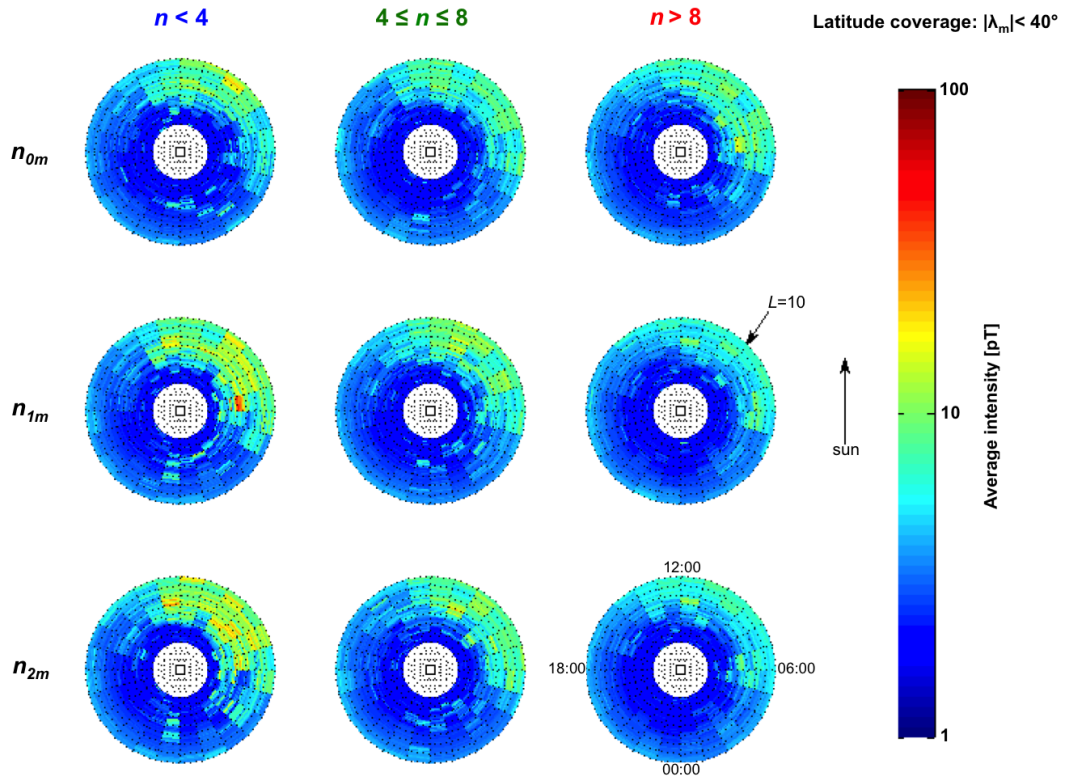

FIGURE 4.6: Average chorus intensities as functions of L, MLT, and n for (left column) low, (middle column) moderate, and (right column) high solar wind densities. Results are shown for maximum solar wind density observed on (top row) current day (n_{0m}), (middle row) previous day (n_{1m}), and (bottom row) 2 days ago (n_{2m}). The magnetic latitude coverage is $|\lambda_m| < 40°$.

upper band (row d) average chorus intensities as functions of L, MLT, and maximum solar wind density from previous day (n_{1m}) for low (left column), moderate (middle) and high (right column) solar wind densities. The upper band chorus intensities are expectedly weak with peak values of less than 10 pT. The peak intensities largely occur within the regions of 0600 to 1200 MLT (equatorial) and 1000 to 1400 MLT (midlatitude) and drop slightly with increasing density.

The lower band chorus is more extensive, occurring in the region $4 \leq L \leq 9$ from 0500 to 1100 MLT (equatorial) and from 0600 to 1400 MLT (midlatitude), and

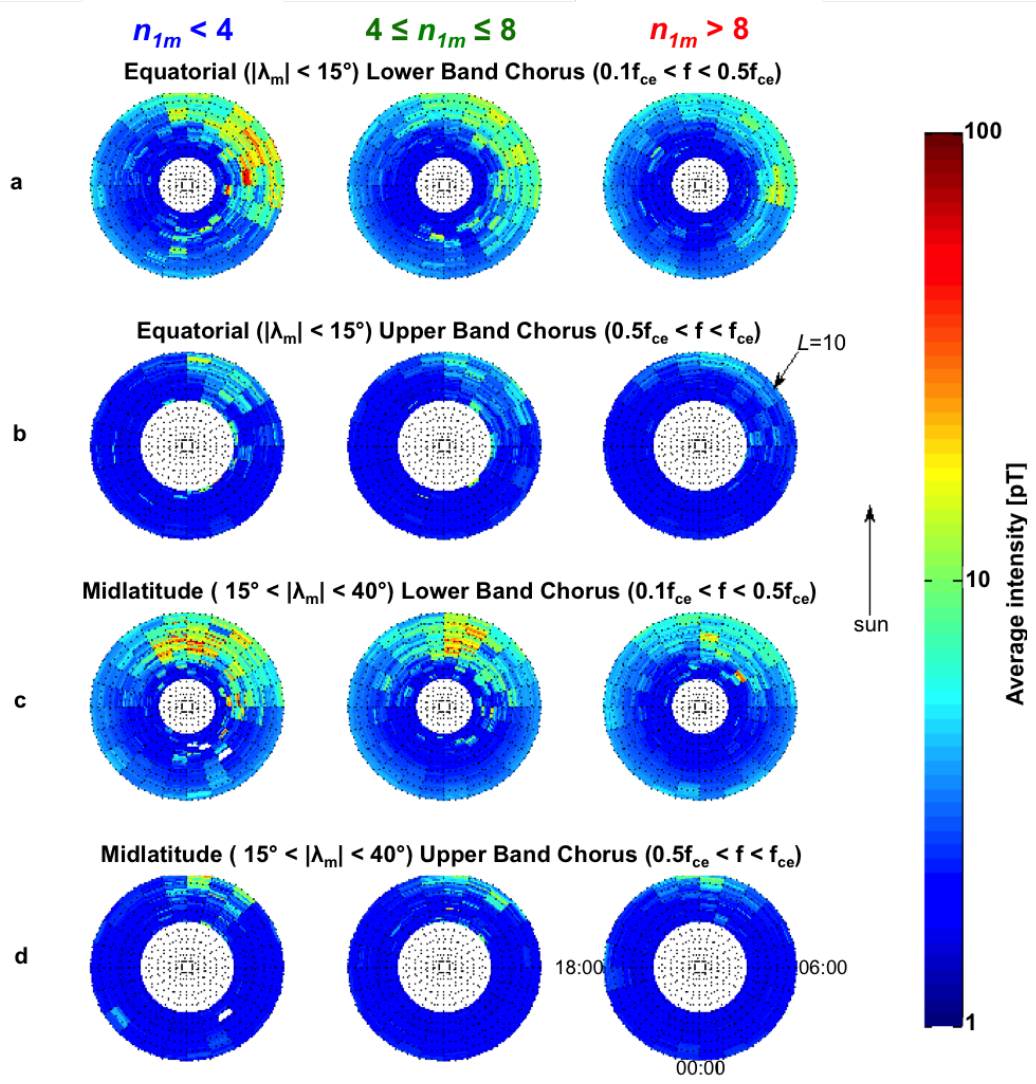

FIGURE 4.7: The (a) equatorial ($|\lambda_m| < 15°$) lower band, (b) equatorial upper band, (c) midlatitude ($15° \leq |\lambda_m| \leq 40°$) lower band, and (d) midlatitude upper band average chorus intensities as a function of L, MLT, and maximum solar wind density from previous day (n_{1m}) for low (left column), moderate (middle column), and high (right column) solar wind densities.

stronger in compression to the corresponding upper band chorus with peak intensities rising to 50 pT, 20 pT, and 15 pT during low, moderate, and high solar wind densities respectively. However, the occurrence of peak lower band chorus intensities during low solar wind densities (Figure 4.7) is lower than during active conditions (Figure 4.3) and during fast solar wind velocities (Figure 4.5). The peak intensities of midlatitude chorus are roughly equal in magnitude to the corresponding equatorial chorus intensities. In contrast, the peak intensities for midlatitude region predominantly occur within a smaller MLT sector than the corresponding equatorial chorus intensities, a similar trend to solar wind velocity and geomagnetic activity. Evidently, the results show convincing dependency between the intensity of chorus emission and solar wind density.

Average Chorus Intensities as a Function of Flow Pressure

Flow pressure is a function of velocity and density that is also known to contribute in the control of high energy fluxes at the geostationary orbit. Figure 4.8 presents the average lower band chorus intensities as functions of L, MLT, and P for low (left column), moderate (middle column), and high (right column) pressures. The results are shown for maximum pressure from the current day (P_{0m}, top row), previous day (P_{1m}, middle row), and 2 days (P_{2m}, bottom row) ago in order to take into account the time delay introduced by the magnetospheric system. Similar to solar wind velocity (Figure 4.1), the average chorus intensities rise with increasing pressure. The Kullback-Leibler theory was applied to calculate D_{KL}, between low and moderate (D_{KLlm}), low and high (D_{KLlh}), and moderate and high (D_{KLmh}) pressures for each particular cases of delay, shown in Table 4.3. In this case, the most widespread statistical distribution is observed with current day maximum

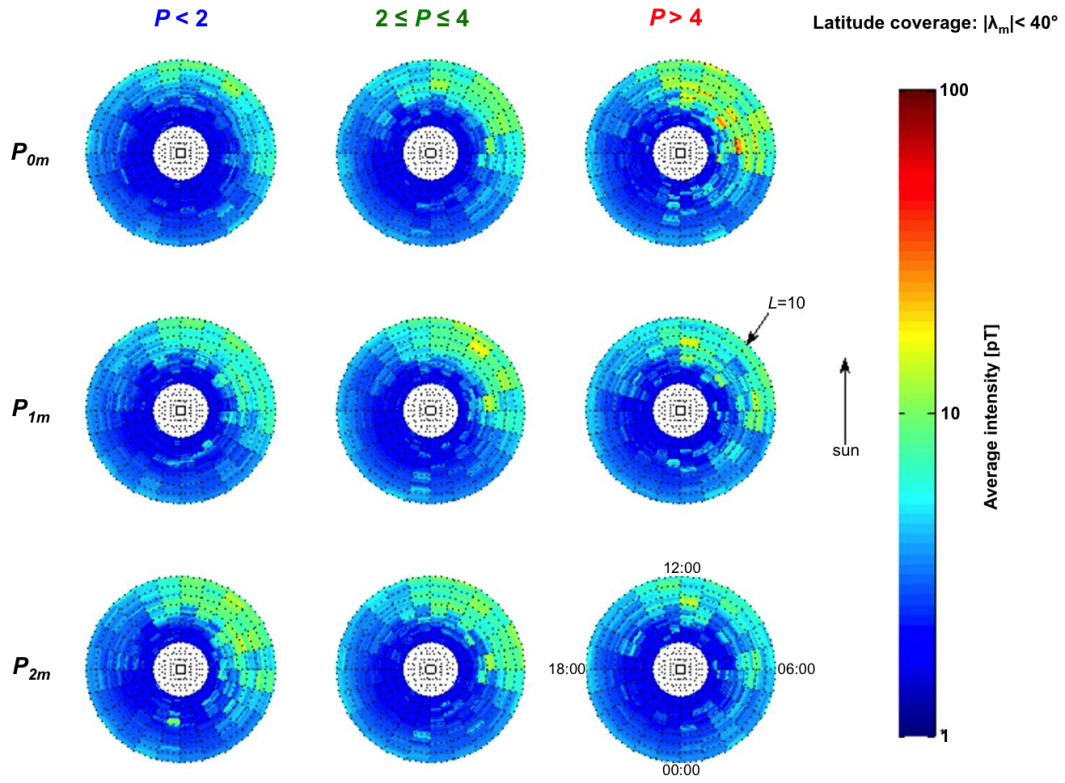

FIGURE 4.8: Average chorus intensities as a function of L, MLT, and P for (left column) low, (middle column) moderate, and (right column) high pressures. Results are shown for maximum pressure observed on (top row) current day (P_{0m}), (middle row) previous day (P_{1m}), and (bottom row) 2 days ago (P_{2m}). The magnetic latitude coverage is $|\lambda_m| < 40°$.

TABLE 4.3: The Kullback-Leibler Distance (D_{KL}) between low and moderate (D_{KLlm}), low and high (D_{KLlh}), and moderate and high (D_{KLmh}) pressures for P_{0m}, P_{1m} and P_{2m} as presented in Figure 4.8. The most widespread statistical distribution is observed with current day maximum pressure (P_{0m}, top row) with the largest D_{KLlh} value of 0.0517

	D_{KLlm}	D_{KLmh}	D_{KLlh}
P_{0m}	0.0296	0.0426	0.0517
P_{1m}	0.0349	0.0429	0.0413
P_{2m}	0.0410	0.0327	0.0453

pressure (P_{0m}, top row) with the largest D_{KLlh} value of 0.0517. Therefore, the current day maximum pressure is used with no time delay for solar wind pressure.

Figure 4.9 shows the equatorial ($|\lambda_m| < 15°$) lower band (a), equatorial upper

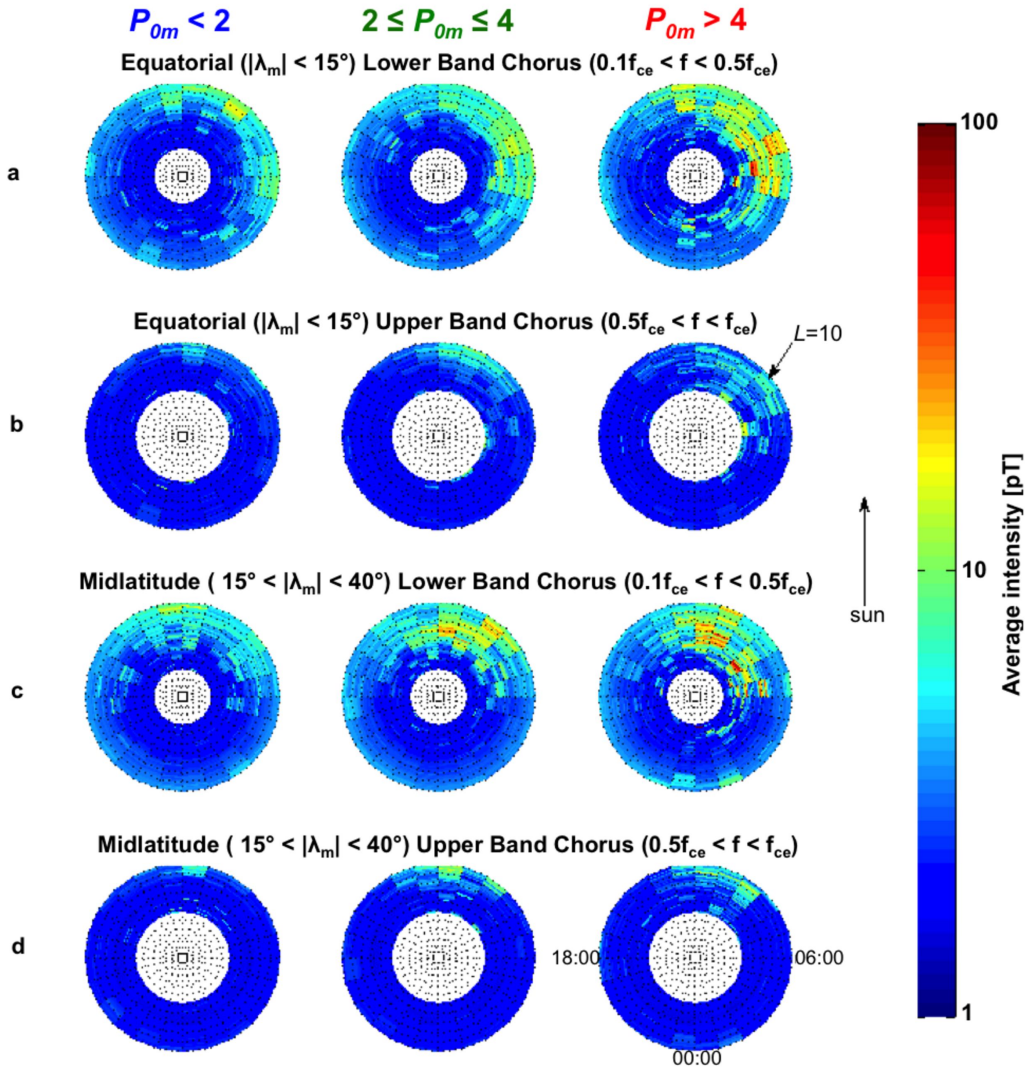

FIGURE 4.9: The (a) equatorial ($|\lambda_m| < 15°$) lower band, (b) equatorial upper band, (c) midlatitude ($15° \leq |\lambda_m| \leq 40°$) lower band, and (d) midlatitude upper band average chorus intensities as a function of L, MLT, and maximum current day pressure (P_{0m}) for low (left column), moderate (middle column), and high (right column) pressures.

band (b), midlatitude ($15° \leq |\lambda_m| \leq 40°$) lower band (c) and midlatitude upper band (d) average chorus intensities as functions of L, MLT, and maximum current day pressure (P_{0m}) for low (left column), moderate (middle column), and high (right column) pressures. The results show significant similarities to solar wind velocity (Figure 4.5) and geomagnetic activity (Figure 4.3) with regards to the distribution of chorus emissions. Generally, the average chorus intensities rise with increasing pressure. The average lower band chorus intensities are larger than the corresponding upper band chorus intensities. The peak lower band chorus intensities rise to 10 pT and 20 pT, primarily from pre-midnight to the afternoon sector, during quiet and moderate conditions, respectively. The largest intensities are observed for lower band chorus during active conditions in the region of $4 \leq L \leq 9$ from 2300 to 1300 MLT (equatorial) and from 0500 to 1400 MLT (midlatitude). The peak intensities of the midlatitude chorus are largely similar in magnitude to the corresponding equatorial chorus intensities. However, the peak intensities for midlatitude region predominantly occur within a smaller MLT sector than the corresponding equatorial chorus intensities. The occurrence of peak lower band chorus intensities during high pressures (Figure 4.9) is slightly lower than during active conditions (Figure 4.3) and during fast solar wind velocities (Figure 4.5). The results prove that the intensity of chorus emission is also dependent upon pressure.

Average Chorus Intensities as a Function of Interplanetary Magnetic Field

High energy flux enhancement depends not only on the solar wind velocity and density but also on the vertical interplanetary magnetic field component (Bz). The southward interplanetary magnetic field ($Bz < 0$) causes large flux enhancement

TABLE 4.4: The Kullback-Leibler Distance (D_{KL}) between low and moderate (D_{KLlm}), low and high (D_{KLlh}), and moderate and high (D_{KLmh}) Bs for Bs_{60}, Bs_{90} and Bs_{120} as presented in Figure 4.10. The only valid statistical distribution is observed with 90 min of delay in Bs (Bs_{90}, middle row) with a D_{KLlh} value of 0.0766

	D_{KLlm}	D_{KLmh}	D_{KLlh}
Bs_{60}	0.0328	0.0894	0.0825
Bs_{90}	0.0393	0.0667	0.0766
Bs_{120}	0.0339	0.0713	0.0631

due to strong coupling with the Earth's geomagnetic field. According to *Tsurutani et al.* [244], the southward interplanetary magnetic field is the most geoeffective parameter. While several studies have shown that the dawn-side and nightside chorus respond quickly to southward interplanetary magnetic field, the exact time delay is not known. Therefore, time delays of up to 1440 min (24 h) at 30 min intervals were studied. In the following analysis $Bs = -Bz$ is defined as the strength of the southward interplanetary magnetic field. Bs <2 nT is categorised as low, 2 nT$\leq$ Bs $\leq$ 4 nT moderate, and Bs >4 nT high. Figure 4.10 shows the average lower band chorus intensities as functions of L, MLT and Bs for low (left column), moderate (middle column), and (right column) high Bs. The results are shown for Bs with 60 (Bs_{60}, top row), 90 (Bs_{90}, middle row), and 120 (Bs_{120}, bottom row) min of delay. Similar to solar wind velocity (Figure 4.4), the average chorus intensities increase with increasing Bs. The Kullback-Leibler theory was applied to calculate D_{KL}, between low and moderate (D_{KLlm}), low and high (D_{KLlh}), and moderate and high (D_{KLmh}) Bs for each particular cases of delay as shown in Table 4.4. In this case, the only valid statistical distribution is observed with 90 min of delay in Bs (Bs_{90}, middle row) with a D_{KLlh} value of 0.0766 (Note that the Kullback-Leibler results for delays of larger than 120 min provided invalid distributions and were increasingly more random).

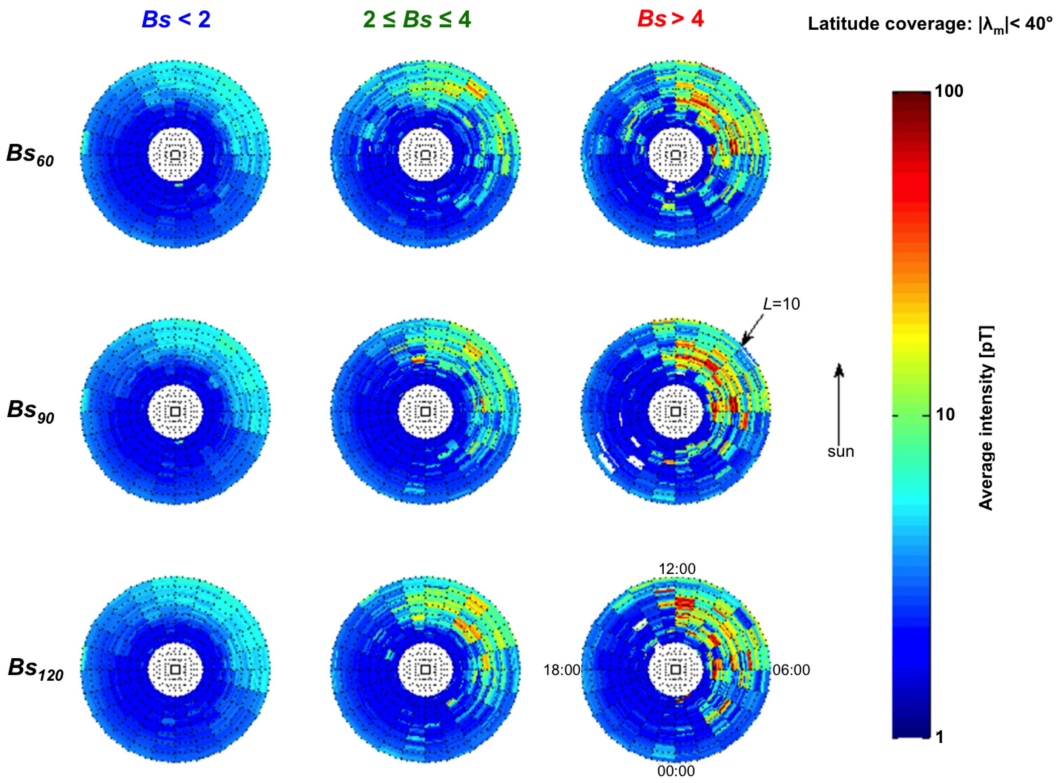

FIGURE 4.10: Average chorus intensities as a function of L, MLT, and Bs for (left column) low, (middle column) moderate, and (right column) high Bs. Results are shown for (top row) Bs with 60 (Bs_{60}), (middle row) 90 (Bs_{90}), and (bottom row) 120 (Bs_{120}) min of delay. The magnetic latitude coverage is $|\lambda_m| < 40°$.

Figure 4.11 shows the equatorial ($|\lambda_m| < 15°$) lower band (a), equatorial upper band (b), midlatitude ($15° \leq |\lambda_m| \leq 40°$) lower band (c) and midlatitude upper band (d) average chorus intensities as functions of L, MLT, and (Bs) with 90 min of delay for low (left column), moderate (middle column), and high (right column) Bs. The results show significant similarities to solar wind velocity (Figure 4.5) and geomagnetic activity (Figure 4.3) with regards to the intensities of chorus emission. The average chorus intensities increase with increasing Bs. The average lower band chorus intensities are larger than the corresponding upper band chorus intensities. The upper band chorus intensities are mostly weak with peak values of less than 10 pT. The peak equatorial lower band chorus intensities are more

widely distributed (from pre-midnight to early afternoon in the region of $4 \leq L \leq 9$) compared to the midlatitude lower band chorus (from dawn to afternoon in the region of $4 \leq L \leq 9$). Also, the peak lower band chorus intensities of 50 pT are more commonly observed with high Bs than with low solar wind density and high pressure.

Overall, results indicate that the intensity of chorus emission is not only dependent on geomagnetic activity but also dependent on solar wind velocity, density, pressure, and vertical interplanetary magnetic field component. Bs and Solar wind velocity are evidently the most influential parameters having the largest D_{KL} value between the extreme ends of the distributions (D_{KLlh} =0.0766) and (D_{KLsf} =0.0635), respectively, followed by pressure (D_{KLlh} =0.0517) and density (D_{KLlh} =0.0500). The results here are in line with previous studies that have also identified solar wind velocity as highly influential solar wind parameter that control the flux of energetic electrons at geostationary orbit.

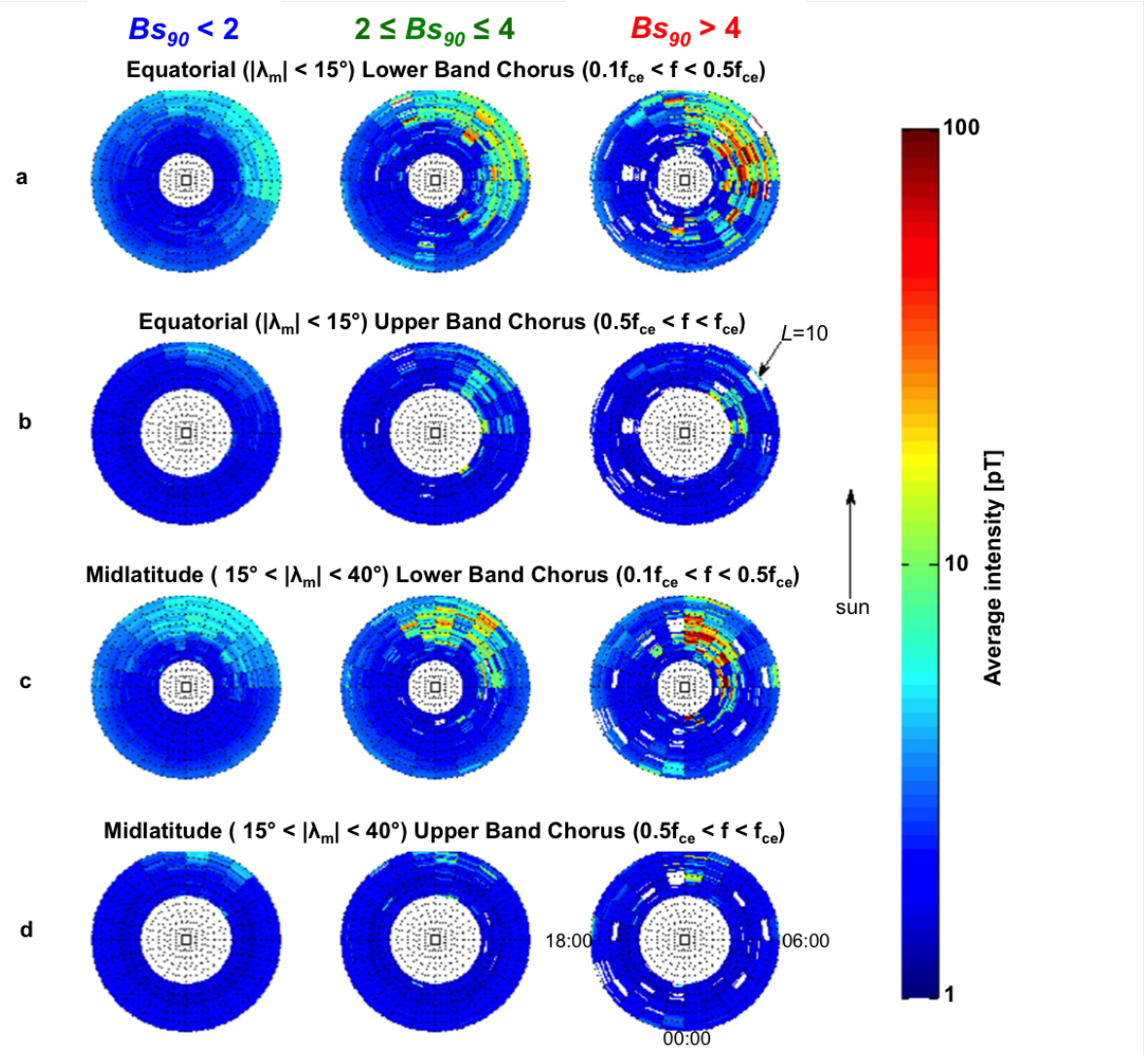

FIGURE 4.11: The (a) equatorial ($|\lambda_m| < 15°$) lower band, (b) equatorial upper band, (c) midlatitude ($15° \leq |\lambda_m| \leq 40°$) lower band, and (d) midlatitude upper band average chorus intensities as a function of L, MLT, and (Bz_{90}) with 90 min of delay for low (left column), moderate (middle column), and high (right column) Bs.

4.2.3 Discussions and Conclusions

The present study examined almost four years (1 January 2004 to 29 September 2007) of STAFF data from Double Star TC1 and OMNI database. The results are largely consistent but far more statistically significant than previous studies that presented model wave distributions in the inner magnetosphere under different values of geomagnetic activity as expressed by the geomagnetic indices [4, 168, 169]. In particular, the results here agree with the results of *Meredith et al.* [169] who used the geomagnetic index, Ae, to study the distributions of the upper and lower band chorus intensities. However, in the present study the set of parameters of the wave distributions was expanded to include the solar wind parameters (velocity, density, pressure, and Bs) in addition to the geomagnetic activity. The results strongly suggest that the intensity of chorus emission is not only dependent on geomagnetic activity but also dependent on solar wind parameters. The strong dependency between the intensity of chorus emission and the solar wind parameters shown here is not peculiar given the fact that various studies in the past (e.g., [63, 78, 222]) identified a high correlation coefficient between geomagnetic indices and solar wind parameters.

Generally, the average upper band chorus intensities are relatively weak with peak values largely below 10 pT in all cases (chorus intensity as a function of geomagnetic activity, solar wind velocity, density, pressure, and Bs). The largest intensities of the order 50 pT are observed for lower band chorus during active conditions, high solar wind velocities, low solar wind densities, high pressures, and high Bs correspondingly. Perhaps, the upper band chorus intensities are weaker than the lower band chorus because the generation of the upper band chorus requires higher anisotropy of resonant electrons [126]. It is known that

electron injection and anisotropy depends upon geomagnetic activity and solar wind parameters. The resonant anisotropy and the resonant numbers of electrons largely determine the chorus wave instability [258, 259]. The natural enhancement of electron anisotropy in the noon sector may result in high occurrence of dayside chorus at higher L [253] where critical stably trapped flux levels are low. Electron injection would further enhance wave excitation [139]. This could account for the fact that chorus wave activities are associated with geomagnetic activity and also solar wind parameters.

The occurrence of peak lower band chorus intensities are most extensive during active conditions, fast solar wind velocities, and high Bs (from 2300 to 1300 MLT in the region of $4\leq L \leq 9$) but slightly less extensive during low solar wind densities and high pressures (from 500 to 1200 MLT in the region of $4\leq L \leq 9$). The peak midlatitude ($15^\circ \leq |\lambda_m| \leq 40^\circ$) chorus intensities predominantly occur within smaller MLT slots than the corresponding equatorial ($|\lambda_m| < 15^\circ$) chorus intensities for both the upper and lower band chorus. Possibly, this is because Landau damping weakens some of the waves as they propagate to higher latitudes, where the wave normal angles are more oblique [140, 141].

Evidently, the intensity of chorus emission is more dependent on solar wind velocity and Bs than solar wind density and pressure. Based on the Kullback-Leibler theory, the most widespread distribution was observed with Bs ($D_{KLlh} = 0.0766$) and solar wind velocity (D_{KLsf} =0.0635) followed by pressure (D_{KLlh} =0.0517) and density (D_{KLlh} =0.0500). This suggests that Bs and velocity are the most influential solar wind parameter that affect the evolution of the magnetospheric chorus wave intensities, consistent with the results of *Kim et al.* [128] who presented an empirical model of the global distributions of the magnetospheric chorus

amplitude using an artificial neural network and utilised the instantaneous measurement of the solar wind parameters as input. However, the present study takes into account the time delay introduced by the magnetospheric system. The results demonstrates that the most widespread statistical distributions are observed with a time delay of 90 min in Bz and a time delay of 1 day in solar wind velocity and density.

Studies of the evolution of energetic electron fluxes rely heavily on the numerical codes in order to model energy and pitch angle diffusion due to electron interaction with plasma waves in the frame of quasi-linear approximation. Therefore, including the solar wind parameters in addition to the geomagnetic activity in the statistical wave models will benefit those studies, provide a better representation of the wave distributions in the magnetosphere, and improve our knowledge of the acceleration and loss of radiation belt electrons.

4.2.4 Acknowledgments

Double Star was a joint mission by the European Space Agency and the China National Space Administration. The STAFF and DWP experiments, operations and data analysis, were supported by CNES (France), STFC (UK) and ESA. The OMNI data were obtained from the GSFC/SPDF OMNIWeb interface at http://omniweb.gsfc.nasa.gov.

4.3 Summary

Naturally occurring electromagnetic waves have attracted significant attention in recent decades for their crucial role in the acceleration and loss of energetic electrons that ultimately change the dynamics of the radiation belts. The interactions of electrons with chorus waves play an important role in both the acceleration and loss of radiation belt electrons. The distribution of chorus waves in the inner magnetosphere is commonly presented under different values of geomagnetic activity as expressed by the geomagnetic indices (Ae, Kp, and Dst). However, it has been shown that only around 50% of geomagnetic storms increase flux of relativistic electrons at geostationary orbit, while 20% causes a decrease and the remaining 30% has relatively no effect. Also, the geomagnetic indices are indirect, nonspecific parameters compiled from imperfectly covered ground based measurements that lack time history. Therefore, in the present chapter the set of parameters of the wave distributions was expanded to include the solar wind parameters in addition to the geomagnetic activity. This study examined almost four years (01, January, 2004 to 29, September, 2007) of STAFF data from Double Star TC1 combined with geomagnetic indices and solar wind parameters from OMNI database in order to present a comprehensive model of wave magnetic field intensities for the chorus waves as functions of MLT, L, λ_m, geomagnetic activity, and solar wind parameters. The results indicated that the intensity of chorus emission was dependent on geomagnetic activity and solar wind parameters. The peak chorus intensities were observed primarily on the dawn-side during high solar wind velocity, low density, high pressure, and high Bs respectively. The average chorus intensities are more extensive and stronger for lower band chorus than the corresponding

upper band chorus. The results have been published in the peer-reviewed international Journal of Geophysical Research in August 2014 (*Aryan, H., Yearby, K., Balikhin, M. A., Agapitov, O. V., Krasnoselskikh, V., and Boynton, R. (2014), Statistical study of chorus wave distributions in the inner magnetosphere using Ae and solar wind parameters, J. Geophys. Res. Space Phys., 119, 6131-6144, doi: 10.1002/2014JA019939*).

Chapter 5

Particle Acceleration in Interplanetary Shock Waves

5.1 Introduction

Shock waves occur ubiquitously throughout the universe and form the most fundamental areas of plasma physics research [127, 185, 202, 204]. The study of shock waves began before the discovery of the solar wind in 1966 [127]. At the time, the existence of shock waves in high temperature collisionless plasma was hugely debated. However, upon the discovery of the solar wind in early 1960's, the rapid rise time of the magnetic storms suggested very thin collisionless shocks [127, 202, 203]. The mean free path in the solar wind was calculated as approximately one Au , the distance from the Earth to the Sun, $Au \approx 1.5 \times 10^8$ km. Hence, collisions in the solar wind are insignificant, given the fact that the shock thickness is significantly smaller than the mean free path.

The most widely studied forms of shock waves in the solar system include Interplanetary (IP) collisionless shocks, associated with CMEs and CIRs [201], and planetary bow shocks. The Earth's bow shock, where the Earth's magnetic field forms an obstacle to the supersonically flowing solar wind, was the first collisionless shock wave discovered [114, 175, 205, 223]. The Earth's bow shock along with the bow shocks of other planets are classified as standing shocks. In contrast, the interplanetary collisionless shocks are propagating shocks, which are formed when supersonic solar wind, generally associated with CMEs and CIRs, interact with the slower ambient solar wind. The solar wind will be left with higher velocity, density, temperature, and pressure, in the wake of a collisionless shock crossing.

Shock waves play a significant role in the processes of space weather, the control of the dynamics and energisation of the terrestrial magnetosphere, and the energisation of the radiation belts where many important satellites operate. This chapter attempts to describe the most important properties of collisionless shock waves and study their behaviour in CMEs and CIRs which leads to particle acceleration.

5.2 Interplanetary Collisionless Shocks

Collisionless shocks are propagating waves that occur ubiquitously throughout the universe, which characterises the fundamental processes that occur both within the heliosphere and throughout the universe. Some of the most high profile collisionless shocks within the universe include, the planetary bow shocks, interplanetary shocks in the heliosphere, the cosmological structure formation shocks, the giant termination shocks of radio galaxies, and the supernova remnant shocks.

Collisionless shocks are important scientifically and practically. The interplanetary collisionless shocks can energise and accelerate charged particles of plasma. This contribute to energetic proton events at the Earth orbit that are hazardous to many space based technological systems. Knowledge of mechanisms by which charged particles are energised and accelerated will be highly beneficial to studies of all shocks, in particular, the planetary bow shocks and interplanetary collisionless shocks.

A collisionless shock wave is a transition between two regions of steady flow, where many physical processes occur on scales of the order of the ion and electron gyro-radius and inertial length. In the shock frame, the plasma quantities measured in the un-shocked region, upstream, is given a subscript u, while the plasma quantities measured in the shocked region, downstream, is given a subscript d.

The most important processes in a collisionless shock, that determines the main characteristics of energy repartition, takes place near the transition region [77, 130]. The transition region is the region between the point of lowest magnetic field immediately before the shock and the point of highest magnetic field immediately after the shock[65].

In the shock reference frame, plasma parameters, such as, solar wind velocity, magnetic field, density, temperature, and pressure change across a shock. The normal vector to the shock frame, shock normal, is defined as $\hat{n}$, while, the angle between the shock normal vector and the magnetic field, shock normal angle, is defined as θ_{Bn}. If the shock normal angle $\theta_{Bn} > 45°$, the shock is said to be quasi-perpendicular, otherwise, if the shock normal angle $\theta_{Bn} < 45°$ the shock is classified as quasi-parallel. In quasi-perpendicular shocks, the transition from upstream to downstream is generally stable and characterised by a steep rise in

the magnetic field. In contrast, the transition from upstream to downstream is largely turbulent in the case of quasi-parallel shocks. In the later case, particles can escape upstream generating an extended shock transition region.

In the solar wind frame, shocks moving away from the Sun are known as forward shocks, and vice versa. Forward shocks are commonly formed ahead of propagating CMEs and CIRs, where supersonic solar wind, associated with CMEs and CIRs, interact with the slower ambient solar wind. Reverse shocks may also form, usually at the trailing edge of CMEs and CIRs. The formation of reverse shock is more common in CIRs due to their unique propagation profile.

Another important property of shock waves is defined by the relative magnitude of the upstream velocity, in the shock frame, characterised as slow or fast shock given by equations 5.1 and 5.2.

$$V_{\text{slow}}^2 = \frac{1}{2}\left[\left(c_s^2 + V_A^2\right) - \sqrt{\left(c_s^2 + V_A^2\right)^2 - 4c_s^2 V_A^2 \cos^2\theta_{Bn}}\right] \tag{5.1}$$

$$V_{\text{fast}}^2 = \frac{1}{2}\left[\left(c_s^2 + V_A^2\right) + \sqrt{\left(c_s^2 + V_A^2\right)^2 - 4c_s^2 V_A^2 \cos^2\theta_{Bn}}\right] \tag{5.2}$$

Where, V_A is the Alfven Velocity and c_s is the sonic speed. In the solar wind frame, the normal component of a slow shock propagates with velocity V_{slow}, whereas, the normal component of a fast shock propagates with velocity V_{fast}. The slow shocks have sub-alfvenic flows both upstream and downstream of the shock [109]. At the

Earth's orbit, distance of 1 *Au* away from the Sun, the majority of observed shocks are fast forward with a small proportion of slow shocks [51, 150, 254, 255].

5.3 Observation of Shocks Associated with Coronal Mass Ejections

5.3.1 Introduction

Interaction of the CMEs with the solar wind may lead to the formation of interplanetary collisionless shocks and also contribute to the acceleration of solar energetic protons in both the vicinity of the Earth and the interplanetary medium. Fermi type ion acceleration at the collisionless shocks takes place due to multiple crossings of shocks by a particular ion. Initially a seed population of the reflected ions is formed which excites wave instabilities upstream of the shock front. Interaction of the reflected ions with formed upstream wave field leads to the ion scattering. Part of the reflected ions are scattered back to the shock front that can be reflected back again and so on. Each time a particular ion is reflected from the shock front it gains energy. While such a general scenario is widely accepted a few unsolved problems still remain, for example, the origin of the seed population and a comprehensive self-consistent model of plasma wave interactions and ion scattering in the wave field. Currently, Magnetohydrodynamics (MHD) codes are used to model the formation and propagation of collisionless shocks associated with CMEs. To forecast solar energetic protons on the basis of these MHD models requires waves and ion seed populations to be added to the field structure obtained by the MHD

codes. This cannot provide accurate results as the process of acceleration is sensitive to both the peculiarities of the seed population and the distribution of wave amplitudes, that cannot be obtained by the MHD approximation.

In the present study it is shown that at least for some particular CMEs the MHD approach is unable to account even for the formation and evolution of a CME associated shock. One of the main motivation is the results of *Russell et al.* [201] showing that for CIR associated shocks it is the region between Venus and the Earth where stronger shocks are formed as a result of coalescence of weaker shocks and *Russell et al.* [201] even refers to that region as the incubator of shocks. In the present study it is shown that this is also the case at least for some CMEs.

5.3.2 Description of the Data Set

The European Space Agency launched Venus Express in November 2005 using a Soyuz-Freget launcher. The VEX satellite carry a number of different instruments to study the Venusian atmosphere, surface, and plasma environment in more detail. The satellite has been in operation since April 2006 with an elliptical polar orbit of 24 h period and a 12 Venus radius. Aboard Venus Express the fluxgate Magnetometer (MAG) measures the magnetic field vector with a sampling rate of 128 Hz [262]. This study analysed 8 months (from 01 July 2007 to 31 October 2007 and from 01 February 2009 to 31 May 2009) of magnetic field measurements to identify shock crossings at the Venusian orbit ($0.72 Au$) during the 2007 and 2009 solar wind conjunction periods between Venus and the Earth.

The office of space mission and payload development division of NASA launched the Advanced Composition Explorer (ACE) in August 1997 using a McDonnell-Dougles Delta II 7920 launch vehicle. ACE is located at 1 Au upstream of Earth and carry a number of different sensors and instruments to measure and compare the composition of several samples of matter [225]. The magnetometer (MAG) aboard ACE consist of a set of wide range triaxial twin sensors that are mounted remotely from the spacecraft on separate booms to reduce the effect of magnetics from other instruments and the spacecraft. They measure the local IMF magnitude and direction at 30 Hz in order to determine the large scale fluctuation and structure characteristics of the IMF. This study analysed 8 months (from 01 July 2007 to 31 October 2007 and from 01 February 2009 to 31 May 2009) of magnetic field measurements to identify shock crossings at the Earth orbit ($1Au$) during the 2007 and 2009 solar wind conjunction periods between Venus and the Earth.

The CME parameters, such as eruption time, direction of propagation, speed, acceleration, cloud mass, kinetic energy and angular width were obtained from the Large Angle and Spectrometric Coronagraph Experiment (LASCO) CME catalogue which is available online ($http : //cdaw.gsfc.nasa.gov/CME_list/$). LASCO is one of several instruments aboard the Solar and Heliospheric Observatory (SOHO) spacecraft which was launched in December 1995 using an Atlas II-AS (AC-121) as part of an international collaboration between ESA and NASA to study the Sun. The SOHO mission was designed to study the Sun's corona, structure and dynamics of the solar interior.

The ENLIL simulation model provided by the Community Coordinated Modelling Centre (CCMC) at Goddard Space Flight Centre through their public Runs on

Request system ($http://ccmc.gsfc.nasa.gov$) were used to simulate the propagation of CMEs. The CCMC is a multi-agency partnership between NASA, AFMC, AFOSR, AFRL, AFWA, NOAA, NSF and ONR. The ENLIL with a cone model [180] which is a 3D time dependent MHD solar wind model, capable of representing CMEs and propagating features through a realistic model of the solar wind, was developed by the D. Odstrcil at the University of Colorado at Boulder. The CCMC version of the ENLIL model has been verified against data recorded near Earth showing that the model provides good predictions of the CME arrival times (e.g., [64, 233]).

5.3.3 Events

Solar wind conjunction between Venus and the Earth occur when the two planets are in line with the Sun. Subsequently, any magnetic structure associated with a particular CME crossing would be observed by both VEX and ACE magnetometers with a time delay depending on the speed of the CME. During solar wind Venus-Earth conjunction periods in 2007 and 2009 SOHO/LASCO observed a halo and a partial halo CME. The partial halo CME eruption occurred at 01 : 31 UTC on 29 July 2007 followed by a halo CME eruption a day later at 04 : 54 on 30 July 2007. The propagation of these CMEs were simulated in order to predict their arrival times at the Venusian and the Earth orbits. The simulations were performed using the ENLIL with a cone model provided by CCMC.

Figures 5.1 presents a snapshot of the CCMC's ENLIL with a cone model simulation at 20 : 00 on 30 July 2007. The leading partial halo CME is at the Venusian orbit while the trailing CME is still expanding close to the Sun. The structures of the CMEs are clear through density variations. At the leading edge of the

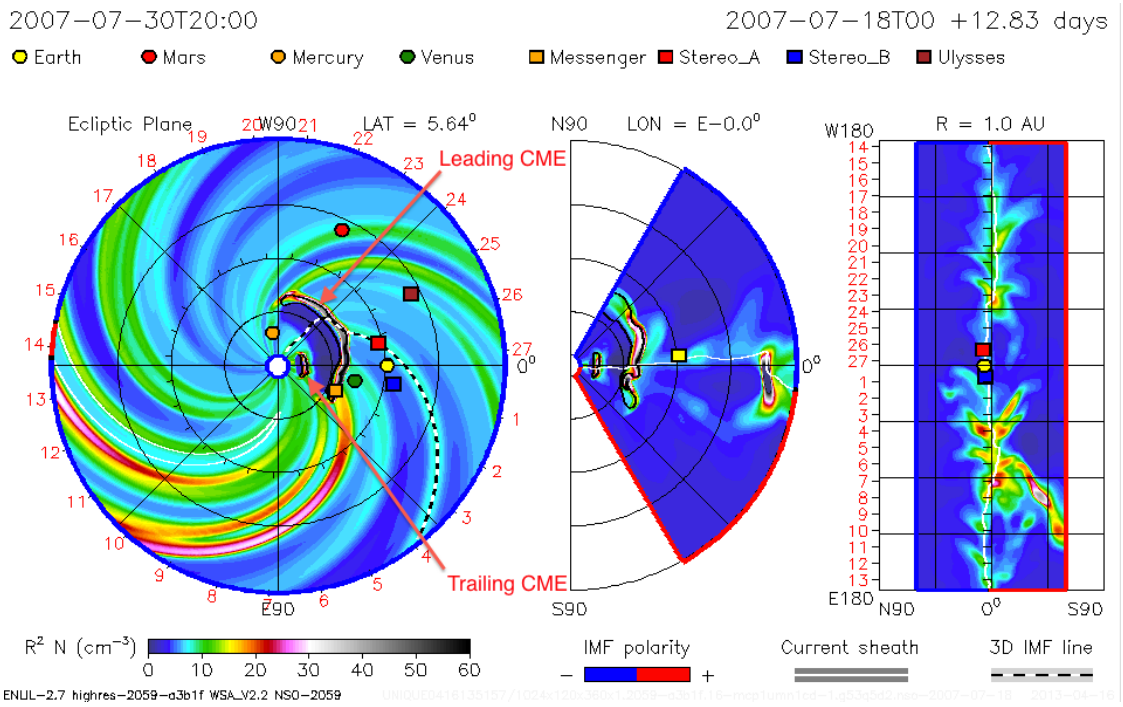

FIGURE 5.1: A snapshot of the CCMC's ENLIL with a cone model simulation at 20 : 00 on 30 July 2007. The leading partial halo CME is at the Venusian orbit while the trailing CME is still expanding close to the Sun. The structures of the CMEs are clear through density variations. At the leading edge of the CMEs plasma material is compressed creating a region of high plasma density. Conversely, at the trailing edge of the CMEs plasma material is rarefied creating a region of low plasma density. The estimated arrival time of the leading partial halo CME at Venus is approximately 20 : 00 on 30 July 2007. The red arrows point to the leading and trailing CMEs.

CMEs plasma material is compressed creating a region of high plasma density. In contrast, at the trailing edge of the CMEs plasma material is rarefied creating a region of low plasma density. In addition, a snapshot of the CCMC's ENLIL with a cone model simulation at 20 : 00 on 31 July 2007 is shown in Figures 5.2. At this stage, the leading partial halo CME is at the Earth orbit while the trailing CME is on the verge of arriving at the Venusian orbit.

The above simulation results presented in Figures 5.1 and 5.2 were used to estimate the arrival time of the leading CME at VEX and ACE as approximately 20 : 00 on 30 July 2007 and 20 : 00 on 31 July 2007 respectively. On the other hand

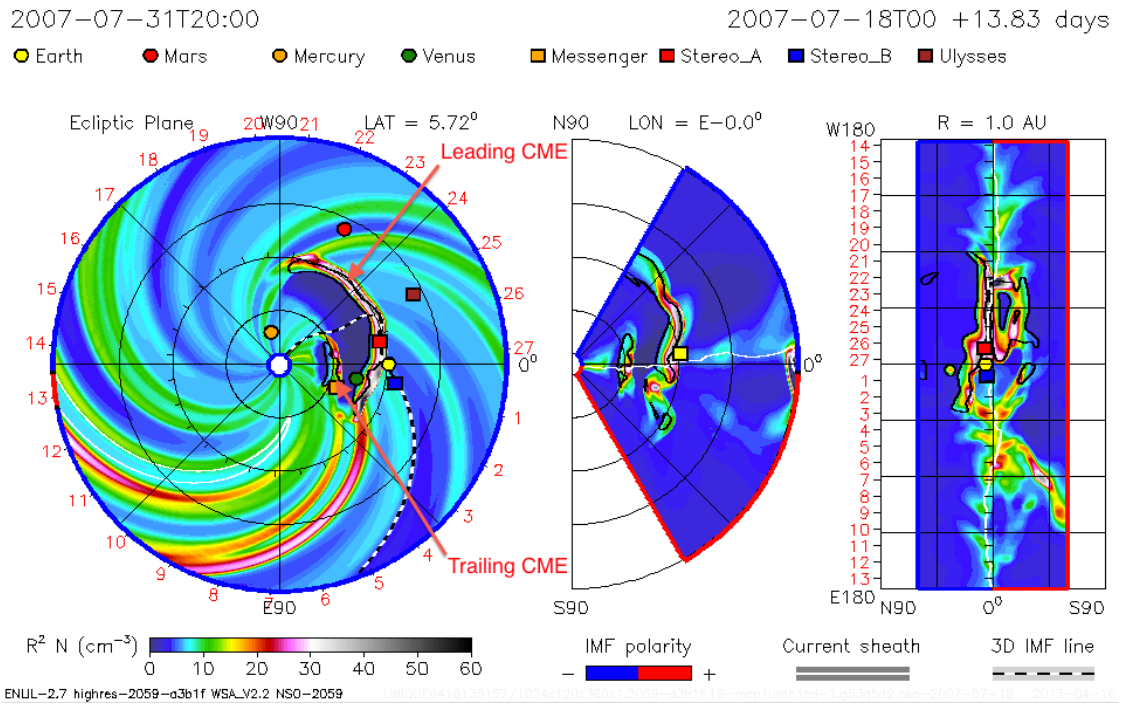

FIGURE 5.2: A snapshot of the CCMC's ENLIL with a cone model simulation at 20 : 00 on 31 July 2007. The leading partial halo CME is at the Earth orbit while the trailing CME is on the verge of arriving at the Venusian orbit. The structures of the CMEs are clear through density variations. At the leading edge of the CMEs plasma material is compressed creating a region of high plasma density. Whereas, at the trailing edge of the CMEs plasma material is rarefied creating a region of low plasma density. The estimated arrival time of the leading partial halo CME at the Earth is approximately 20 : 00 on 31 July 2007. The red arrows point to the leading and trailing CMEs.

the estimated arrival time of the trailing CME at VEX and ACE was estimate as approximately 02 : 00 on 1 August 2007 and 02 : 00 on 2 August 2007 respectively. The estimated arrival times from the ENLIL with a cone model provides a time slot to search for possible shocks associated with the crossing of the corresponding CMEs. The main advantage of this method is that it eliminates any ambiguity regarding the CME crossing time. Generally, the majority of CME associated shocks travel ahead of the propagating CME [113]. Therefore, the CME associated shock crossings would mainly be expected to occur close to the CME arrival time at the Venusian and the Earth orbits.

The magnetic field measurements recorded by the magnetometers aboard VEX and ACE confirm the crossing of the leading partial halo CME at VEX (Figures 5.3) and ACE (Figure 5.4). During these periods a number of nonlinear structures reminiscent of shock crossings have been observed both at VEX and ACE. All such structures were analysed in order to identify shock crossings using the same shock crossing criteria as developed by *Russell et al.* [201]. According to this criteria, for a shock crossing the directions of the shock normal (B_n), the main magnetic field component and the component in the shock plane parallel to the projection of the upstream field (B_L) should not cross zero in the shock coordinate frame. Also a shock crossing is characterised by a sharp single directional jump in the magnetic field measurements [201] with the Mach number crossing one between upstream and downstream of the shock.

When the above criteria was applied to the nonlinear structures reminiscent of shock crossings associated with the leading CME it was found that six structures observed by VEX at times: 14.54, 15.51, 18.00, 18.91, 19.12, and 19.71 UTC hours on 30 July 2007, and four structures observed by ACE at times: 19.00, 19.89, 20.03, and 20.11 UTC hours on 31 July 2007 all marked by green dotted lines in Figures 5.3 and 5.4 corresponded to shock crossings with the presence of a sharp single directional jump in the magnetic field and the generation of shock associated waves either upstream/downstream or both of the shock. The vertical orange dotted lines represent examples of nonlinear structures that has not fully formed into a shock, and the red dotted lines represent some examples of nonlinear structures that did not fulfil the criteria for a shock crossing. A close-up view of all the above corresponding shocks is given in Figure 5.5 (VEX) and Figure 5.6 (ACE).

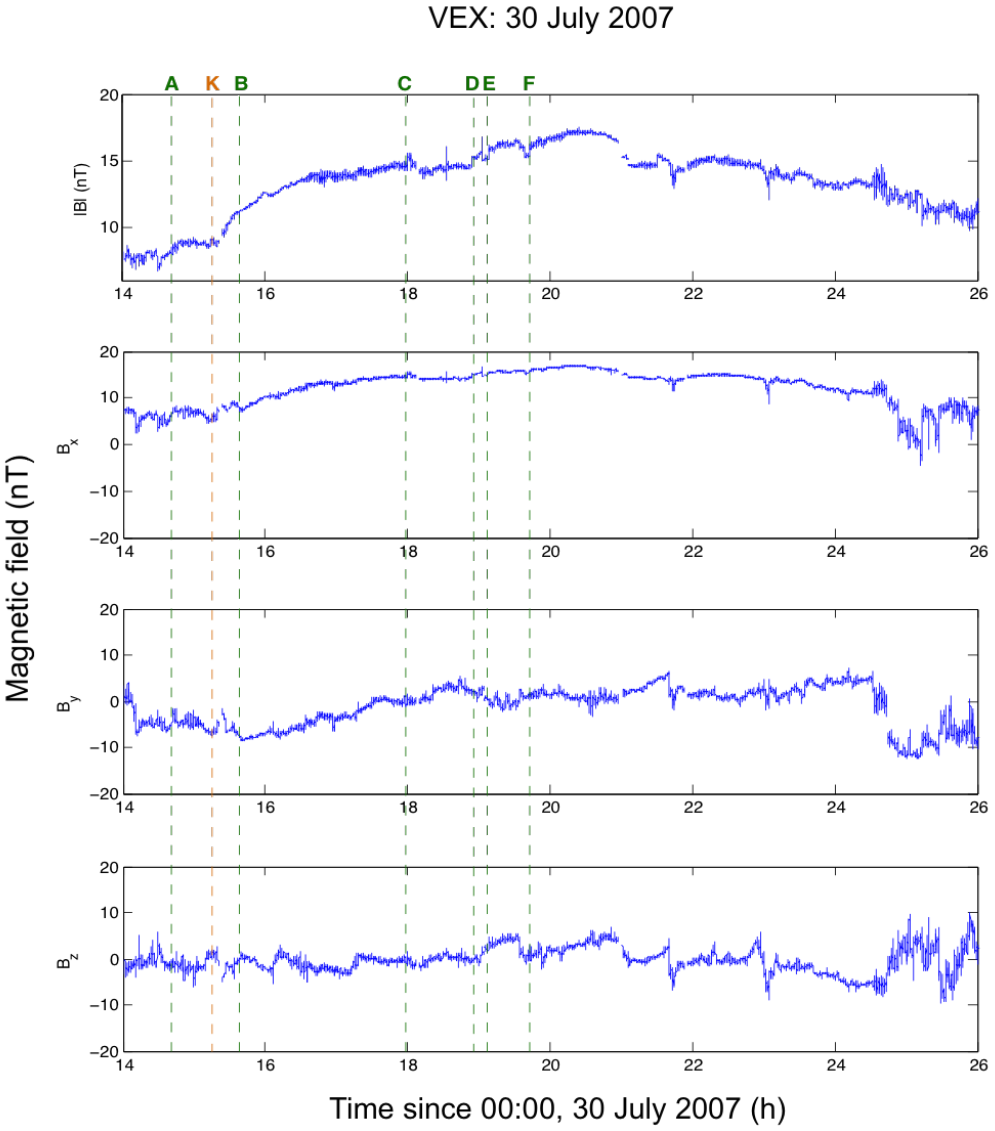

FIGURE 5.3: The magnetic field data recorded by the magnetometer aboard VEX during the CME crossing on 30 July 2007. The vertical green dotted lines mark the shock crossing times (A : F) and the vertical orange dotted line (K) represent an example of a nonlinear structure that has not fully formed into a shock.

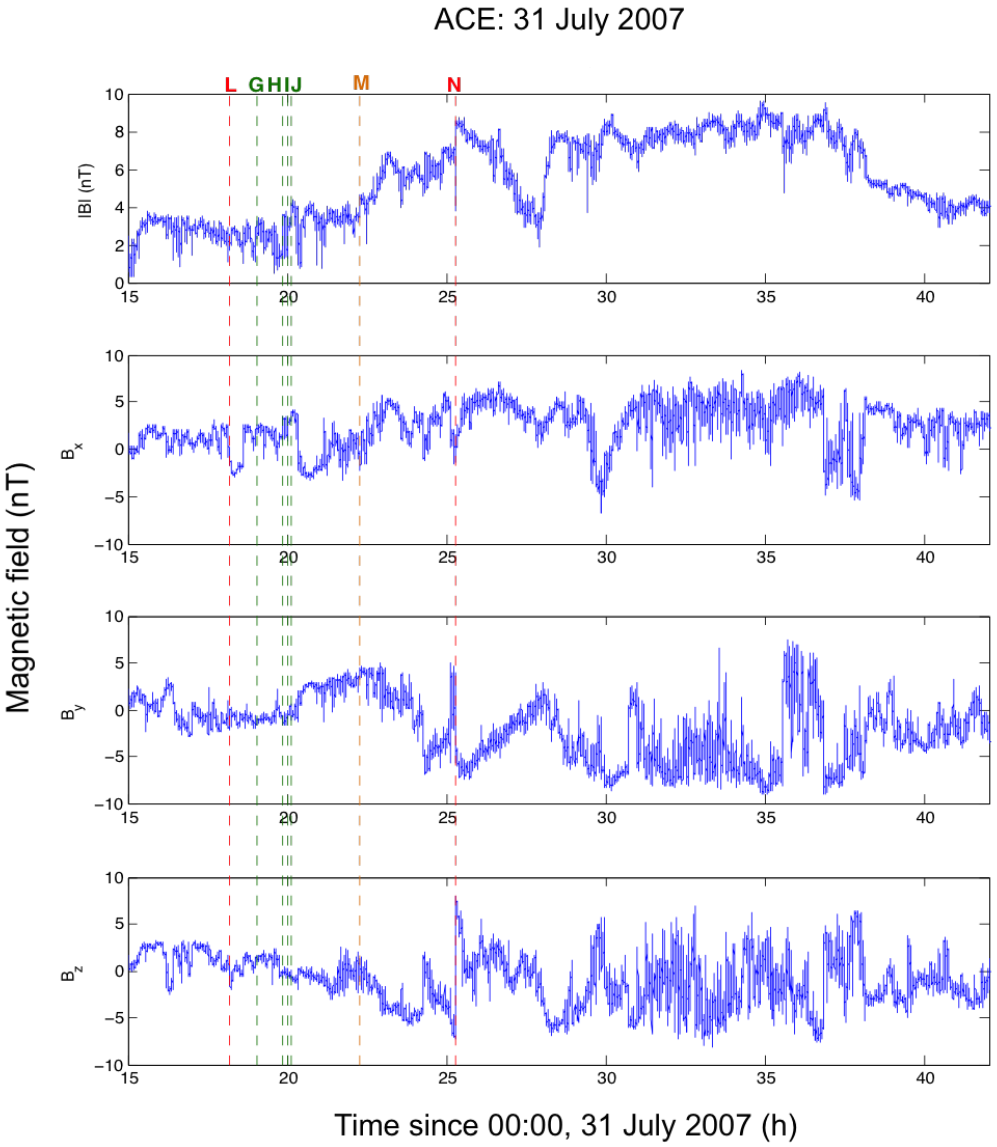

FIGURE 5.4: The magnetic field data recorded by the magnetometer aboard ACE during the CME crossing on 31 July 2007. The vertical green dotted lines (G : J) mark the shock crossing times, the vertical orange dotted line (M) represent an example of a nonlinear structure that has not fully formed into a shock, and the red dotted lines (L and N) represent some examples of nonlinear structures that did not fulfil the criteria for a shock crossing.

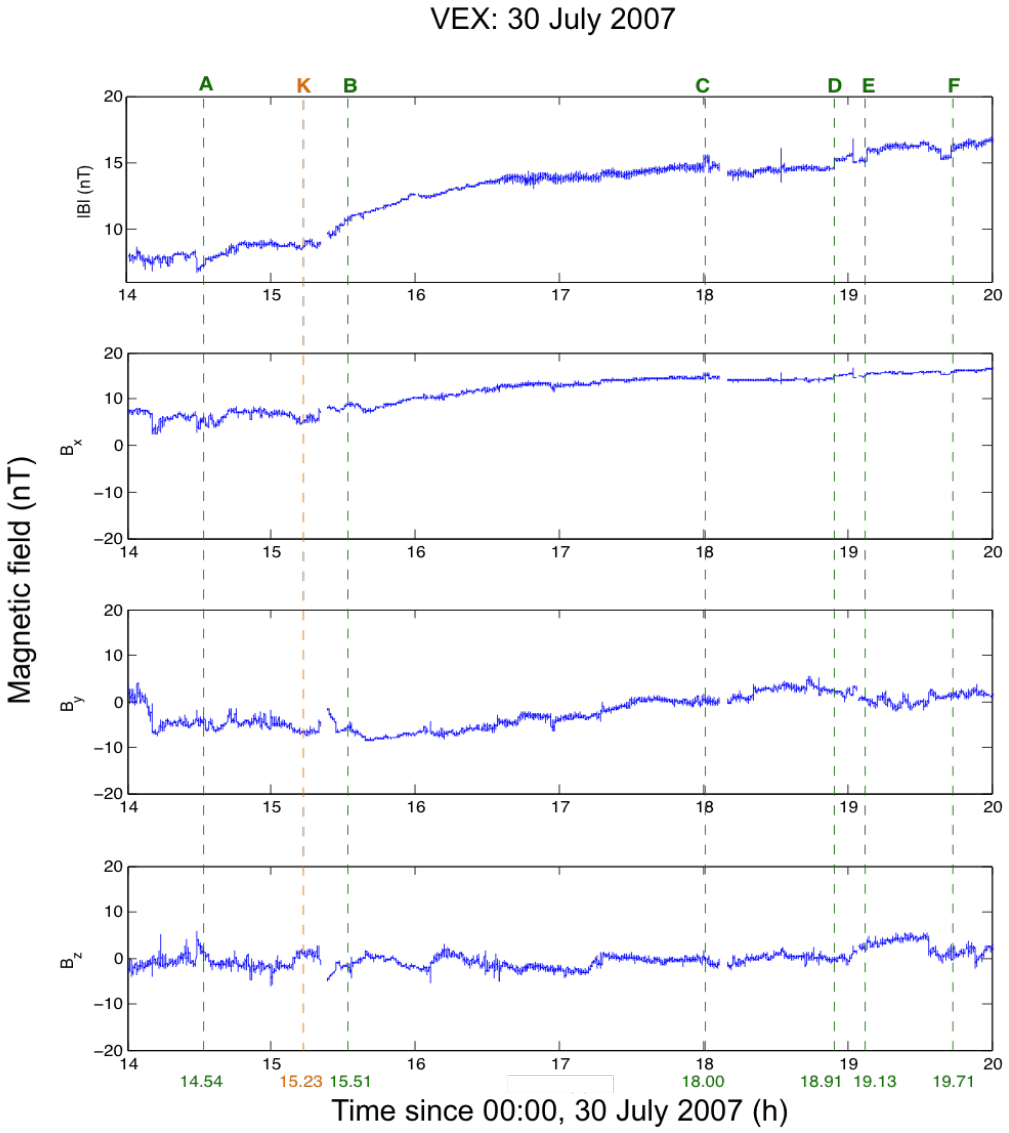

FIGURE 5.5: The magnetic field data recorded by the magnetometer aboard VEX during the CME crossing on 30 July 2007. A close-up view of the shocks presented in Figure 5.3. Caption of Figure 5.3 apply.

Table 5.1 provide a summary of observed shocks associated with the crossing of the leading CME at VEX and ACE. Table 5.1 specify the shock crossing date, the shock crossing time, the magnetic field jump (ΔB), the ratio of magnetic field jump over magnetic field ($\Delta B/B$), the angle between the magnetic field and the shock normal (θ_{Bn}) and the Mach number.

There are fairly noticeable similarities amongst the six shocks observed by VEX

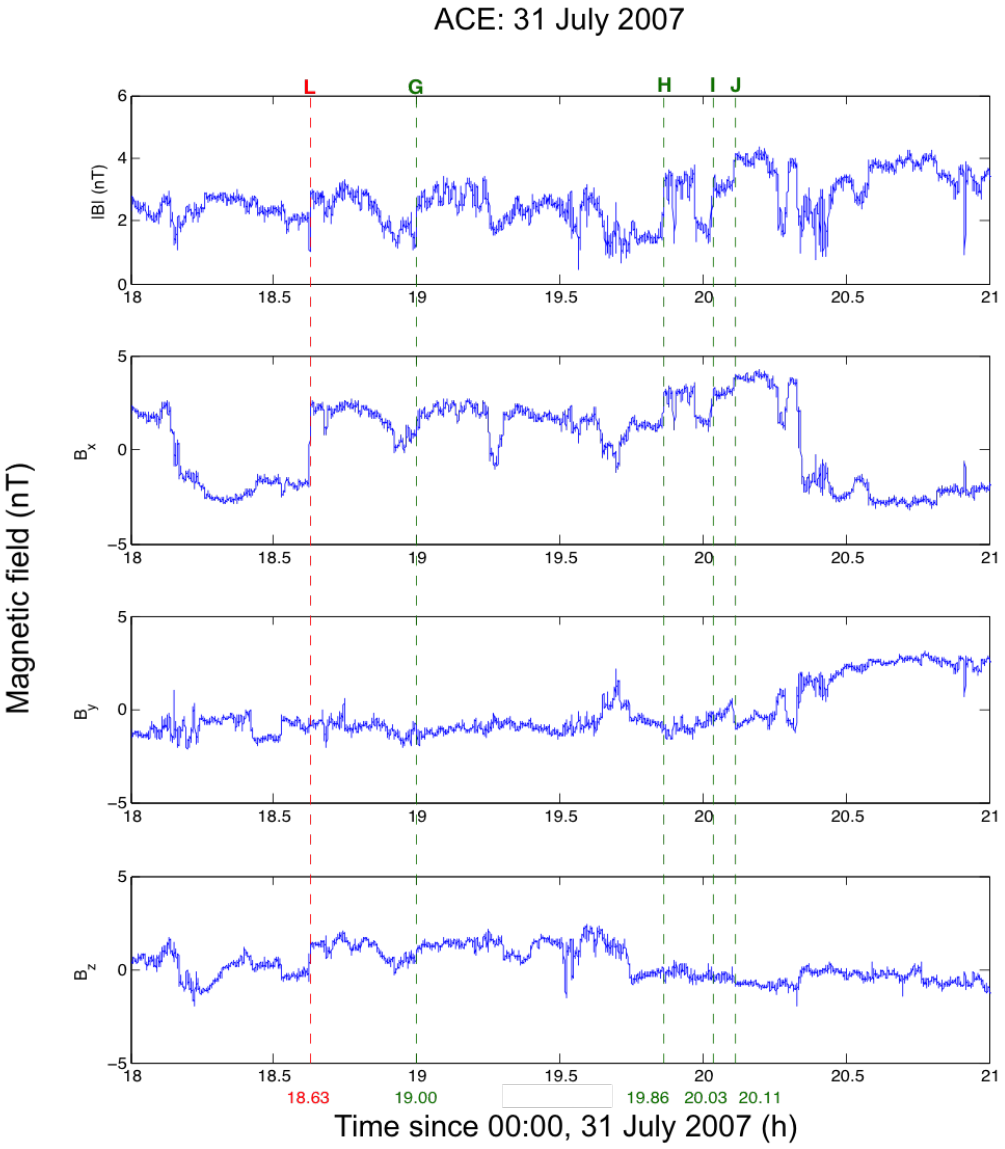

FIGURE 5.6: The magnetic field data recorded by the magnetometer aboard ACE during the CME crossing on 31 July 2007. A close-up view of the shocks presented in Figure 5.4. Caption of Figure 5.4 apply.

which are classified as weak shocks with relatively small values of $\Delta B/B$ (0.07, 0.04, 0.05, 0.05, 0.05, and 0.05), field jump ΔB (0.51, 0.38, 0.71, 0.72, 0.72, and 0.82), and Mach number (1.04, 1.02, 1.04, 1.05, 1.04 and 1.05). The first three shocks (shock A, B, and C) observed by VEX (as presented in Table 5.1) are quasi-parallel with $\theta_{Bn} < 45°$ (5°, 28°, and 36° respectively). However, the final three shocks (shock D, E, and F) are quasi-perpendicular with $\theta_{Bn} > 45°$ (87°, 63°,

TABLE 5.1: A summary of shock properties observed at VEX and ACE associated with the leading CME crossing. Shocks A, B, C, D, E and F were observed by VEX on 30 July 2007, whereas shocks G, H, I, J were observed by ACE on 31 July 2007. The columns of the table left to right specify the shock crossing date, the shock crossing time, the magnetic field jump (ΔB), the ratio of magnetic field jump over magnetic field ($\Delta B/B$), the angle between the magnetic field and the shock normal (θ_{Bn}) and the Mach number.

Spacecraft	Shock	Date	Time (h)	$\Delta B(nT)$	$\Delta B/B$	θ°_{Bn}	Mach No.
VEX	A	30 July 2007	14.54	0.51	0.07	5	1.04
VEX	B	30 July 2007	15.51	0.38	0.04	28	1.02
VEX	C	30 July 2007	18.00	0.71	0.05	36	1.04
VEX	D	30 July 2007	18.91	0.72	0.05	87	1.05
VEX	E	30 July 2007	19.13	0.72	0.05	63	1.04
VEX	F	30 July 2007	19.71	0.82	0.05	49	1.05
ACE	G	31 July 2007	19.00	1.14	0.86	85	1.84
ACE	H	31 July 2007	19.86	1.77	1.13	69	2.04
ACE	I	31 July 2007	20.03	1.29	0.8	55	1.76
ACE	J	31 July 2007	20.11	0.79	0.25	34	1.25

and 49°). In general, the wave activity upstream and downstream of the shocks observed by VEX are insignificant, i.e., shock D shown in Figure 5.7. In contrast, shock C illustrated in Figure 5.8 possesses relatively significant wave activity both upstream and downstream of the shock.

On the other hand, the four shocks observed by ACE are rather different from those observed by VEX. The shocks observed by ACE are relatively stronger with larger values of $\Delta B/B$ (0.86, 1.13, 0.80, and 0.25), field jump ΔB (1.14, 1.77, 1.29, and 0.79), and Mach number (1.84, 2.04, 1.76, and 1.25) correspondingly . Three of these shocks (shocks G, H, and I given in Table 5.1) are quasi-perpendicular with $\theta_{Bn} > 45°$ (85°, 69° and 55° respectively). Whereas, the final shock (shock J) observed by ACE is quasi-parallel with $\theta_{Bn} < 45°$ (34°). In general, the wave activity upstream and downstream of the shocks observed by ACE are insignificant. However, shock H presented in Figure 5.9 possesses relatively significant wave activity downstream of the shock. Also there appears to be a significant structure

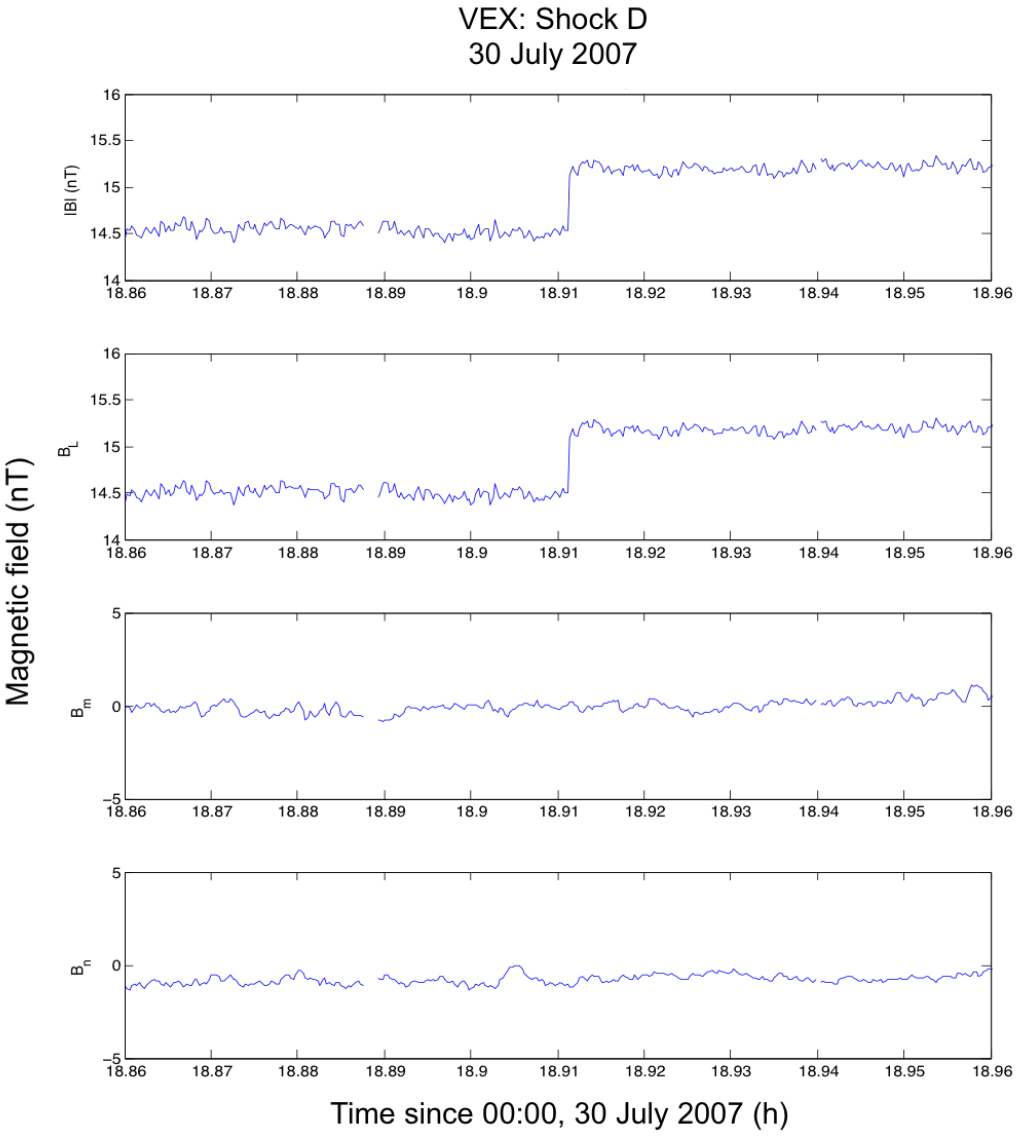

FIGURE 5.7: The magnetic field data associated with shock D that was observed by VEX at 18.91 hours on 30 July 2007. $|B|$, B_L, B_m and B_n are the magnetic field magnitude, the component in the shock plane parallel to the projection of the upstream magnetic field, the component in the plane of the shock perpendicular to the projection of the upstream field and the field component along the shock normal direction respectively.

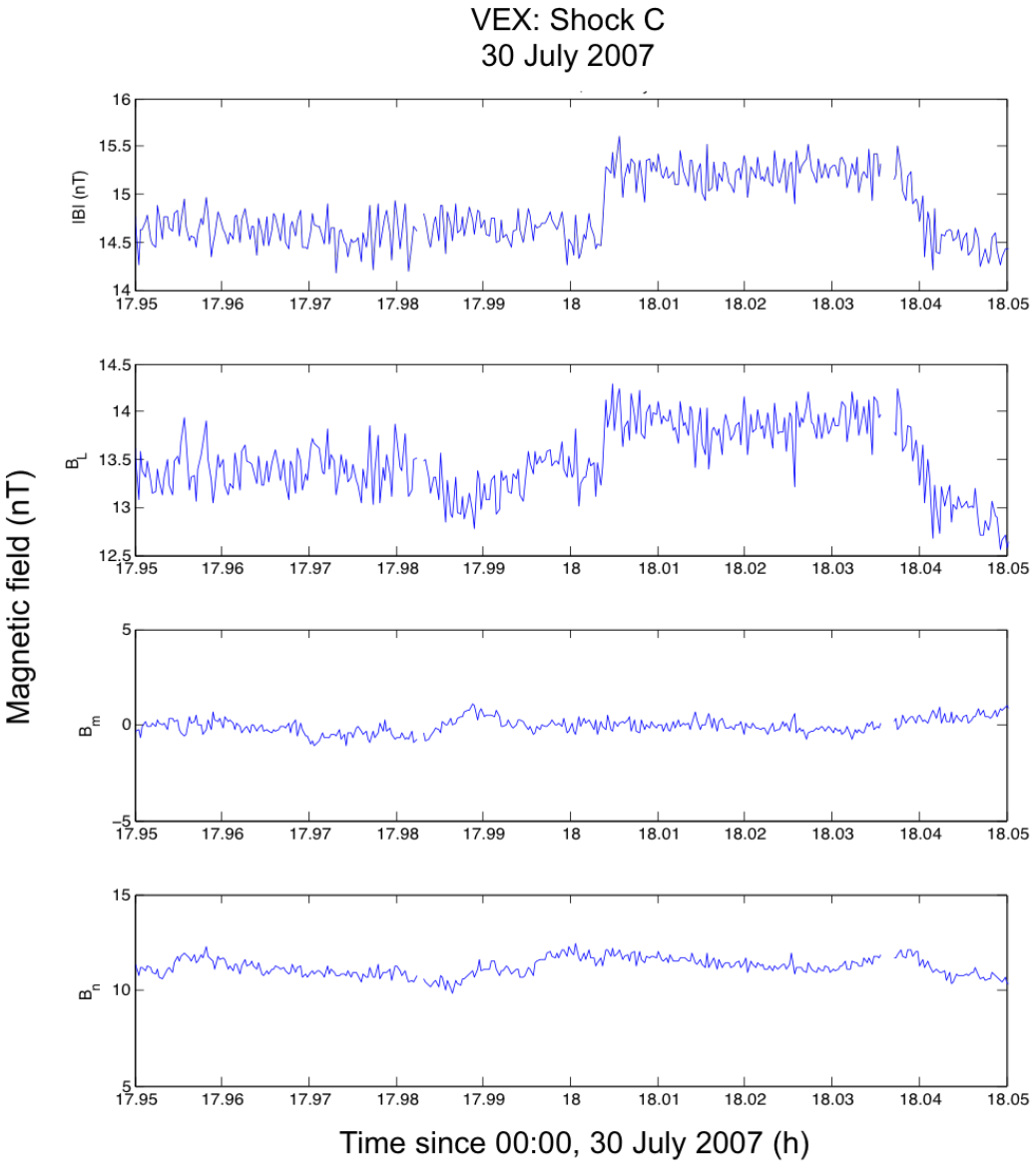

FIGURE 5.8: The magnetic field data associated with shock C that was observed by VEX at 18.00 hours on 30 July 2007. See caption of Figure 5.7 for $|B|$, B_L, B_m and B_n.

at the foot of shock I illustrated in Figure 5.10 that may have formed as a result of collision between two shocks. Other nonlinear structures in the magnetic field measurements observed by VEX and ACE did not fulfil the criteria for a shock crossing. For example, Figure 5.11 illustrates a nonlinear structure observed by ACE at 18.60 hours on 31 July 2007 that did not fulfil the criteria for a shock crossing. In this case, the main magnetic field component (B_L) crosses the zero

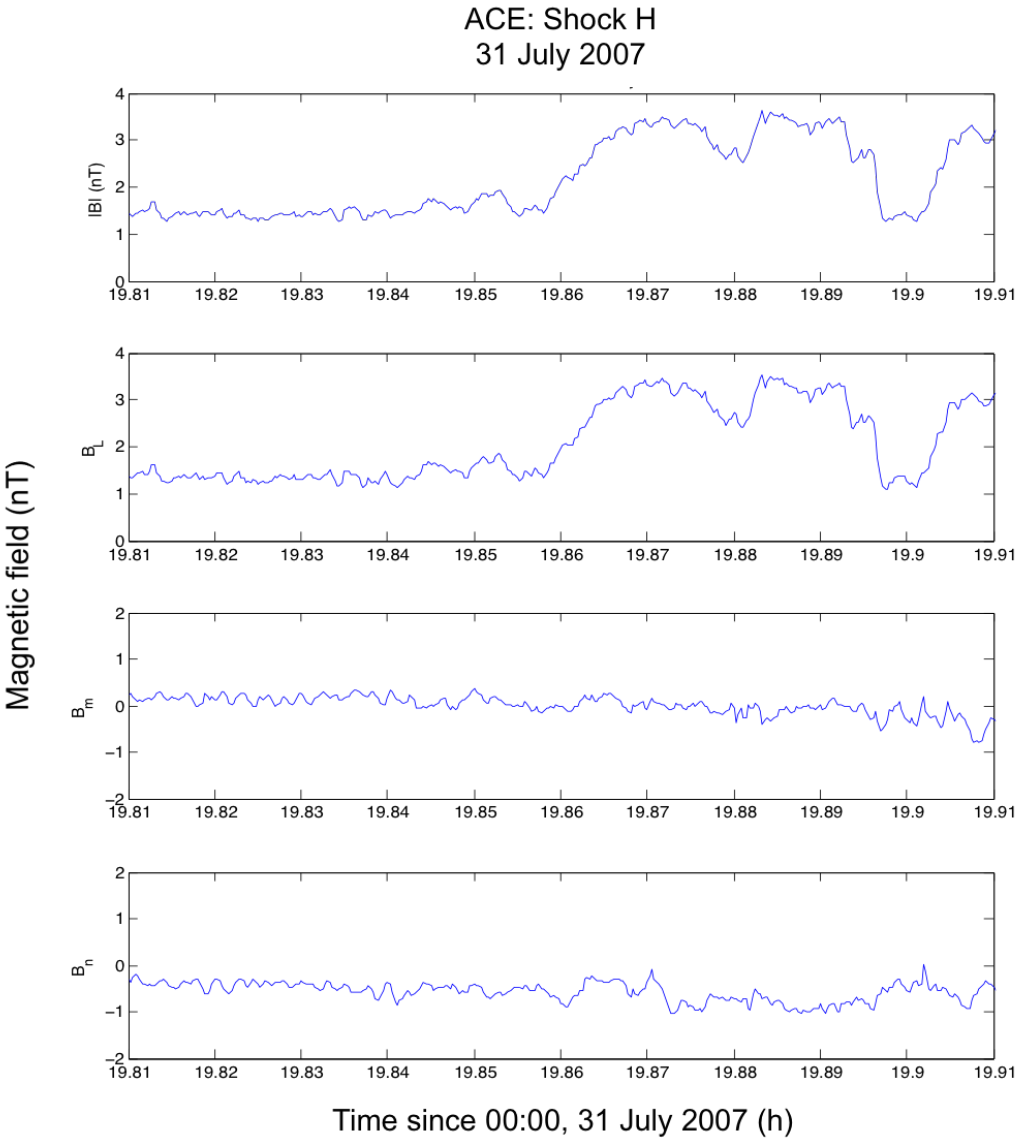

FIGURE 5.9: The magnetic field data associated with shock H that was observed by ACE at 19.86 hours on 31 July 2007. See caption of Figure 5.7 for $|B|$, B_L, B_m and B_n.

axis in the shock coordinate frame.

The observation of fewer but stronger shocks by ACE compared to VEX provides persuasive indication of shock strengthening by coalescence as it was reported by *Russell et al.* [201] for shocks associated with CIRs.

In this study both the coplanarity and minimum variance methods were used to calculate the shock normal, the field component along the normal direction, the

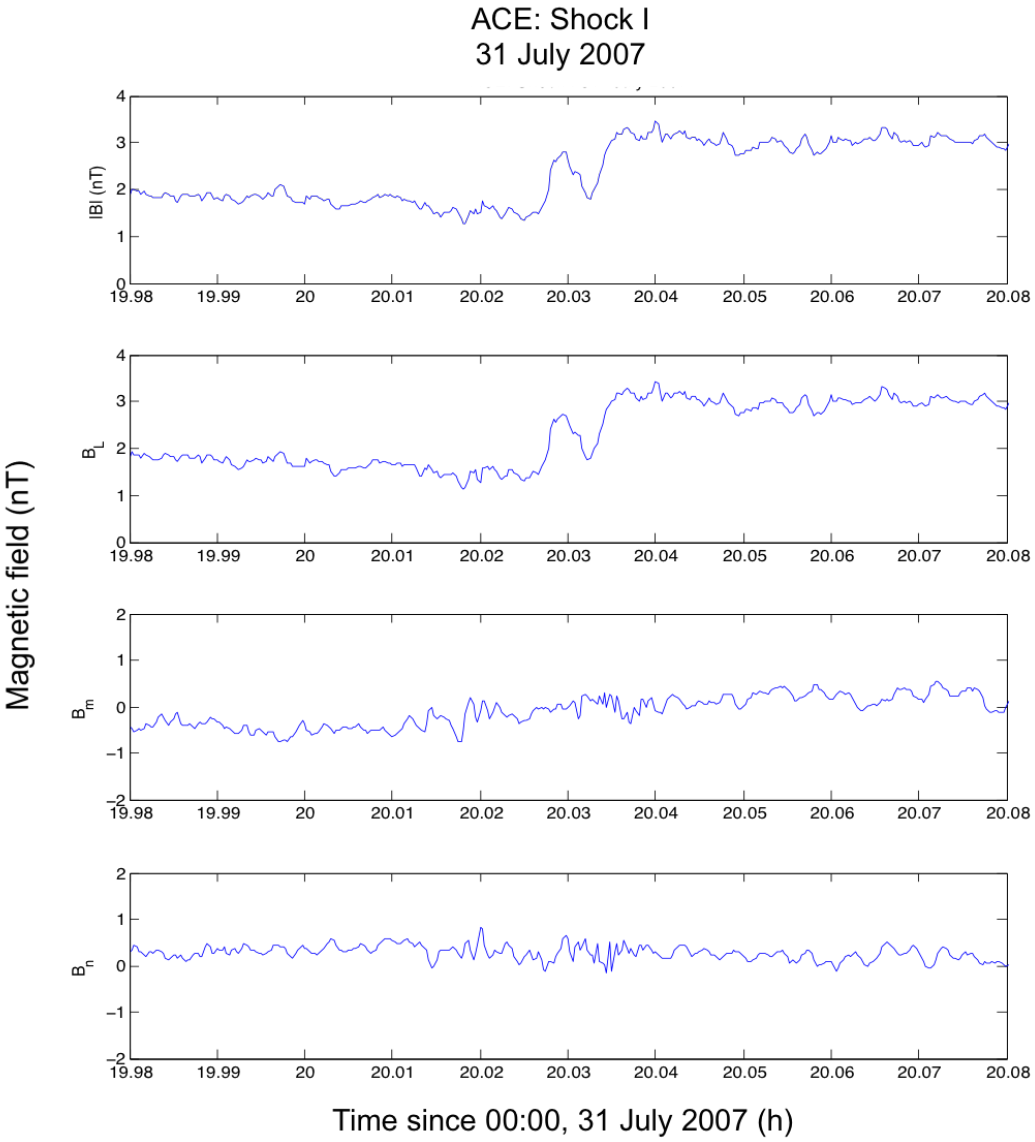

FIGURE 5.10: The magnetic field data associated with shock I that was observed by ACE at 20.03 hours on 31 July 2007. See caption of Figure 5.7 for $|B|$, B_L, B_m and B_n.

component in the shock plane parallel to the projection of the upstream magnetic field, and the component in the plane of the shock perpendicular to the projection of the upstream field. Both methods are frequently used to estimate the shock normal ($\hat{n}$) from single spacecraft magnetic field data. The coplanarity method rely on the assumption that the magnetic field upstream and downstream of the shock is stationary and it satisfies Rankine-Hugoniot relations. The coplanarity method

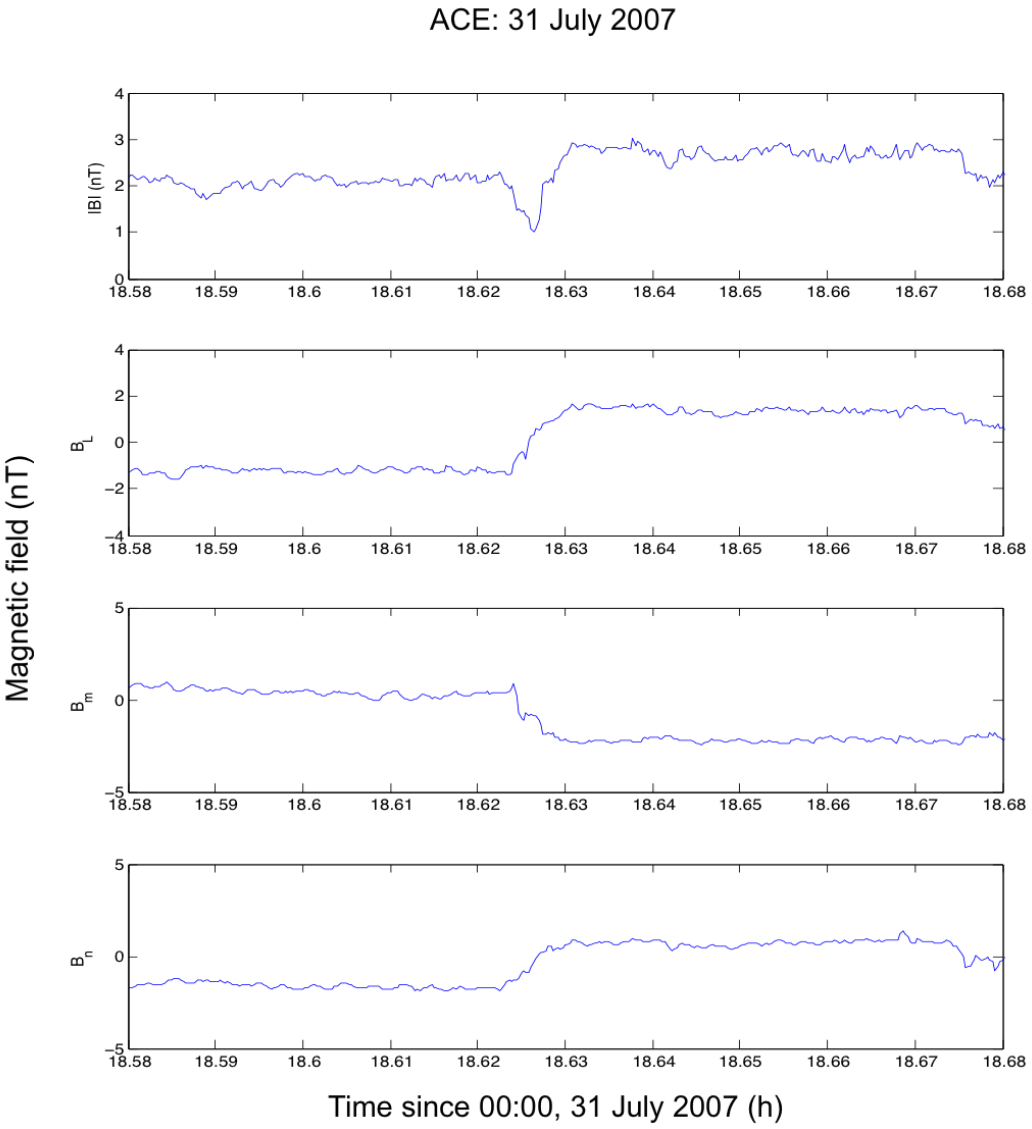

FIGURE 5.11: The magnetic field data associated with a non-linear structure that did not fulfil the shock criteria. This structure was observed by ACE at 20.11 hours on 31 July 2007. In this case, the main magnetic field component (B_L) crosses the zero axis in the shock coordinated frame. See caption of Figure 5.7 for $|B|$, B_L, B_m and B_n.

also insists that the shock normal and the magnetic field upstream and downstream of the shock all lie in the same plane [2, 55, 137]. When these assumptions are true, the shock normal ($\hat{n}$) can be calculated using equation 5.3, where ΔB indicates the jump in magnetic field (i.e., $\Delta B = B_d - B_u$).

$$\hat{n} = \pm \frac{(B_d \times B_u) \times (\Delta B)}{|(B_d \times B_u) \times (\Delta B)|} \tag{5.3}$$

The minimum variance method, originally developed to study the time profiles of magnetometer data at the magnetopause [224], also depend on the assumption that the magnetic field upstream and downstream of the shock is stationary [125, 224]. Based on these assumptions, the minimum variance (σ) of the normal magnetic field component during shock crossing is given by equation 5.4:

$$\sigma^2 = \frac{1}{K} \sum_{i=1}^{K} [B^i \cdot \hat{n} - \overline{B} \cdot \hat{n}]^2 \tag{5.4}$$

where K represents the number of magnetic field measurements and $\overline{B}$ is the average of the K field measurements used in the calculations (equation 5.5):

$$\bar{B} = \frac{1}{K} \sum_{i=1}^{K} B^i \tag{5.5}$$

The minimisation of equation 5.4 corresponds to the smallest eigenvalue of the covariant matrix:

$$M_{\alpha\beta} = (\overline{B_\alpha B_\beta} - \overline{B_\alpha}\ \overline{B_\beta}) \qquad \alpha, \beta = 1, 2, 3 \tag{5.6}$$

where $\overline{B_\alpha}$ and $\overline{B_\beta}$ are the average Cartesian components of field vectors. The normal vector is then equivalent to the smallest eigenvector of the covariant matrix given in equation 5.6 [224].

The Mach number was estimated using Formula 5.7, the same formula as of *Balikhin et al.* [26] where **M** represents Mach number, B_d and B_u are upstream and downstream magnetic field measurements respectively. The magnetic geometry of the shock is described by the angle between the magnetic field and the shock normal (θ_{Bn}).

$$\mathbf{M} - 1 \approx (\frac{B_d}{B_u} - 1) sin^2\theta_{Bn} \tag{5.7}$$

The ENLIL simulations revealed that the trailing CME arrived at VEX, as displayed in Figure 5.12, at approximately 02 : 00 on 1 July 2007 when the VEX spacecraft was within the Venusian bow shock. Hence, during this period there is a significant gap in the clean magnetic field data recorded by VEX. Consequently, the identification of CME associated shock crossings during this data gap was not possible. For this reason the trailing CME was not studied further.

For validation purposes, the magnetic field data measurements recorded by WIND were also analysed during the leading CME crossing on 31 July 2007. It was found that WIND, similar to ACE, also observed a total of four relatively strong shocks

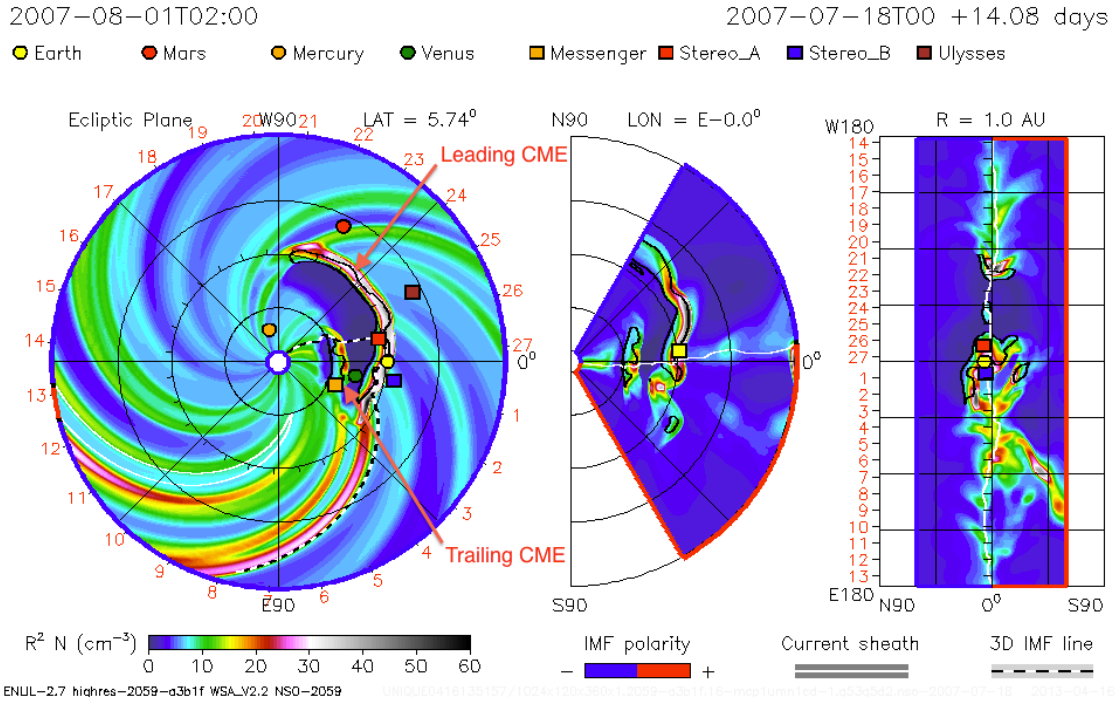

FIGURE 5.12: A snapshot of the CCMC's ENLIL with a cone model simulation at 02 : 00 on 1 August 2007. The trailing CME is at the Venusian orbit, while the leading CME is passing the Earth orbit. The structures of the CMEs are clear through density variations. The estimated arrival time of the trailing halo CME at Venus is approximately 02 : 00 on 1 August 2007. The red arrows point to the leading and trailing CMEs.

associated with the leading CME. This reiterates that stronger shocks may have formed as a result of coalescence of weaker shocks.

5.3.4 Discussions and Conclusions

In this study it was found that there were a total of six shocks observed by VEX and only four but stronger shocks observed by ACE associated with the crossing of a partial halo CME on 30 July 2007 at the Venusian orbit and a day later at the Earth orbit . This indicates that the shocks observed at ACE may have strengthened by coalescence of weaker shocks observed earlier at VEX, and more importantly the formation of stronger shocks resulting from this coalescence takes place between Venus and the Earth.

It is the balance of nonlinear steepening and some counterbalancing processes such as dispersion and resistivity that leads to the formation of shocks. The majority of subcritical shocks observed in the vicinity of the Earth are fast magnetosonic dispersive shocks. These shocks are formed when the dispersion of fast magnetosonic waves counterbalances the nonlinear steepening [127]. The steepening of the nonlinear structure can be analytically described as the transfer of energy to the shorter scales. If the MHD approximation is valid then the waves on these new shorter scales will propagate with the same speed as the initial wave due to the non-dispersive characteristics of the MHD waves. Continuous steepening will pump more energy into these scales leading to an increase in the amplitude of the corresponding waves, and at some stage the latter waves will also become subjected to nonlinear steepening where the energy will be transferred into even shorter scales and so on. Eventually, this cascade will stop at extremely short scales where the MHD approximation will be invalid for their description. At this point it would be necessary to use the two fluid MHD model.

The small-amplitude waves described by two fluid MHD are dispersive [127], i.e their phase velocity depends on the spatial scale. Waves with short scale will either propagate upstream relative to the front and form a wave precursor in case of quasi-perpendicular geometry or in almost perpendicular case when $cos(\theta_{Bn}) < \sqrt{\mu}$ they will be convected downstream and form wave train. Here μ is the ratio of electron and ion masses. The spatial scales of such fast magnetosonic shocks are determined by the whistler dispersion scale $cos(\theta_{Bn})(c/\omega_{pi})$, where ω_{pi} is the ion plasma frequency [130]. As the nonlinear structures associated with the CME steepens, the time when they reach local whistler dispersive scale depends upon the local plasma parameters that vary due to the non-uniformity of the CME

itself. At that stage, local dispersive shocks will be formed in various locations. Generally, the propagation velocity of these shocks should differ as the plasma parameters are not uniform, leading to the coalescence in at least some of them. Such shocks can be effective accelerators of ions due to multiple reflections from their colliding fronts. This process of multiple shock formation is beyond the classical MHD approach, as the MHD does not account for wave dispersion.

This work can be extended to include CME associated shocks during solar wind conjunction periods between VEX and other spacecrafts near the Earth orbit such as the STEREO (Solar TErrestrial RElations Observatory) satellites. In this case, more CME associated shocks can be studied in order to understand further the formation of stronger shocks resulting from the coalescence of weaker shocks between the orbits of Venus and the Earth.

5.3.5 Acknowledgements

The simulation results have been provided by the Community Coordinated Modelling Center at Goddard Space Flight Center through their public Runs on Request system (http://ccmc.gsfc.nasa.gov). The CCMC is a multi-agency partnership between NASA, AFMC, AFOSR, AFRL, AFWA, NOAA, NSF and ONR. The ENLIL with Cone Model Model was developed by the D. Odstrcil at the University of Colorado at Boulder. I would like to acknowledge discussions with C. T. Russell, A. P. Dimmock, S. N. Walker and S. A. Pope.

5.4 Summary

Collisionless shocks occur ubiquitously throughout the universe. Most importantly, collisionless shocks are formed when solar wind interacts with propagating CMEs. Ions accelerated at these shocks contribute to the solar energetic protons observed in the vicinity of the Earth. Recently a joint analysis of Venus Express (VEX) and STEREO data by *Russell et al.* [201] have shown that the formation of strong shocks associated with CIRs takes place between the orbits of Venus and the Earth as a result of coalescence of weaker shocks formed earlier. The present study used VEX and ACE data in order to analyse shocks associated with CMEs that erupted on 29 and 30 of July 2007 during the solar wind conjunction period between Venus and the Earth. For these particular cases it was shown that the above scenario of shock formation proposed for CIRs also takes place for CMEs. Contradiction with shock formation resulting from MHD modelling is explained by inability of classical MHD to account for the role of wave dispersion in the formation of the shock. The results have been published in the peer-reviewed international journal of Annales Geophysicae, in March 2014 (*Aryan, H., Balikhin, M. A., Taktakishvili, A., and Zhang, T. L. (2014), Observation of shocks associated with CMEs in 2007. Ann. Geophys., 3, 223-230, doi: 0.5194/angeo-32-223-2014*).

Chapter 6

Conclusions

6.1 Summary and Conclusions

Energetic charged particles in near Earth geospace pose serious hazard to the electronic components of satellites. The energetic electrons can severely damage or even destroy electronic systems [12, 19, 34, 68, 69, 91]. This may cause satellite malfunction or even lead to the loss of the satellite, which can be very disruptive and extremely expensive. The severity of the hazard is determined by the level of energetic electron flux [14, 17]. The flux of relativistic electrons at the outer radiation belt can change by several orders of magnitude during storms and other disturbances. Satellite operators and manufacturers rely on accurate forecasts of these near Earth geospace environment in order to prevent catastrophic damages during severe conditions. Despite decades of research, particle acceleration in near Earth geospace is not yet fully understood. This thesis has increased the understanding of particle acceleration in near Earth geospace through studying the relationship between solar wind parameters and energetic electron fluxes at

the outer radiation belt, the study of naturally occurring electromagnetic waves and their crucial role in the acceleration and loss of energetic electrons in the inner magnetosphere, and the study of particle acceleration in the vicinity of the Earth and interplanetary medium by strong interplanetary collisionless shocks associated with Coronal Mass Ejections, in particular, in the case of strong collisionless shock formation associated with shock coalescence.

Precise knowledge of the relationship between solar wind parameters and relativistic electron fluxes at the outer radiation belt can help improve forecasting and nowcasting of changes in energetic electron population and ultimately help mitigate the damage caused to the satellites and other space based systems [12] operating at geostationary orbit. The correlation between solar wind velocity and energetic electron fluxes was previously reported to have a triangle shape with a distinct velocity dependent lower limit, but a velocity independent upper limit. It was shown that the flux of energetic electron increased with solar wind velocity until a saturation velocity was reached. Beyond the saturation velocity an increase in solar wind velocity was statistically not accompanied with energetic electron flux enhancement. This thesis demonstrated that the saturation velocity was dependent on solar wind density, whereby the saturation velocity decreased as the solar wind density increased. This improved knowledge can be used to model and forecast fluxes of high energy electrons in the outer terrestrial radiation belt more accurately. Subsequently, the forecasts will be more reliable and the satellite operators would be able to use the information to mitigate damage to their satellites.

In addition, naturally occurring electromagnetic waves, such as plasmaspheric hiss

and chorus waves, play a crucial role in the acceleration and loss of energetic electrons in near Earth geospace that ultimately change the dynamics of the radiation belts [139, 141, 143, 167, 169, 236, 240]. The distribution of these waves in the inner magnetosphere is commonly presented under different values of geomagnetic activity as expressed by the geomagnetic indices [4, 139, 141, 168, 169], despite the fact that not all geomagnetic storms necessarily change relativistic electron fluxes in the outer radiation belt and the fact that geomagnetic indices are indirect and nonspecific parameters [18, 247] that lack time history information. This thesis presented wave distributions not only as a function of geomagnetic activity, but also as a function of directly measured solar wind parameters (velocity, density, pressure, and IMF) that are known to be predominantly effective in the control of radiation belt energetic electron fluxes [184, 194, 195, 251]. The new wave models can benefit studies of the evolution of energetic electron fluxes that rely heavily on the numerical codes in order to model energy and pitch angle diffusion due to electron interaction with plasma waves in the frame of quasi-linear approximation. The new wave models can also be used to improve forecasting and nowcasting of energetic electrons in the inner magnetosphere.

Energetic particles in the vicinity of the Earth and the interplanetary medium are accelerated by interplanetary collisionless shock waves mainly associated with Coronal Mass Ejections and Co-rotating Interactive Regions. This thesis revealed that collisionless shocks, associated with CMEs, coalescence between the orbits of Venus and the Earth in order to form stronger shocks. Such shocks can be effective accelerators of ions due to multiple reflections from their colliding fronts. This improved our knowledge of shock formation and coalescence.

6.2 Future Work

Although, the work presented in this thesis improved our knowledge of particle acceleration in near Earth geospace, there is the potential for future studies. The work presented in Chapter 3 was based on one day averages of electron fluxes measured in the energy range $1.8 - 3.5$ MeV and solar wind densities less than 6.0cm^{-3}. The relationship between the saturation velocity and solar wind density for electron fluxes measured in other energy ranges and for solar wind densities larger than 6 cm^{-3} is highly beneficial for modelling and forecasting of fluxes of high energy electrons. Hence, this work can be extended to other energy levels and solar wind densities larger than 6 cm^{-3}.

Additionally, the wave modes developed in Chapter 4 to present chorus wave distributions in the inner magnetosphere as functions of geomagnetic activity and solar wind parameters can be extended to include plasmaspheric hiss waves. Plasmaspheric hiss is an important class of electromagnetic wave that play a crucial role in the dynamics of the radiation belts [38, 39, 237]. Plasmaspheric hiss is not only responsible for the formation of the slot region [1, 156, 157], but it is also responsible for the decay of energetic electrons in the outer radiation belt during relatively quiet times [232] due to resonant pitch angle scattering of energetic electrons [157]. Evidence suggest that there is a strong link between chorus and plasmaspheric waves.

Finally, Chapter 5 revealed that collisionless shocks, associated with CMEs, coalescence between the orbits of Venus and the Earth in order to form stronger shocks. The study was based on magnetic data measurements from VEX and ACE spacecraft's. This work can be extended to include data measurements from

other satellites within the Venusian and Earth orbits. Also, it would be highly beneficial to study the formation of these collisionless shocks nearer to the Sun before their arrival at the Venusian orbit and study their propagation beyond the orbit of the Earth.

References

[1] Abel, B., and R. M. Thorne (1998), Electron scattering loss in Earth's inner magnetosphere 1. Dominant physical processes, , *103*, 2385–2396, doi:10.1029/97JA02919.

[2] Abraham-Shrauner, B. (1972), Determination of magnetohydrodynamic shock normals, , *77*, 736, doi:10.1029/JA077i004p00736.

[3] Agapitov, O., V. Krasnoselskikh, Y. V. Khotyaintsev, and G. Rolland (2012), Correction to: A statistical study of the propagation characteristics of whistler waves observed by Cluster, , *39*, L24102, doi:10.1029/2012GL054320.

[4] Agapitov, O., A. Artemyev, V. Krasnoselskikh, Y. V. Khotyaintsev, D. Mourenas, H. Breuillard, M. Balikhin, and G. Rolland (2013), Statistics of whistler mode waves in the outer radiation belt: Cluster STAFF-SA measurements, *Journal of Geophysical Research (Space Physics)*, *118*, 3407–3420, doi:10.1002/jgra.50312.

[5] Akasofu, S.-I., P. D. Perreault, F. Yasuhara, and C.-I. Meng (1973), Auroral substorms and the interplanetary magnetic field, , *78*, 7490, doi:10.1029/JA078i031p07490.

[6] Albert, J. M. (2003), Evaluation of quasi-linear diffusion coefficients for EMIC waves in a multispecies plasma, *J. Geophys. Res.*, *108*(A6), 1249, doi:10.1029/2002JA009792.

[7] Albert, J. M. (2005), Evaluation of quasi-linear diffusion coefficients for whistler mode waves in a plasma with arbitrary density ratio, *J. Geophys. Res.*, *110*(A3), A03,218, doi:10.1029/2004JA010844.

[8] Artemyev, A. V., O. V. Agapitov, D. Mourenas, V. Krasnoselskikh, and L. M. Zelenyi (2013), Storm-induced energization of radiation belt electrons: Effect of wave obliquity, , *40*, 4138–4143, doi:10.1002/grl.50837.

[9] Aryan, H., R. J. Boynton, and S. N. Walker (2013), Analysis of trends between solar wind velocity and energetic electron fluxes at geostationary orbit using the reverse arrangement test, *Journal of Geophysical Research (Space Physics)*, *118*, 636–641, doi:10.1029/2012JA018216.

[10] Axford, W. I., and C. O. Hines (1961), A unifying theory of high-latitude geophysical phenomena and geomagnetic storms, *Canadian Journal of Physics*, *39*, 1433, doi:10.1139/p61-172.

[11] Baker, D. N. (1986), Substorms in the earth's magnetosphere, in *Magnetospheric Phenomena in Astrophysics*, *American Institute of Physics Conference Series*, vol. 144, edited by R. I. Epstein and W. C. Feldman, pp. 184–207, doi:10.1063/1.35655.

[12] Baker, D. N. (1996), Solar wind-magnetosphere drivers of space weather., *Journal of Atmospheric and Terrestrial Physics*, *58*, 1509–1526.

[13] Baker, D. N. (2000), The occurrence of operational anomalies in spacecraft and their relationship to space weather, *IEEE Transactions on Plasma Science*, *28*, 2007–2016, doi:10.1109/27.902228.

[14] Baker, D. N. (2002), How to cope with space weather, *Science*, *297*, 5586, doi:10.1126/science.1074956.

[15] Baker, D. N., and S. G. Kanekal (2008), Solar cycle changes, geomagnetic variations, and energetic particle properties in the inner magnetosphere, *Journal of Atmospheric and Solar-Terrestrial Physics*, *70*, 195–206, doi: 10.1016/j.jastp.2007.08.031.

[16] Baker, D. N., and S. G. Kanekal (2008), Solar cycle changes, geomagnetic variations, and energetic particle properties in the inner magnetosphere, *Journal of Atmospheric and Solar-Terrestrial Physics*, *70*, 195–206, doi: 10.1016/j.jastp.2007.08.031.

[17] Baker, D. N., R. D. Belian, P. R. Higbie, R. W. Klebesadel, and J. Blake (1987), Deep dielectric charging effects due to high-energy electrons in earths outer magnetospherec, *J. Electrost*, *20*(1), doi:10.1016/0304-3886(87) 90082-9.

[18] Baker, D. N., R. L. McPherron, T. E. Cayton, and R. W. Klebesadel (1990), Linear prediction filter analysis of relativistic electron properties at 6.6 R(E), , *95*, 15,133–15,140, doi:10.1029/JA095iA09p15133.

[19] Baker, D. N., J. B. Blake, L. B. Callis, J. R. Cummings, D. Hovestadt, S. Kanekal, B. Klecker, R. A. Mewaldt, and R. D. Zwickl (1994), Relativistic electron acceleration and decay time scales in the inner and outer radiation belts: SAMPEX, *Geophys. Res. Lett.*, *21*(6), doi:10.1029/93GL03532.

[20] Baker, D. N., et al. (1998), Coronal mass ejections, magnetic clouds, and relativistic magnetospheric electron events:, *J. Geophys. Res.*, *103*(A8), doi: 10.1029/97JA03329.

[21] Baker, D. N., et al. (1998), A strong CME-related magnetic cloud interaction with the Earth's Magnetosphere: ISTP observations of rapid relativistic electron acceleration on May 15, 1997, , *25*, 2975–2978, doi:10.1029/98GL01134.

[22] Baker, D. N., S. G. Kanekal, X. Li, S. P. Monk, J. Goldstein, and J. L. Burch (2004), An extreme distortion of the Van Allen belt arising from the 'Hallowe'en' solar storm in 2003, , *432*, 878–881, doi:10.1038/nature03116.

[23] Baker, D. N., et al. (2013), A long-lived relativistic electron storage ring embedded in earths outer van allen belt, *Science*, *340*, 186–190, doi:10.1126/science.1233518.

[24] Baker, D. N., et al. (2014), Gradual diffusion and punctuated phase space density enhancements of highly relativistic electrons: Van allen probes observations, *Geophysical Research Letters*, *41*(5), 1351–1358, doi:10.1002/2013GL058942.

[25] Balikhin, M. A., I. Bates, and S. Walker (2001), Identification of linear and nonlinear processes in space plasma turbulence data, *Advances in Space Research*, *28*, 787–800, doi:10.1016/S0273-1177(01)00515-4.

[26] Balikhin, M. A., T. L. Zhang, M. Gedalin, N. Y. Ganushkina, and S. A. Pope (2008), Venus Express observes a new type of shock with pure kinematic relaxation, , *35*, L01103, doi:10.1029/2007GL032495.

[27] Balikhin, M. A., R. J. Boynton, S. A. Billings, M. Gedalin, N. Ganushkina, D. Coca, and H. Wei (2010), Data based quest for solar wind-magnetosphere coupling function, , *37*, L24107, doi:10.1029/2010GL045733.

[28] Balikhin, M. A., R. J. Boynton, S. Walker, J. E. Borovsky, S. A. Billings, and H. L. Wei (2011), Using the NARMAX approach to model the evolution of energetic electrons fluxes at geostationary orbit, *Geophys. Res. Lett.*, *38*(18), doi:10.1029/2011GL048980.

[29] Barnes, C. W., and J. A. Simpson (1976), Evidence for interplanetary acceleration of nucleons in corotating interaction regions, , *210*, L91–L96, doi: 10.1086/182311.

[30] Bartels, J., N. H. Heck, and H. F. Johnston (1939), The three-hour-range index measuring geomagnetic activity, *Terrestrial Magnetism and Atmospheric Electricity (Journal of Geophysical Research)*, *44*, 411, doi: 10.1029/TE044i004p00411.

[31] Beck, T. W., T. J. Housh, J. P. Weir, J. T. Cramer, V. Vardaxis, G. O. Johnson, J. W. Coburn, M. H. Malek, and M. Mielke (2006), An examination of the runs test, reverse arrangements test, and modified reverse arrangements test for assessing surface EMG signal stationarity, *J. Neuroscience Methods*, *156*(1-2), doi:10.1016/j.jneumeth.2006.03.011.

[32] Bendat, J. S., and A. G. Piersol (2000), Random data analysis and measurement procedures, in *Random Data Analysis and Measurement Procedures*, vol. Third Edition, pp. 96 – 99, Wiley-Interscience, doi:10.1088/0957-0233/11/12/702.

[33] Billings, S. A., M. Korenberg, and S. Chen (1989), Identification of non-linear output?affine systems using an orthogonal least?squares algorithm, *International Journal of Control*, *49*, 21572189.

[34] Blake, J. B., M. S. Gussenhoven, E. G. Mullen, and R. W. Fillius (1992), Identification of an unexpected space radiation hazard, *IEEE Transactions on Nuclear Science*, *39*, 1761–1764, doi:10.1109/23.211364.

[35] Blake, J. B., D. N. Baker, N. Tumer, K. W. Ogilvie, and R. P. Leppings (1997), Correlation of changes in the outer zone relativistic electron population with upstream solar wind and magnetic field measurements, *Geophys. Res. Lett.*, *24*(8), doi:10.1029/97GL00859.

[36] Boaghe, O. M., M. A. Balikhin, S. A. Billings, and H. Alleyne (2001), Identification of nonlinear processes in the magnetospheric dynamics and forecasting of Dst index, *J. Geophys. Res.*, *106(A12)*, 30,04730,066.

[37] Bortnik, J., and R. M. Thorne (2007), The dual role of ELF/VLF chorus waves in the acceleration and precipitation of radiation belt electrons, *Journal of Atmospheric and Solar-Terrestrial Physics*, *69*, 378–386, doi: 10.1016/j.jastp.2006.05.030.

[38] Bortnik, J., R. M. Thorne, and N. P. Meredith (2008), The unexpected origin of plasmaspheric hiss from discrete chorus emissions, , *452*, 62–66, doi:10.1038/nature06741.

[39] Bortnik, J., W. Li, R. M. Thorne, V. Angelopoulos, C. Cully, J. Bonnell, O. Le Contel, and A. Roux (2009), An Observation Linking the Origin of Plasmaspheric Hiss to Discrete Chorus Emissions, *Science*, *324*, 775–, doi: 10.1126/science.1171273.

[40] Bostrom, C. O., D. S. Beall, and J. C. Armstrong (1970), Time history of the inner radiation zone, October 1963 to December 1968, , *75*, 1246, doi:10.1029/JA075i007p01246.

[41] Bothmer, V., and R. Schwenn (1998), The structure and origin of magnetic clouds in the solar wind, *Annales Geophysicae*, *16*, 1–24, doi:10.1007/s00585-997-0001-x.

[42] Boynton, R. J., M. A. Balikhin, S. A. Billings, H. L. Wei, and N. Ganushkina (2011), Using the NARMAX OLS-ERR algorithm to obtain the most influential coupling functions that affect the evolution of the magnetosphere, *J. Geophys. Res.*, *116*(A5), A05,218.

[43] Boynton, R. J., M. A. Balikhin, S. A. Billings, A. S. Sharma, and O. A. Amariutei (2011), Data derived NARMAX Dst model, *Annales Geophysicae*, *29*(6), 965–971, doi:10.5194/angeo-29-965-2011.

[44] Boynton, R. J., M. A. Balikhin, S. A. Billings, G. D. Reeves, N. Ganushkina, M. Gedalin, O. A. Amariutei, J. E. Borovsky, and S. N. Walker (2013), The analysis of electron fluxes at geosynchronous orbit employing a NARMAX approach, *Journal of Geophysical Research (Space Physics)*, *118*, 1500–1513, doi:10.1002/jgra.50192.

[45] Burkepile, J. T., A. J. Hundhausen, A. L. Stanger, O. C. St. Cyr, and J. A. Seiden (2004), Role of projection effects on solar coronal mass ejection properties: 1. A study of CMEs associated with limb activity, *Journal of Geophysical Research (Space Physics)*, *109*, A03103, doi:10.1029/2003JA010149.

[46] Burtis, W. J., and R. A. Helliwell (1969), Banded chorus - A new type of VLF radiation observed in the magnetosphere by OGO 1 and OGO 3, , *74*, 3002, doi:10.1029/JA074i011p03002.

[47] Carpenter, D. L. (1963), Whistler Evidence of a 'Knee' in the Magnetospheric Ionization Density Profile, , *68*, 1675–1682, doi:10.1029/JZ068i006p01675.

[48] Carrington, R. C. (1859), Description of a Singular Appearance seen in the Sun on September 1, 1859, , *20*, 13–15.

[49] Carrington, R. C. (1863), Observations of spots on the sun, in *Observations of Spots on the Sun*, Williams andNorgate., London.

[50] Chan, K.-W., and R. E. Holzer (1976), ELF hiss associated with plasma density enhancements in the outer magnetosphere, , *81*, 2267–2274, doi:10.1029/JA081i013p02267.

[51] Chao, J. K., and S. Olbert (1970), Observation of slow shocks in interplanetary space, , *75*, 6394, doi:10.1029/JA075i031p06394.

[52] Chapman, S., and V. C. A. Ferraro (1931), A new theory of magnetic storms, *Terrestrial Magnetism and Atmospheric Electricity (Journal of Geophysical Research)*, *36*, 171, doi:10.1029/TE036i003p00171.

[53] Chapman, S., and V. C. A. Ferraro (1931), A new theory of magnetic storms, *Terrestrial Magnetism and Atmospheric Electricity (Journal of Geophysical Research)*, *36*, 77, doi:10.1029/TE036i002p00077.

[54] Cladis, J. B., L. F. Chase, Jr., W. L. Imhof, and D. J. Knecht (1961), Energy Spectrum and Angular Distributions of Electrons Trapped in the Geomagnetic Field, , *66*, 2297–2312, doi:10.1029/JZ066i008p02297.

[55] Colburn, D. S., and C. P. Sonett (1966), Discontinuities in the Solar Wind, , *5*, 439–506, doi:10.1007/BF00240575.

[56] Cornilleau-Wehrlin, N., et al. (2005), The STAFF-DWP wave instrument on the DSP equatorial spacecraft: description and first results, *Annales Geophysicae*, *23*, 2785–2801, doi:10.5194/angeo-23-2785-2005.

[57] Craven, J. D. (1966), Temporal variations of electron intensities at low altitudes in the outer radiation zone as observed with satellite Injun 3, , *71*, 5643–5663, doi:10.1029/JZ071i023p05643.

[58] Darrouzet, F., V. Pierrard, S. Benck, G. Lointier, J. Cabrera, K. Borremans, N. Y. Ganushkina, and J. D. Keyser (2013), Links between the plasmapause and the radiation belt boundaries as observed by the instruments CIS, RAPID, and WHISPER onboard Cluster, *Journal of Geophysical Research (Space Physics)*, *118*, 4176–4188, doi:10.1002/jgra.50239.

[59] Davis, T. N., and M. Sugiura (1966), Auroral electrojet activity index AE and its universal time variations, , *71*, 785–801, doi:10.1029/JZ071i003p00785.

[60] Dmitriev, A. V., N. B. Crosby, and J.-K. Chao (2005), Interplanetary sources of space weather disturbances in 1997 to 2000, *Space Weather*, *3*, S03001, doi:10.1029/2004SW000104.

[61] Elkington, S. R., M. K. Hudson, and A. A. Chan (1999), Acceleration of relativistic electrons via drift-resonant interaction with toroidal-mode Pc-5 ULF oscillations, *Geophys. Res. Lett.*, *26*(21), 3273–3276.

[62] Elkington, S. R., M. K. Hudson, and A. A. Chan (2003), Resonant acceleration and diffusion of outer zone electrons in an asymmetric geomagnetic field, *Journal of Geophysical Research (Space Physics)*, *108*, 1116, doi:10.1029/2001JA009202.

[63] Elliott, H. A., J.-M. Jahn, and D. J. McComas (2013), The Kp index and solar wind speed relationship: Insights for improving space weather forecasts, *Space Weather*, *11*, 339–349, doi:10.1002/swe.20053.

[64] Falkenberg, T. V., B. Vrsnak, A. Taktakishvili, D. Odstrcil, P. MacNeice, and M. Hesse (2010), Investigations of the sensitivity of a coronal mass ejection model (ENLIL) to solar input parameters, *Space Weather*, *8*(6), doi:10.1029/2009SW000555.

[65] Farris, M. H., C. T. Russell, and M. F. Thomsen (1993), Magnetic structure of the low beta, quasi-perpendicular shock, , *98*, 15,285, doi:10.1029/93JA00958.

[66] Farthing, W. H., J. P. Brown, and W. C. Bryant (1982), Differential spacecraft charging on the geostationary operational environmental satellites, *NASA STI/Recon Technical Report N*, *82*, 26,356.

[67] Feldman, W. C., J. R. Asbridge, S. J. Bame, E. E. Fenimore, and J. T. Gosling (1981), The solar origins of solar wind interstream flows - Near-equatorial coronal streamers, , *86*, 5408–5416, doi:10.1029/JA086iA07p05408.

[68] Fennell, J. F., H. C. Koons, J. L. Roeder, and J. B. Blake (2001), Spacecraft Charging: Observations and Relationship to Satellite Anomalies, in *Spacecraft Charging Technology, ESA Special Publication*, vol. 476, edited by R. A. Harris, p. 279.

[69] Feynman, J., and S. B. Gabriel (2000), On space weather consequences and predictions, , *105*, 10,543–10,564, doi:10.1029/1999JA000141.

[70] Feynman, J., and A. J. Hundhausen (1994), Coronal mass ejections and major solar flares: The great active center of March 1989, , *99*, 8451–8464, doi:10.1029/94JA00202.

[71] Fisk, L. A., and M. A. Lee (1980), Shock acceleration of energetic particles in corotating interaction regions in the solar wind, , *237*, 620–626, doi:10.1086/157907.

[72] Fok, M. C., and T. E. Moore (1997), Ring current modeling in a realistic magnetic field configuration, *Geophys. Res. Lett.*, *24*(14), 1775–1778, doi:10.1029/97GL01255.

[73] Fok, M. C., R. A. Wolf, R. W. Spiro, and T. E. Moore (2001), Comprehensive computational model of earth's ring current, *J. Geophys. Res.*, *106*(A5), 8417–8424, doi:10.1029/2000JA000235.

[74] Frank, L. A. (1965), Inward Radial Diffusion of Electrons of Greater than 1.6 Million Electron Volts in the Outer Radiation Zone, , *70*, 3533–3540, doi:10.1029/JZ070i015p03533.

[75] Freeman, J. W., Jr. (1964), The Morphology of the Electron Distribution in the Outer Radiation Zone and near the Magnetospheric Boundary As Observed by Explorer 12, , *69*, 1691–1723, doi:10.1029/JZ069i009p01691.

[76] Ganushkina, N. Y., T. I. Pulkkinen, and T. Fritz (2005), Role of substorm-associated impulsive electric elds in the ring current development during storms, *Annales Geophysicae*, *23*, 579–591, doi:10.5194/angeo-23-579-2005.

[77] Gedalin, M., and M. Balikhin (2004), Electric potential in the low-Mach-number quasi-perpendicular collisionless shock ramp revisited, *Journal of Geophysical Research (Space Physics)*, *109*, A03106, doi:10.1029/2003JA010219.

[78] Gholipour, A., C. Lucas, and B. N. Araabi (2004), Black box modeling of magnetospheric dynamics to forecast geomagnetic activity, *Space Weather*, *2*, S07001, doi:10.1029/2003SW000039.

[79] Gold, T. (1959), Motions in the Magnetosphere of the Earth, , *64*, 1219–1224, doi:10.1029/JZ064i009p01219.

[80] Gopalswamy, N., and B. J. Thompson (2000), Early life of coronal mass ejections, *Journal of Atmospheric and Solar-Terrestrial Physics*, *62*, 1457–1469, doi:10.1016/S1364-6826(00)00079-1.

[81] Gopalswamy, N., S. Akiyama, S. Yashiro, G. Michalek, and R. P. Lepping (2008), Solar sources and geospace consequences of interplanetary magnetic clouds observed during solar cycle 23, *Journal of Atmospheric and Solar-Terrestrial Physics*, *70*, 245–253, doi:10.1016/j.jastp.2007.08.070.

[82] Gosling, J. T. (1996), Corotating and Transient Solar Wind Flows in Three Dimensions, , *34*, 35–74, doi:10.1146/annurev.astro.34.1.35.

[83] Gosling, J. T., and V. J. Pizzo (1999), Formation and Evolution of Corotating Interaction Regions and their Three Dimensional Structure, , *89*, 21–52, doi:10.1023/A:1005291711900.

[84] Gosling, J. T., A. J. Hundhausen, V. Pizzo, and J. R. Asbridge (1972), Compressions and rarefactions in the solar wind: Vela 3, , *77*, 5442, doi: 10.1029/JA077i028p05442.

[85] Gosling, J. T., E. Hildner, R. M. MacQueen, R. H. Munro, A. I. Poland, and C. L. Ross (1976), The speeds of coronal mass ejection events, , *48*, 389–397, doi:10.1007/BF00152004.

[86] Gosling, J. T., J. R. Asbridge, S. J. Bame, W. C. Feldman, G. Borrini, and R. T. Hansen (1981), Coronal streamers in the solar wind at 1 AU, , *86*, 5438–5448, doi:10.1029/JA086iA07p05438.

[87] Gosling, J. T., D. J. McComas, J. L. Phillips, and S. J. Bame (1991), Geomagnetic activity associated with earth passage of interplanetary shock disturbances and coronal mass ejections, , *96*, 7831–7839, doi:10.1029/91JA00316.

[88] Gosling, J. T., S. J. Bame, D. J. McComas, J. L. Phillips, V. J. Pizzo, B. E. Goldstein, and M. Neugebauer (1993), Latitudinal variation of solar wind corotating stream interaction regions: ULYSSES, , *20*, 2789–2792, doi: 10.1029/93GL03116.

[89] Gosling, J. T., D. J. McComas, R. M. Skoug, and R. J. Forsyth (2001), Stream Interaction Regions at High Heliographic Latitudes During Ulysses12/22/2004 6:25PM Second Polar Orbit, , *97*, 189–192, doi: 10.1023/A:1011871421324.

[90] Gringauz, K. I., V. G. Kurt, V. I. Moroz, and I. S. Shklovskii (1960), Results of Observations of Charged Particles Observed Out to R = 100, 000 km, with the Aid of Charged-Particle Traps on Soviet Space Rockets, , *37*, 716.

[91] Gussenhoven, M. S., and E. G. Mullen (1983), Geosynchronous environment for severe spacecraft charging, *Journal of Spacecraft and Rockets*, *20*, 26–34, doi:10.2514/3.28353.

[92] Hamilton, D. C., G. Gloeckler, F. M. Ipavich, B. Wilken, and W. Stuedemann (1988), Ring current development during the great geomagnetic storm of February 1986, , *93*, 14,343–14,355, doi:10.1029/JA093iA12p14343.

[93] Hastings, D. E. (1995), A review of plasma interactions with spacecraft in low Earth orbit, , *100*, 14,457–14,484, doi:10.1029/94JA03358.

[94] Hayakawa, M., and S. S. Sazhin (1992), Mid-latitude and plasmaspheric HISS - A review, , *40*, 1325–1338, doi:10.1016/0032-0633(92)90089-7.

[95] Hayakawa, M., N. Ohmi, M. Parrot, and F. Lefeuvre (1986), Direction finding of ELF hiss emissions in a detached plasma region of the magnetosphere, , *91*, 135–142, doi:10.1029/JA091iA01p00135.

[96] Helliwell, R. A. (1967), A theory of discrete VLF emissions from the magnetosphere, , *72*, 4773–4790, doi:10.1029/JZ072i019p04773.

[97] Hill, T. W. (1979), Generation of the magnetospheric electric field, *Washington DC American Geophysical Union Geophysical Monograph Series*, *21*, 297–315, doi:10.1029/GM021p0297.

[98] Hoffman, R. A., and J. L. Burch (1973), Electron precipitation patterns and substorm morphology, , *78*, 2867–2884, doi:10.1029/JA078i016p02867.

[99] Horne, R. B. (2007), Plasma astrophysics: Acceleration of killer electrons, *Nature Physics*, *3*, 590–591, doi:10.1038/nphys703.

[100] Horne, R. B., and R. M. Thorne (1998), Potential waves for relativistic electron scattering and stochastic acceleration during magnetic storms, , *25*, 3011–3014, doi:10.1029/98GL01002.

[101] Horne, R. B., and R. M. Thorne (2003), Relativistic electron acceleration and precipitation during resonant interactions with whistler-mode chorus, , *30*, 1527, doi:10.1029/2003GL016973.

[102] Horne, R. B., R. M. Thorne, S. A. Glauert, J. M. Albert, N. P. Meredith, and R. R. Anderson (2005), Timescale for radiation belt electron acceleration by whistler mode chorus waves, *J. Geophys. Res.*, *110*(A3), A03,225.

[103] Howard, R. A., N. R. Sheeley, Jr., D. J. Michels, and M. J. Koomen (1985), Coronal mass ejections - 1979-1981, , *90*, 8173–8191, doi:10.1029/JA090iA09p08173.

[104] Hudson, M., S. Elkington, J. Lyon, and C. Goodrich (2000), Increase in relativistic electron flux in the inner magnetosphere: ULF wave mode structure, *Advances in Space Research*, *25*(12), 2327–2337.

[105] Hudson, M. K., S. R. Elkington, J. G. Lyon, C. C. Goodrich, and T. J. Rosenberg (1999), Simulation of radiation belt dynamics driven by solar wind variations, in *Geophys. Monogr. Ser.*, vol. 109, pp. 171–182, AGU, Washington, DC.

[106] Hudson, M. K., S. R. Elkington, J. G. Lyon, M. Wiltberger, and M. Lessard (2001), Radiation belt electron acceleration by ULF wave drift resonance: Simulation of 1997 and 1998 storms, in *Space Weather*, pp. 289–296, Geophys. Monogr.

[107] Hundhausen, A. (1999), Coronal Mass Ejections, in *The many faces of the sun: a summary of the results from NASA's Solar Maximum Mission.*, edited by K. T. Strong, J. L. R. Saba, B. M. Haisch, and J. T. Schmelz, p. 143.

[108] Hundhausen, A. J. (1972), Coronal Expansion and Solar Wind, *Physics and Chemistry in Space*, *5*, doi:10.1007/978-3-642-65414-5.

[109] Hundhausen, A. J. (1985), Some macroscopic properties of shock waves in the heliosphere, *Washington DC American Geophysical Union Geophysical Monograph Series*, *34*, 37–58.

[110] Hundhausen, A. J., C. B. Sawyer, L. House, R. M. E. Illing, and W. J. Wagner (1984), Coronal mass ejections observed during the solar maximum mission - Latitude distribution and rate of occurrence, , *89*, 2639–2646, doi: 10.1029/JA089iA05p02639.

[111] Iucci, N., et al. (2006), Spacecraft operational anomalies and space weather impact hazards, *Advances in Space Research*, *37*, 184–190, doi:10.1016/j.asr. 2005.03.028.

[112] Jian, L., C. T. Russell, J. G. Luhmann, and R. M. Skoug (2006), Properties of Stream Interactions at One AU During 1995 2004, , *239*, 337–392, doi: 10.1007/s11207-006-0132-3.

[113] Jian, L., C. T. Russell, J. G. Luhmann, and R. M. Skoug (2006), Properties of Interplanetary Coronal Mass Ejections at One AU During 1995 2004, , *239*, 393–436, doi:10.1007/s11207-006-0133-2.

[114] Jones, F. C., and D. C. Ellison (1991), The plasma physics of shock acceleration, , *58*, 259–346, doi:10.1007/BF01206003.

[115] Jordanova, V. K., J. U. Kozyra, A. F. Nagy, and G. V. Khazanov (1997), Kinetic model of the ring current-atmosphere interactions, *J. Geophys. Res.*, *102*(A7), 14,279–14,291, doi:10.1029/96JA03699.

[116] Jordanova, V. K., et al. (1998), Effect of wave-particle interactions on ring current evolution for January 10-11, 1997: Initial results, , *25*, 2971–2974, doi:10.1029/98GL00649.

[117] Jordanova, V. K., C. J. Farrugia, R. M. Thorne, G. V. Khazanov, G. D. Reeves, and M. F. Thomsen (2001), Modeling ring current proton precipitation by electromagnetic ion cyclotron waves during the May 1416, 1997, storm, *J. Geophys. Res.*, *106*(A1), 7–22, doi:10.1029/2000JA002008.

[118] Jordanova, V. K., D. T. Welling, S. G. Zaharia, L. Chen, and R. M. Thorne (2012), Modeling ring current ion and electron dynamics and plasma instabilities during a high-speed stream driven storm, *J. Geophys. Res.*, *117*(A00L08), 0148–0227, doi:10.1029/2011JA017433.

[119] Jordanova, Y., V. K. andMiyoshi (2005), Relativistic model of ring current and radiation belt ions and electrons: Initial results, *Geophys. Res. Lett.*, *32*(14), 14,104, doi:10.1029/2005GL023020.

[120] Joselyn, J. A., and B. T. Tsurutani (1990), Geomagnetic sudden impulses and storm sudden commencements - A note on terminology, *EOS Transactions*, *71*, 1808, doi:10.1029/90EO00350.

[121] Kahler, S. (1987), Coronal mass ejections, *Reviews of Geophysics*, *25*, 663–675, doi:10.1029/RG025i003p00663.

[122] Kahler, S. W., N. R. Sheeley, Jr., and M. Liggett (1989), Coronal mass ejections and associated X-ray flare durations, , *344*, 1026–1033, doi:10.1086/167869.

[123] Kamide, Y., and J. D. Winningham (1977), A statistical study of the 'instantaneous' nightside auroral oval - The equatorward boundary of electron precipitation as observed by the Isis 1 and 2 satellites, , *82*, 5573–5588, doi:10.1029/JA082i035p05573.

[124] Kataoka, R., and Y. Miyoshi (2006), Flux enhancement of radiation belt electrons during geomagnetic storms driven by coronal mass ejections and corotating interaction regions, *Space Weather*, *4*, 09004, doi:10.1029/2005SW000211.

[125] Kawano, H., and T. Higuchi (1996), A generalization of the minimum variance analysis method, *Annales Geophysicae*, *14*, 1019–1024, doi:10.1007/s00585-996-1019-1.

[126] Kennel, C. F., and H. E. Petschek (1966), Limit on Stably Trapped Particle Fluxes, , *71*, 1.

[127] Kennel, C. F., J. P. Edmiston, and T. Hada (1985), A quarter century of collisionless shock research, *Washington DC American Geophysical Union Geophysical Monograph Series*, *34*, 1–36.

[128] Kim, K.-C., Y. Shprits, J. Lee, and J. Hwang (2013), Empirically modeled global distribution of magnetospheric chorus amplitude using an artificial neural network, *Journal of Geophysical Research (Space Physics)*, *118*, 6243–6253, doi:10.1002/jgra.50595.

[129] Kivelson, M. G., and C. T. Russell (1995), *Introduction to Space Physics*, Cambridge University Press, UK.

[130] Krasnoselskikh, V., et al. (2013), The Dynamic Quasiperpendicular Shock: Cluster Discoveries, , *178*, 535–598, doi:10.1007/s11214-013-9972-y.

[131] Krieger, A. S., A. F. Timothy, and E. C. Roelof (1973), A Coronal Hole and Its Identification as the Source of a High Velocity Solar Wind Stream, , *29*, 505–525, doi:10.1007/BF00150828.

[132] Kullback, S. (1959), Information theory and statistics, in *Information Theory and Statistics*, Wiley series in probability and mathematical statistics. Probability and mathematical statistics, John Wiley &Sons.

[133] Kullback, S., and R. A. Leibler (1951), On information and sufficiency, *The Annals of Mathematical Statistics*, *22*, doi:10.1214/aoms/1177729694.

[134] Lang, K. R. (2000), The Sun From Space, , *273*, 1–6.

[135] Lanzerotti, L. J., and A. Wolfe (1980), Particle diffusion in the geomagnetosphere - Comparison of estimates from measurements of magnetic and electric field fluctuations, , *85*, 2346–2348, doi:10.1029/JA085iA05p02346.

[136] LeDocq, M. J., D. A. Gurnett, and G. B. Hospodarsky (1998), Chorus Source Locations from VLF Poynting Flux Measurements with the Polar Spacecraft, , *25*, 4063, doi:10.1029/1998GL900071.

[137] Lepping, R. P., and P. D. Argentiero (1971), Single spacecraft method of estimating shock normals, , *76*, 4349, doi:10.1029/JA076i019p04349.

[138] Li, W., Y. Y. Shprits, and R. M. Thorne (2007), Dynamic evolution of energetic outer zone electrons due to wave-particle interactions during storms,

Journal of Geophysical Research (Space Physics), *112*(A11), A10220, doi: 10.1029/2007JA012368.

[139] Li, W., et al. (2009), Global distribution of whistler-mode chorus waves observed on the THEMIS spacecraft, , *36*, L09104, doi:10.1029/2009GL037595.

[140] Li, W., et al. (2010), THEMIS analysis of observed equatorial electron distributions responsible for the chorus excitation, *Journal of Geophysical Research (Space Physics)*, *115*, A00F11, doi:10.1029/2009JA014845.

[141] Li, W., J. Bortnik, R. M. Thorne, and V. Angelopoulos (2011), Global distribution of wave amplitudes and wave normal angles of chorus waves using THEMIS wave observations, *Journal of Geophysical Research (Space Physics)*, *116*(A15), A12205, doi:10.1029/2011JA017035.

[142] Li, W., B. Ni, R. M. Thorne, J. Bortnik, J. C. Green, C. A. Kletzing, W. S. Kurth, and G. B. Hospodarsky (2013), Constructing the global distribution of chorus wave intensity using measurements of electrons by the POES satellites and waves by the Van Allen Probes, , *40*, 4526–4532, doi: 10.1002/grl.50920.

[143] Li, W., et al. (2014), Radiation belt electron acceleration by chorus waves during the 17 March 2013 storm, *Journal of Geophysical Research (Space Physics)*, *119*, 4681–4693, doi:10.1002/2014JA019945.

[144] Li, X., and M. A. Temerin (2001), The electron radiation belt, *Space Science Reviews*, *95*(1), doi:10.1023/A:1005221108016.

[145] Li, X., I. Roth, M. Temerin, J. R. Wygant, M. K. Hudson, and J. B. Blake (1993), Simulation of the prompt energization and transport of radiation

belt particles during the March 24, 1991 SSC, , *20*, 2423–2426, doi:10.1029/93GL02701.

[146] Li, X., et al. (1999), Rapid enchancements of relativistic electrons deep in the magnetosphere during the May 15, 1997, magnetic storm, , *104*, 4467–4476, doi:10.1029/1998JA900092.

[147] Li, X., D. N. Baker, M. Temerin, G. Reeves, R. Friedel, and C. Shen (2005), Energetic electrons, 50 keV to 6 MeV, at geosynchronous orbit: Their responses to solar wind variations, *Space Weather*, *3*(4), doi:10.1029/2004SW000105.

[148] Li, X. F., and H.-R. Cho (1997), Development and propagation of equatorial waves, *Advances in Atmospheric Sciences*, *14*, 323–338, doi:10.1007/s00376-997-0053-6.

[149] Liemohn, M. W., and M. Jazowski (2008), Ring current simulations of the 90 intense storms during solar cycle 23, *J. Geophys. Res.*, *113*(A3), A00A17, doi:10.1029/2008JA013466.

[150] Lin, C. C., H. Q. Feng, D. J. Wu, J. K. Chao, L. C. Lee, and L. H. Lyu (2009), Two-spacecraft observations of an interplanetary slow shock, *Journal of Geophysical Research (Space Physics)*, *114*, A03105, doi:10.1029/2008JA013154.

[151] Loewe, C. A., and G. W. Prölss (1997), Classification and mean behavior of magnetic storms, , *102*, 14,209–14,214, doi:10.1029/96JA04020.

[152] Lohmeyer, W. Q., and K. Cahoy (2013), Space weather radiation effects on geostationary satellite solid-state power amplifiers, *Space Weather*, *11*, 476–488, doi:10.1002/swe.20071.

[153] Lui, A. T. Y., C. D. Anger, and S.-I. Akasofu (1975), The equatorward boundary of the diffuse aurora and auroral substorms as seen by the Isis 2 auroral scanning photometer, , *80*, 3603–3614, doi:10.1029/JA080i025p03603.

[154] Lui, A. T. Y., S.-I. Akasofu, E. W. Hones, Jr., S. J. Bame, and C. E. McIlwain (1976), Observation of the plasma sheet during a contracted oval substorm in a prolonged quiet period, , *81*, 1415–1419, doi:10.1029/JA081i007p01415.

[155] Lyatsky, W., and G. V. Khazanov (2008), Effect of solar wind density on relativistic electrons at geosynchronous orbit, , *35*, L03109, doi:10.1029/2007GL032524.

[156] Lyons, L. R., and R. M. Thorne (1973), Equilibrium structure of radiation belt electrons, , *78*, 2142–2149, doi:10.1029/JA078i013p02142.

[157] Lyons, L. R., R. M. Thorne, and C. F. Kennel (1972), Pitch-angle diffusion of radiation belt electrons within the plasmasphere, , *77*, 3455, doi:10.1029/JA077i019p03455.

[158] Manoharan, P. K. (2006), Evolution of Coronal Mass Ejections in the Inner Heliosphere: A Study Using White-Light and Scintillation Images, , *235*, 345–368, doi:10.1007/s11207-006-0100-y.

[159] Matsumura, C., Y. Miyoshi, K. Seki, S. Saito, V. Angelopoulos, and J. Koller (2011), Outer radiation belt boundary location relative to the magnetopause: Implications for magnetopause shadowing, *J. Geophys. Res.*, *116*(A6), A06,212, doi:10.1029/2011JA016575.

[160] Mauk, B. H., N. J. Fox, S. G. Kanekal, R. L. Kessel, D. G. Sibeck, and A. Ukhorskiy (2013), Science Objectives and Rationale for the Radiation Belt Storm Probes Mission, , *179*, 3–27, doi:10.1007/s11214-012-9908-y.

[161] McIlwain, C. E. (1961), Coordinates for Mapping the Distribution of Magnetically Trapped Particles, , *66*, 3681–3691, doi:10.1029/JZ066i011p03681.

[162] Meier, M. M., R. D. Belian, T. E. Cayton, R. A. Christensen, B. Garcia, K. M. Grace, J. C. Ingraham, J. G. Laros, and G. D. Reeves (1996), The energy spectrometer for particles (esp): Instrument description and orbital performance, *AIP Conference Proceedings*, *383*, 203–210, doi:10.1063/1.51533.

[163] Menvielle, M., and A. Berthelier (1991), The K-derived planetary indices - Description and availability, *Reviews of Geophysics*, *29*, 415–432, doi:10.1029/91RG00994.

[164] Meredith, N. P., R. B. Horne, A. D. Johnstone, and R. R. Anderson (2000), The temporal evolution of electron distributions and associated wave activity following substorm injections in the inner magnetosphere, , *105*, 12,907–12,918, doi:10.1029/2000JA900010.

[165] Meredith, N. P., R. B. Horne, and R. R. Anderson (2001), Substorm dependence of chorus amplitudes: Implications for the acceleration of electrons to relativistic energies, , *106*, 13,165–13,178, doi:10.1029/2000JA900156.

[166] Meredith, N. P., R. B. Horne, R. H. A. Iles, R. M. Thorne, D. Heynderickx, and R. R. Anderson (2002), Outer zone relativistic electron acceleration associated with substorm-enhanced whistler mode chorus, *J. Geophys. Res.*, *107*(A7), 0148–0227, doi:10.1029/2001JA900146.

[167] Meredith, N. P., R. B. Horne, R. M. Thorne, and R. R. Anderson (2003), Favored regions for chorus-driven electron acceleration to relativistic energies in the Earth's outer radiation belt, , *30*, 1871, doi:10.1029/2003GL017698.

[168] Meredith, N. P., R. B. Horne, R. M. Thorne, D. Summers, and R. R. Anderson (2004), Substorm dependence of plasmaspheric hiss, *Journal of Geophysical Research (Space Physics)*, *109*, A06209, doi:10.1029/2004JA010387.

[169] Meredith, N. P., R. B. Horne, A. Sicard-Piet, D. Boscher, K. H. Yearby, W. Li, and R. M. Thorne (2012), Global model of lower band and upper band chorus from multiple satellite observations, *Journal of Geophysical Research (Space Physics)*, *117*(A16), A10225, doi:10.1029/2012JA017978.

[170] Meredith, N. P., R. B. Horne, J. Bortnik, R. M. Thorne, L. Chen, W. Li, and A. Sicard-Piet (2013), Global statistical evidence for chorus as the embryonic source of plasmaspheric hiss, , *40*, 2891–2896, doi:10.1002/grl.50593.

[171] Millan, R. M., and R. M. Thorne (2007), Review of radiation belt relativistic electron losses, *Journal of Atmospheric and Solar-Terrestrial Physics*, *69*, 362–377, doi:10.1016/j.jastp.2006.06.019.

[172] Miyoshi, Y., and R. Kataoka (2005), Ring current ions and radiation belt electrons during geomagnetic storms driven by coronal mass ejections and corotating interaction regions, , *32*, L21105, doi:10.1029/2005GL024590.

[173] Mourenas, D., A. V. Artemyev, O. V. Agapitov, and V. Krasnoselskikh (2013), Analytical estimates of electron quasi-linear diffusion by fast magnetosonic waves, *Journal of Geophysical Research (Space Physics)*, *118*, 3096–3112, doi:10.1002/jgra.50349.

[174] Munro, R. H., J. T. Gosling, E. Hildner, R. M. MacQueen, A. I. Poland, and C. L. Ross (1979), The association of coronal mass ejection transients with other forms of solar activity, , *61*, 201–215, doi:10.1007/BF00155456.

[175] Ness, N. F., C. S. Scearce, and J. B. Seek (1964), Initial Results of the Imp 1 Magnetic Field Experiment, , *69*, 3531–3569, doi:10.1029/JZ069i017p03531.

[176] Neugebauer, M., and C. W. Snyder (1962), Solar Plasma Experiment, *Science*, *138*, 1095–1097, doi:10.1126/science.138.3545.1095-a.

[177] Ni, B., R. M. Thorne, Y. Y. Shprits, and J. Bortnik (2008), Resonant scattering of plasma sheet electrons by whistler-mode chorus: Contribution to diffuse auroral precipitation, , *35*, L11106, doi:10.1029/2008GL034032.

[178] Nishimura, Y., et al. (2010), Identifying the Driver of Pulsating Aurora, *Science*, *330*, 81–, doi:10.1126/science.1193186.

[179] O'Brien, T. P., R. L. McPherron, D. Sornette, G. D. Reeves, R. Friedel, and H. J. Singer (2001), Which magnetic storms produce relativistic electrons at geosynchronous orbit?, , *106*, 15,533–15,544, doi:10.1029/2001JA000052.

[180] Odstrcil, D., P. Riley, and X. P. Zhao (2004), simulation of the 12 May 1997 interplanetary CME event, *J. Geophys. Res.*, *109*(A2), 0148–0227, doi:10.1029/2003JA010135.

[181] Ohtani, S., Y. Miyoshi, H. J. Singer, and J. M. Weygand (2009), On the loss of relativistic electrons at geosynchronous altitude: Its dependence on magnetic configurations and external conditions, *J. Geophys. Res.*, *114*(A1), A01,202, doi:10.1029/2008JA013391.

[182] Omura, Y., N. Furuya, and D. Summers (2007), Relativistic turning acceleration of resonant electrons by coherent whistler mode waves in a dipole magnetic field, *J. Geophys. Res.*, *112*(A6), A06,236.

[183] Omura, Y., M. Hikishima, Y. Katoh, D. Summers, and S. Yagitani (2009), Nonlinear mechanisms of lower-band and upper-band VLF chorus emissions in the magnetosphere, *Journal of Geophysical Research (Space Physics)*, *114*, A07217, doi:10.1029/2009JA014206.

[184] Onsager, T. G., J. C. Green, G. D. Reeves, and H. J. Singer (2007), Solar wind and magnetospheric conditions leading to the abrupt loss of outer radiation belt electrons, *J. Geophys. Res.*, *112*(A1), A01,202, doi: 10.1029/2006JA011708.

[185] Papadopoulos, K. (1985), Microinstabilities and anomalous transport, *Washington DC American Geophysical Union Geophysical Monograph Series*, *34*, 59–90.

[186] Parker, E. N. (1963), *Interplanetary dynamical processes.*, Interscience Publishers, New York.

[187] Parrot, M., and F. Lefeuvre (1986), Statistical study of the propagation characteristics of ELF hiss observed on GEOS-1, inside and outside the plasmasphere, *Annales Geophysicae*, *4*, 363–383.

[188] Paschmann, G. (1997), Observational Evidence for Transfer of Plasma Across the Magnetopause, , *80*, 217–234, doi:10.1023/A:1004926004806.

[189] Paulikas, G. A., and J. B. Blake (1979), Effects of the solar wind on magnetospheric dynamics - energetic electrons at the synchronous orbit, in *Quantitative modeling of magnetospheric processes*, edited by W. P. Olson, Geophys. Mono. Ser., pp. 180–202, AGU, Washington DC.

[190] Pfitzer, L. R., S. Kane, and J. R. Winckler (1966), The spectra and intensity of electrons in the radiation belts,, *J. Space Res.*, *6*, 702.

[191] Pizzo, V. (1978), A three-dimensional model of corotating streams in the solar wind. I - Theoretical foundations, , *83*, 5563–5572, doi:10.1029/JA083iA12p05563.

[192] Reeves, G. D. (1998), Relativistic electrons and magnetic storms: 1992-1995, , *25*, 1817–1820, doi:10.1029/98GL01398.

[193] Reeves, G. D., K. L. McAdams, R. H. W. Friedel, and T. P. O'Brien (2003), Acceleration and loss of relativistic electrons during geomagnetic storms, , *30*, 1529, doi:10.1029/2002GL016513.

[194] Reeves, G. D., S. K. Morley, R. H. W. Friedel, M. G. Henderson, T. E. Cayton, G. Cunningham, J. B. Blake, R. A. Christensen, and D.Thomsen (2011), On the relationship between relativistic electron flux and solar wind velocity, *J. Geophys. Res.*, *116*(A2), doi:10.1029/2010JA015735.

[195] Reeves, G. D., S. Morley, and G. Cunningham (2013), Long-term variations in solar wind velocity and radiation belt electrons, *Journal of Geophysical Research (Space Physics)*, *118*, 1040–1048, doi:10.1002/jgra.50126.

[196] Roeder, J. L., J. F. Fennell, M. W. Chen, M. Schulz, M. Grande, and S. Livi (1996), CRRES observations of the composition of the ring-current ion populations, *Advances in Space Research*, *17*, 17–24, doi:10.1016/0273-1177(95)00689-C.

[197] Rostoker, G., E. Friedrich, and M. Dobbs (1997), Physics of magnetic storms, *Washington DC American Geophysical Union Geophysical Monograph Series*, *98*, 149–160, doi:10.1029/GM098p0149.

[198] Rothwell, P., and C. E. McIlwain (1960), Magnetic Storms and the Van Allen Radiation Belts: Observations from Satellite 1958ϵ (Explorer IV), , *65*, 799, doi:10.1029/JZ065i003p00799.

[199] Russell, C. T., and R. L. McPherron (1973), Semiannual variation of geomagnetic activity, , *78*, 92, doi:10.1029/JA078i001p00092.

[200] Russell, C. T., and R. M. Thorne (1970), On the structure of the inner magnetosphere., *Cosmic Electrodynamics*, *1*, 67–89.

[201] Russell, C. T., L. K. Jian, X. Blanco Cano, J. G. Luhmann, and T. L. Zhang (2009), STEREO observations of shock formation in the solar wind, , *36*, L02103, doi:10.1029/2008GL036337.

[202] Sagdeev, R. Z. (1966), Cooperative Phenomena and Shock Waves in Collisionless Plasmas, *Reviews of Plasma Physics*, *4*, 23.

[203] Sagdeev, R. Z. (1979), The 1976 Oppenheimer lectures: Critical problems in plasma astrophysics. I. Turbulence and nonlinear waves, *Reviews of Modern Physics*, *51*, 1–10, doi:10.1103/RevModPhys.51.1.

[204] Sagdeev, R. Z., and A. A. Galeev (1969), *Nonlinear Plasma Theory*, Benjamin, New York.

[205] Saitou, Y., Y. Nakamura, T. Kamimura, and O. Ishihara (2012), Bow Shock Formation in a Complex Plasma, *Physical Review Letters*, *108*(6), 065004, doi:10.1103/PhysRevLett.108.065004.

[206] Santolík, O., and D. A. Gurnett (2003), Transverse dimensions of chorus in the source region, , *30*, 1031, doi:10.1029/2002GL016178.

[207] Santolík, O., E. Macúšová, K. H. Yearby, N. Cornilleau-Wehrlin, and H. S. K. Alleyne (2005), Radial variation of whistler-mode chorus: first results from the STAFF/DWP instrument on board the Double Star TC-1 spacecraft, *Annales Geophysicae*, *23*, 2937–2942, doi:10.5194/angeo-23-2937-2005.

[208] Schrijver, C. J. (2009), Driving major solar flares and eruptions: A review, *Advances in Space Research*, *43*, 739–755, doi:10.1016/j.asr.2008.11.004.

[209] Schulz, M., and L. J. Lanzerotti (1974), Particle Diffusion in the Radiation Belts, *Physics and Chemistry in Space*, *7*, doi:10.1007/978-3-642-65675-0.

[210] Schwabe, S. H. (1843), Solar observations during 1843, *Astron. Nachr*, *21*, 233.

[211] Schwenn, R. (2006), Solar Wind Sources and Their Variations Over the Solar Cycle, , *124*, 51–76, doi:10.1007/s11214-006-9099-5.

[212] Selesnick, R. S., and J. B. Blake (1998), Radiation belt electron observations following the January 1997 magnetic cloud event, , *25*, 2553–2556, doi:10.1029/98GL00665.

[213] Sheeley, N. R., Jr., et al. (1975), Coronal changes associated with a disappearing filament, , *45*, 377–392, doi:10.1007/BF00158457.

[214] Sheeley, N. R., Jr., R. A. Howard, M. J. Koomen, and D. J. Michels (1983), Associations between coronal mass ejections and soft X-ray events, , *272*, 349–354, doi:10.1086/161298.

[215] Sheeley, N. R., Jr., R. A. Howard, D. J. Michels, M. J. Koomen, R. Schwenn, K. H. Muehlhaeuser, and H. Rosenbauer (1985), Coronal mass ejections and interplanetary shocks, , *90*, 163–175, doi:10.1029/JA090iA01p00163.

[216] Sheldon, R. B., H. E. Spence, J. D. Sullivan, T. A. Fritz, and J. Chen (1998), The discovery of trapped energetic electrons in the outer cusp, , *25*, 1825–1828, doi:10.1029/98GL01399.

[217] Shklyar, D., and H. Matsumoto (2009), Oblique whistler-mode waves in the inhomogeneous magnetospheric plasma: Resonant interactions with energetic charged particles, *Surv. Geophys.*, *30*, 55–104.

[218] Shklyar, D. R. (2011), On the nature of particle energization via resonant wave-particle interaction in the inhomogeneous magnetospheric plasma, *Annales Geophysicae*, *29*, 1179–1188, doi:10.5194/angeo-29-1179-2011.

[219] Shprits, Y. Y., D. A. Subbotin, N. P. Meredith, and S. R. Elkington (2008), Review of modeling of losses and sources of relativistic electrons in the outer radiation belt ii: Local acceleration and loss, *Journal of Atmospheric and Solar-Terrestrial Physics*, *70*(14), 1694–1713.

[220] Shprits, Y. Y., D. Subbotin, and B. Ni (2009), Evolution of electron fluxes in the outer radiation belt computed with the VERB code, *Journal of Geophysical Research (Space Physics)*, *114*(A13), A11209, doi:10.1029/2008JA013784.

[221] Siscoe, G. L. (1972), Structure and orientations of solar-wind interaction fronts: Pioneer 6, , *77*, 27, doi:10.1029/JA077i001p00027.

[222] Snyder, C. W., M. Neugebauer, and U. R. Rao (1963), The solar wind velocity and its correlation with cosmic-ray variations and with solar and

geomagnetic activity, *Journal of Geophysical Research*, *68*(24), 6361–6370, doi:10.1029/JZ068i024p06361.

[223] Sonett, C. P., and I. J. Abrams (1963), The Distant Geomagnetic Field, 3, Disorder and Shocks in the Magnetopause, , *68*, 1233–1263, doi:10.1029/JZ068i005p01233.

[224] Sonnerup, B. U. O., and L. J. Cahill, Jr. (1967), Magnetopause Structure and Attitude from Explorer 12 Observations, , *72*, 171, doi:10.1029/JZ072i001p00171.

[225] Stone, E. C., A. M. Frandsen, R. A. Mewaldt, E. R. Christian, D. Margolies, J. F. Ormes, and F. Snow (1998), The Advanced Composition Explorer, , *86*, 1–22, doi:10.1023/A:1005082526237.

[226] Sugiura, M. (1963), *Hourly values of equatorial Dst for the IGY*, NASA, Goddard Space Flight Center, Greenbelt.

[227] Summers, D., and R. M. Thorne (2003), Relativistic electron pitch-angle scattering by electromagnetic ion cyclotron waves during geomagnetic storms, *J. Geophys. Res.*, *108*(A4), 1143.

[228] Summers, D., R. M. Thorne, and F. Xiao (1998), Relativistic theory of wave-particle resonant diffusion with application to electron acceleration in the magnetosphere, , *103*, 20,487–20,500, doi:10.1029/98JA01740.

[229] Summers, D., C. Ma, N. P. Meredith, R. B. Horne, R. M. Thorne, D. Heynderickx, and R. R. Anderson (2002), Model of the energization of outer-zone electrons by whistler-mode chorus during the October 9, 1990 geomagnetic storm, *Geophys. Res. Lett.*, *29*(24), 2174.

[230] Summers, D., C. Ma, and T. Mukai (2004), Competition between acceleration and loss mechanisms of relativistic electrons during geomagnetic storms, *Journal of Geophysical Research (Space Physics)*, *109*, A04221, doi: 10.1029/2004JA010437.

[231] Summers, D., C. Ma, N. Meredith, R. Horne, R. Thorne, and R. Anderson (2004), Modeling outer-zone relativistic electron response to whistler-mode chorus activity during substorms, *Journal of Atmospheric and Solar-Terrestrial Physics*, *66*(2), 133–146.

[232] Summers, D., B. Ni, and N. P. Meredith (2007), Timescales for radiation belt electron acceleration and loss due to resonant wave-particle interactions: 2. Evaluation for VLF chorus, ELF hiss, and electromagnetic ion cyclotron waves, *Journal of Geophysical Research (Space Physics)*, *112*, A04207, doi: 10.1029/2006JA011993.

[233] Taktakishvili, A., M. Kuznetsova, P. MacNeice, M. Hesse, L. Rasttter, A. Pulkkinen, A. Chulaki, and D. Odstrcil (2009), Validation of the coronal mass ejection predictions at the Earth orbit estimated by ENLIL heliosphere cone model, *Space Weather*, *7*(3), 1542, doi:10.1029/2008SW000448.

[234] Taylor, W. W. L., and D. A. Gurnett (1968), Morphology of VLF emissions observed with the Injun 3 satellite, , *73*, 5615–5626, doi:10.1029/JA073i017p05615.

[235] Thomsen, M. F. (2004), Why Kp is such a good measure of magnetospheric convection, *Space Weather*, *2*, S11004, doi:10.1029/2004SW000089.

[236] Thorne, R. M. (2010), Radiation belt dynamics: The importance of wave-particle interactions, , *37*, L22107, doi:10.1029/2010GL044990.

[237] Thorne, R. M., E. J. Smith, R. K. Burton, and R. E. Holzer (1973), Plasmaspheric hiss, , *78*, 1581–1596, doi:10.1029/JA078i010p01581.

[238] Thorne, R. M., E. J. Smith, K. J. Fiske, and S. R. Church (1974), Intensity variation of ELF hiss and chorus during isolated substorms, , *1*, 193–196, doi:10.1029/GL001i005p00193.

[239] Thorne, R. M., T. P. O'Brien, Y. Y. Shprits, D. Summers, and R. B. Horne (2005), Timescale for MeV electron microburst loss during geomagnetic storms, *Journal of Geophysical Research (Space Physics)*, *110*, A09202, doi:10.1029/2004JA010882.

[240] Thorne, R. M., B. Ni, X. Tao, R. B. Horne, and N. P. Meredith (2010), Scattering by chorus waves as the dominant cause of diffuse auroral precipitation, , *467*, 943–946, doi:10.1038/nature09467.

[241] Thorne, R. M., et al. (2013), Rapid local acceleration of relativistic radiation-belt electrons by magnetospheric chorus, *Nature*, *504*, 411–414, doi:10.1038/nature12889.

[242] Tousey, R. (1973), First Results from Skylab., in *Bulletin of the American Astronomical Society*, *Bulletin of the American Astronomical Society*, vol. 5, p. 419.

[243] Tsurutani, B. T., and E. J. Smith (1974), Postmidnight chorus: A substorm phenomenon, , *79*, 118–127, doi:10.1029/JA079i001p00118.

[244] Tsurutani, B. T., A. L. Brinca, E. J. Smith, R. T. Okida, and R. R. Anderson (1989), A statistical study of ELF-VLF plasma waves at the magnetopause, , *94*, 1270–1280, doi:10.1029/JA094iA02p01270.

[245] Tu, W., X. Li, Y. Chen, G. D. Reeves, and M. Temerin (2009), Storm-dependent radiation belt electron dynamics, *J. Geophys. Res.*, *114*(A2), 0148–0227, doi:10.1029/2008JA013480.

[246] Turner, D. L., V. Angelopoulos, W. Li, M. D. Hartinger, M. Usanova, I. R. Mann, J. Bortnik, and Y. Shprits (2013), On the storm-time evolution of relativistic electron phase space density in Earth's outer radiation belt, *Journal of Geophysical Research (Space Physics)*, *118*, 2196–2212, doi:10.1002/jgra.50151.

[247] Turner, N. E., D. N. Baker, T. I. Pulkkinen, and R. L. McPherron (2000), Evaluation of the tail current contribution to Dst, , *105*, 5431–5440, doi:10.1029/1999JA000248.

[248] van Allen, J. A. (1959), The Geomagnetically Trapped Corpuscular Radiation, , *64*, 1683–1689, doi:10.1029/JZ064i011p01683.

[249] Van Allen, J. A. (1991), Why radiation belts exist, *EOS Transactions*, *72*, 361–363, doi:10.1029/90EO10279.

[250] van Allen, J. A., and L. A. Frank (1959), Radiation Measurements to 658,300 Km. with Pioneer IV, , *184*, 219–224, doi:10.1038/184219a0.

[251] Vassiliadis, D., S. F. Fung, and A. J. Klimas (2005), Solar, interplanetary, and magnetospheric parameters for the radiation belt energetic electron flux, *Journal of Geophysical Research (Space Physics)*, *110*, A04201, doi:10.1029/2004JA010443.

[252] Vernov, S. N., A. E. Chudakov, P. V. Vakulov, and Y. I. Logachev (1959), The Study of the Terrestrial Corpuscular Radiation and Cosmic Rays during the Flight of a Cosmic Rocket, *Soviet Physics Doklady*, *4*, 338.

[253] West, H. I., R. M. Buck, and J. R. Walton (1973), Electron pitch angle distributions throughout the magnetosphere as observed on ogo 5, *Journal of Geophysical Research*, *78*(7), 1064–1081, doi:10.1029/JA078i007p01064.

[254] Whang, Y. C. (1996), Transition of slow shocks to fast shocks, in *American Institute of Physics Conference Series*, *American Institute of Physics Conference Series*, vol. 382, edited by D. Winterhalter, J. T. Gosling, S. R. Habbal, W. S. Kurth, and M. Neugebauer, pp. 562–565, doi:10.1063/1.51343.

[255] Whang, Y. C., J. Zhou, R. P. Lepping, and K. W. Ogilvie (1996), Interplanetary slow shock observed from Wind, , *23*, 1239–1242, doi:10.1029/96GL01358.

[256] Williams, D. J. (1966), A 27-day periodicity in outer zone trapped electron intensities, , *71*, 1815–1826, doi:10.1029/JZ071i007p01815.

[257] Wing, S., et al. (2005), Kp forecast models, *Journal of Geophysical Research (Space Physics)*, *110*, A04203, doi:10.1029/2004JA010500.

[258] Xiao, F., R. M. Thorne, and D. Summers (1998), Instability of electromagnetic R-mode waves in a relativistic plasma, *Physics of Plasmas*, *5*, 2489–2497, doi:10.1063/1.872932.

[259] Xiao, F., Q. Zhou, H. He, and L. Tang (2006), Instability of whistler-mode waves by a relativistic kappa-loss-cone distribution in space plasmas, *Plasma Physics and Controlled Fusion*, *48*, 1437–1445, doi:10.1088/0741-3335/48/9/012.

[260] Xiao, F., Z. Su, H. Zheng, and S. Wang (2009), Modeling of outer radiation belt electrons by multidimensional diffusion process, *Journal of Geophysical Research: Space Physics*, *114*(A3), n/a–n/a, doi:10.1029/2008JA013580.

[261] Xiao, F., Z. Su, H. Zheng, and S. Wang (2010), Three-dimensional simulations of outer radiation belt electron dynamics including cross-diffusion terms, *Journal of Geophysical Research: Space Physics*, *115*(A5), n/a–n/a, doi:10.1029/2009JA014541.

[262] Zhang, T. L., et al. (2006), Magnetic field investigation of the Venus plasma environment: Expected new results from Venus Express, , *54*, 1336–1343, doi:10.1016/j.pss.2006.04.018.